Mechanical Engineering Advances

https://ojs.acad-pub.com/index.php/mea

2024 VOLUME 2 ISSUE 1
ISSN: 3029-1232 (Online)

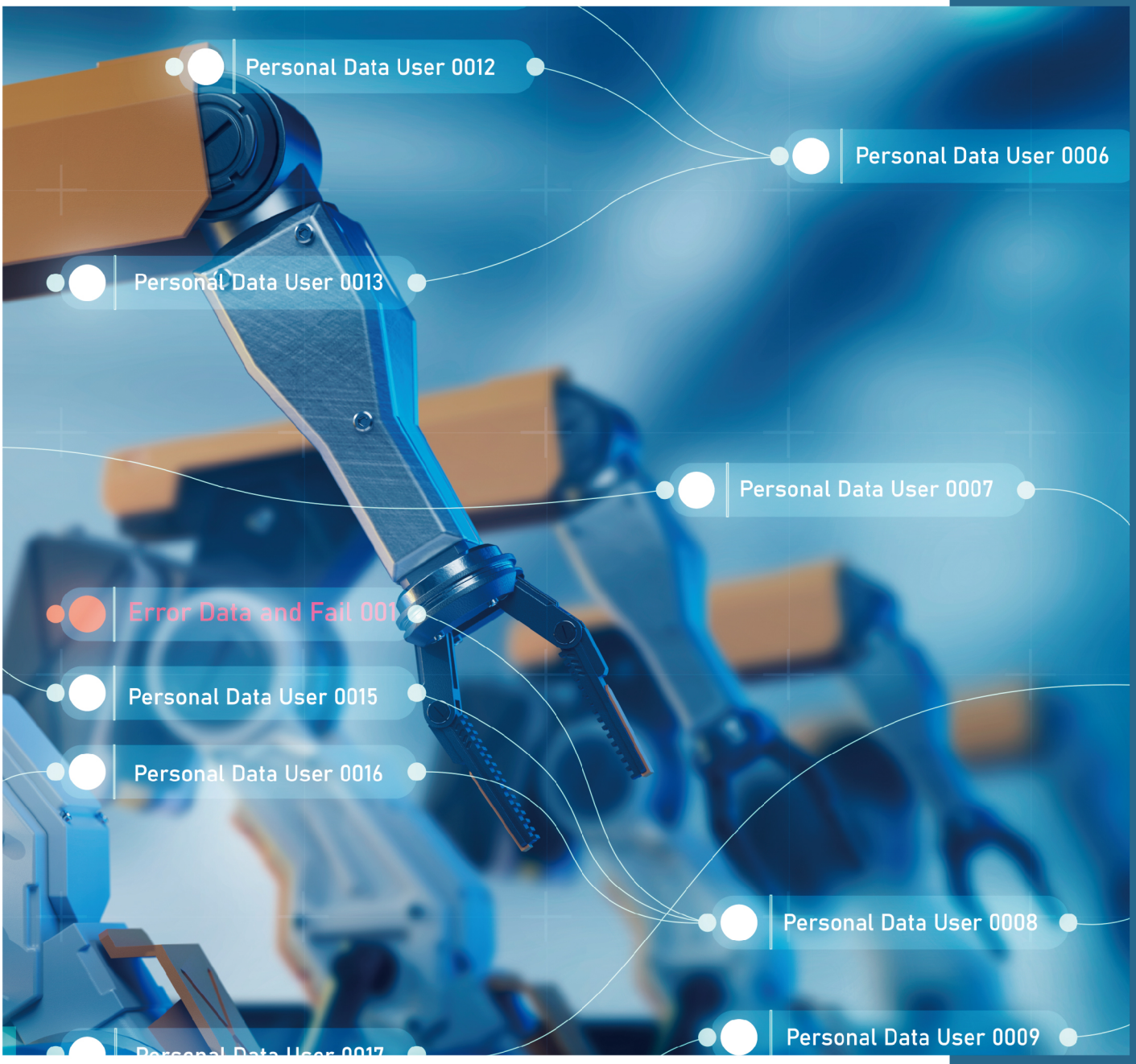

1

Editorial Board

Editor-in-Chief

Associate Editor

Editorial Board Members

Volume 2 Issue 1 • 2024

Mechanical Engineering Advances

ACADEMIC
ACADEMIC PUBLISHING PTE LTD

2024 | Volume 2 | Issue 1

Mechanical Engineering Advances

https://ojs.acad-pub.com/index.php/mea

Contents

Articles

Review

Mechanical Engineering Advances 2024, 2(1), 282.
https://doi.org/10.59400/mea.v2i1.282

Article

Low carbon integrated vehicles and buildings

Kevin Kendall

Research Department, Hydrogen United, B15 3HE Birmingham, UK; kevin.kendallbham@yahoo.co.uk

CITATION

Kendall K. Low carbon integrated vehicles and buildings. Mechanical Engineering Advances. 2024; 2(1): 282. doi: 10.59400/mea.v2i1.282

ARTICLE INFO

Received: 31 October 2023
Accepted: 3 January 2024
Available online: 30 January 2024

Abstract: This paper defines vehicles and buildings as main sources of United Kingdom (UK) carbon dioxide (CO_2) and seeks to cut such emissions using green hydrogen made from combined wind and solar energy. Combustion vehicles powered by fossil petroleum emit near half of UK climate-warming CO_2 while buildings heated by natural gas provide a third. First, current UK grid problems are defined: Electricity, gas and petroleum grids. Refueling green vehicles has been a particular problem. Then experiments on the private wire community of Keele University show how green hydrogen could integrate both green vehicles and buildings. Next, the model supply chain is planned and tested. Finally, experiments and calculations are outlined, analyzing the optimum system design criteria proposed. We conclude that economic green hydrogen can displace petroleum in vehicles, while powering buildings instead of natural gas. Also, the prospect in 2024 is that profits can be made all along the green hydrogen supply chain, such that new businesses involved in local private clean communities can cost less than the National Grid monopoly and other dominant fossil energy companies.

Keywords: wind turbines; solar energy; green hydrogen; green vehicles; green buildings

1. Introduction

The two largest problems for UK global warming are vehicles that combust petroleum-based fuels, and buildings that rely on natural gas for heating [1]. Together, these two sources of fossil CO_2 add up to three-quarters of UK climate change emissions. This paper explains how both problems could be solved by combining local wind power, solar electricity and hydrogen for energy storage [2].

Vehicle emission has been the worst issue because fossil CO_2 from transport has continued to rise whilst other polluters like industry and the electrical power network have cut fossil CO_2 over the last 30 years. Vehicle emissions rose as UK cars increased to 40.7 M vehicles in 2023, while doubling in weight that demanded twice the fuel since 1980. Buildings come second because there has been progress in new buildings, where energy standards have risen, with an EU prospect of mandatory solar panel installation from 2027 [3].

The advance [4] of solar renewable energy in UK homes reached almost 1.2 million in 2023 out of 26 million houses, giving around 4% penetration. Battery electric car penetration was near 2%, but only half green because the grid delivering the battery-charging is still dependent on natural gas until 2035 when off-shore wind should replace many gas and coal fired power stations.

The first part of this paper discusses difficulties for our grids trying to eliminate fossil-fuelled vehicles and buildings, then moves on to define several problems of green fuelling. Second: the combination of wind, solar and hydrogen energy in vehicles and buildings is invoked, using Keele University as the experimental area, the largest campus in Britain with 12,000 population needing about 7 MW of power on average throughout the year, mainly for buildings but also for recharging electric

vehicles. Then, experiments making green hydrogen on-site are described, followed by estimates of scale-up costs and benefits as the present gas and electricity grids are transformed by local wind + solar [5]. Finally, the conclusion is that combining wind, solar and hydrogen can play a profitable part in cutting the Keele fossil CO_2 intensity as the campus moves from 40% now to 100% green in the future.

2. Grid energy issues

Three main grids supply energy around Britain: Electricity, natural gas and petroleum. Since privatisation of gas in 1986 and electricity in 1990, government policy has been to define several major energy sources where electricity is generated or fuels are imported, with regional distribution run by around 6 large gas/electric companies and 5 big liquid fuel companies [6]. Transport fuels and natural gas dominate but the National Grid company running UK electricity infrastructure supplies 21% of UK energy (**Table 1**) through cables and this has been viewed as the future technology that should overtake the others, but it is only the number 7 in the league table of UK energy companies at present. National Grid is monopolistic in owning the English high-voltage wires which other companies must use, so prices are among the highest in Europe. A key problem is that the present electricity grid has little storage so balancing supply and demand is a minute-by-minute process that differs from storing diesel liquid in tanks or natural gas in caverns. The diesel grid could consist of pipes, but it is easier and cheaper to ship liquid fuels by road tankers.

Table 1. UK energy split in 2021 [6].

Energy supplied	TWh	Percentage
Electricity grid	308	21%
Gas grid	485	34%
Petroleum	638	45%
Total	1431	100%

As things stand in 2023, there is little chance that National Grid can increase its energy deliveries by a factor of 5 to replace gas and petroleum with green electricity. In the first place, it has swopped the feed-in tariff to a ‘smart export guarantee’ in 2019, reducing payments to green electricity generators. The original Grid feed-in-tariff was more generous and made solar panels popular since 2010, based on the Millennium German law, requiring energy companies to accept power from homes with solar generators. Second, the National Grid has not provided sufficient electricity to charge electric vehicles effectively. Third, hundreds of green energy projects are stalled waiting for Grid permissions to connect. Finally, National Grid supplies most of its energy from 181 large power stations and has not embraced distributed energy, which includes both wind and solar power, today established as our cheapest energy sources [5].

Cadent is now modifying the gas grid to carry green hydrogen in its pipes, but it is still not clear what the quality will be, mainly because odorants must be added to detect leaks by smell. Several projects have put hydrogen into houses [**7**], but problems of gas leaks and flame speed remain. In thermodynamic terms, combusting

hydrogen is both toxic and inefficient, and should be replaced by electrochemical Combined Heat and Power (CHP) based on hydrogen fuel cells. 100GW of green hydrogen production will be needed to replace petrol/natural gas throughout the UK and this will take decades to achieve.

Petroleum companies are finding it easier to address the green transition because they have been adding biofuels to their fossil liquids since 2010 and are now experimenting on hydrogen as a zero-emission fuel in buses and trucks. This was tested by shipping hydrogen tube trailers to petrol stations, changing the dispenser to suit the hydrogen vehicles. The cost of this shipping process is well understood throughout the UK's 8000 petroleum refuelling station infrastructure because various alternative fuels (e.g., diesel, LPG, biofuel, LNG) have been tried over the last 50 years. £500,000 is sufficient to get results on a green hydrogen refueler, whereas a permanent hydrogen station like the 2021 Tyseley (**Figure 1**) installation cost near £5M because it includes an electrolyser, large storage vessels and compressors to deliver both 700 bar and 350 bar pressurised gas. Moving to battery charging of electric vehicles across the refuelling station network is another major difficulty because high powered rapid chargers are needed, up to 100 kW DC, which require new electric power supplies, while the 80% charging time of 30 min for batteries is six times slower than hydrogen filling, meaning that many more electric charging units are required than hydrogen dispensers.

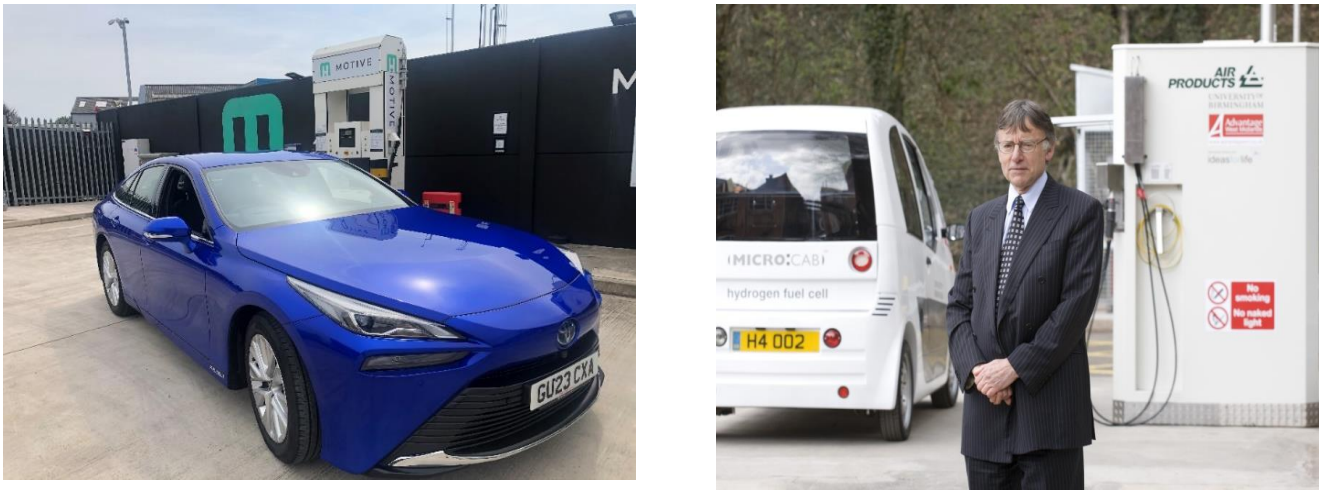

(a) **(b)**

Figure 1. (a) Tyseley hydrogen station refuelling a Toyota Mirai; **(b)** First UK green hydrogen refueler opened in 2008 in the University of Birmingham by the author.

The conclusion is that the existing grids cannot easily change, so it is now vital to consider distributed energy across the UK in the form of thousands of private wires combined with solar/wind electrical communities with big hydrogen storage for use in vehicles and buildings. Changing vehicles from combustion to hydrogen fuel cell battery electric vehicles (HFCBEVs) is the simplest first move because vehicle fuels are shipped and can be flexible, so hydrogen merely adds to petrol, diesel, biofuel, propane, LNG, etc on 8000 existing UK sites that can gradually go green, avoiding the present electric vehicle refuelling problems.

3. Problems of green refuelling

The standard product lifetime description [8] of development, introduction, growth, and maturity is illustrated in **Figure 2(a)** which shows how the number of German hydrogen refuelling stations increased from the first in 1999 to 92 in 2023. The first phase is the development, followed by introduction, then growth, stabilising at maturity which probably is premature because many more stations are planned in the future. Other regions like China, Japan, and Los Angeles have followed this trend, with installations proceeding steadily over time. In 2005, Los Angeles started its project on hydrogen cars and refuellers along with Japan which was manufacturing hydrogen cars at an increasing rate. China introduced its first two stations in 2008, but it took a decade before the growth phase started, rising steadily to 250 units in 2022, with hydrogen bus, truck and car manufacture beginning seriously in 2017.

In **Figure 2(a)**, the first phases of German growth and introduction were long, with experimentation from 1995 but seriously starting in 1999 at the opening of the first hydrogen station at Munich airport. The third phase, growth, started in Germany with the European Union projects on hydrogen buses in 2003, where the largest cities installed hydrogen stations, but not green. Then the third mature phase began around 2020 when there was an infrastructure across the country but insufficient demand from buses, trucks and cars which had to be introduced incrementally to make the whole hydrogen transport system economic. Subsidies were used to support the losses during this time, but eventually it is expected that the stations will grow naturally as profits become apparent.

Figure 2(b) shows that the UK experience was different. The first UK green hydrogen refuelling station was installed by the author at University of Birmingham in 2008 (**Figure 1**) and the enthusiasm for more stations around Britain then started, with Loughborough University following in 2009 and further plants built during the next decade as shown in **Figure 2(b)**. Then in 2018, the installation of UK hydrogen stations stopped, falling to four in 2023 as refuellers were closed, shown by results of **Figure 2(b)**, which compares the German results (**Figure 2(a)**) with the UK picture. Shell/ITM closed three of their hydrogen stations in 2022–2023.

Britain was behind but showed rapid growth (**Figure 2(b)**) until 2015 when the Aberdeen station opened and 2018 when Shell and ITM completed three hydrogen refuellers at motorway services near Gatwick, Cobham and Beaconsfield. Although the Government and UK industry had predicted 65 by 2020, small loss-making stations started to close, for example the Coventry and Birmingham University units which were too small and had low demand. The final blow came in 2022 when Shell closed their stations in England, leaving just Aberdeen, Rotherham, Birmingham and Heathrow operating. The strange shape of this curve may be explained by a product sales dip when early consumers realise that snags arise over the first years, followed by correction and optimisation that produce steady growth later.

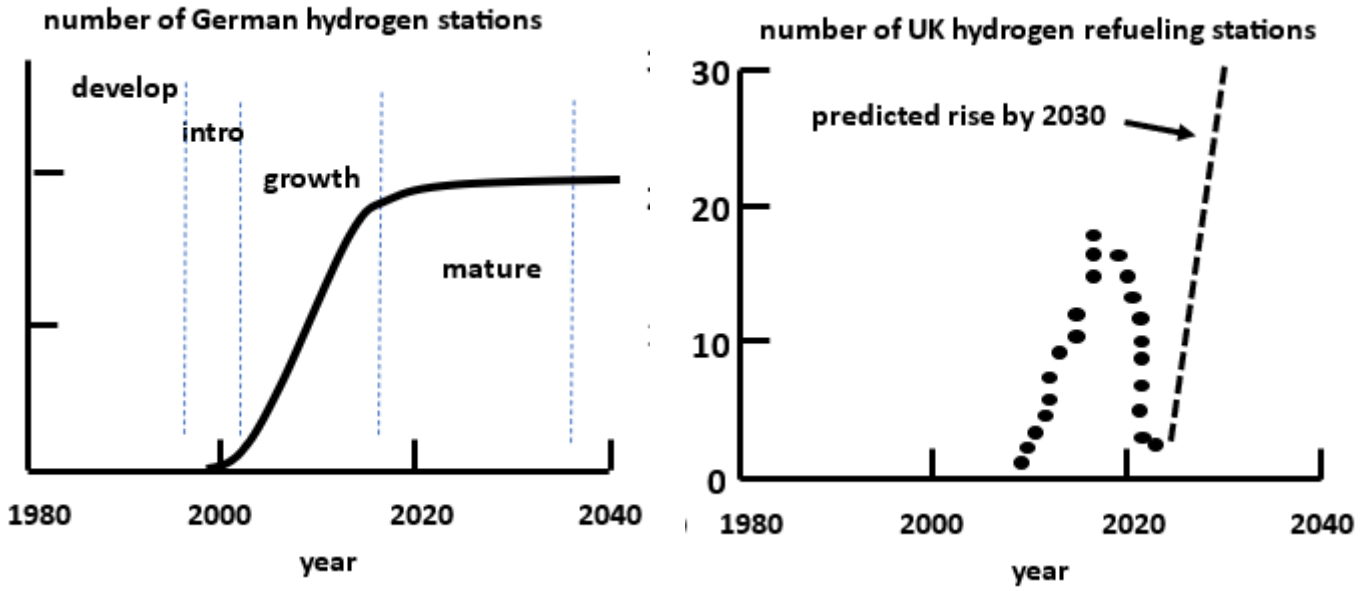

Figure 2. (a): Diagram showing how the German introduction of hydrogen stations followed the standard model for product sales [8]; **(b)**: Results in the UK showed a different picture where the early stations closed because of economic losses through failure to match supply and demand, followed by a predicted surge as profit is demonstrated in 2023.

The interesting differentiation of UK from Germany and China is that large hydrogen subsidies were not deployed in Britain so the premature acceleration to hundreds of refuelling stations seen overseas was killed by £M financial losses of companies like Motive Fuels and Shell. A similar closing of hydrogen stations happened at Everfuel in Denmark because losses were high due to low demand from hydrogen vehicles. However, in 2023 it was demonstrated in UK [9] that profits could be made along the green hydrogen supply chain, allowing capitalist forces to grow the market further as predicted by the dashed line predicting rapid growth of UK hydrogen stations after 2025 in **Figure 2(b)**.

Problems that caused the financial issues were readily identified [9]. First was the lack of demand for hydrogen vehicles, whose UK numbers rose very slowly at first because all hydrogen vehicles were imported and consumers did not buy them. Second, battery electric vehicles were strongly supported by the government with substantial subsidies, distracting hydrogen vehicle enthusiasts, who received no incentives. The third and most important issue was that the largest hydrogen refuelling installations were powered by grid electricity, which was neither green nor economic, costing twice the desired price-point of £10/kg that could compete with petroleum fuels.

The main loss-making decision was to manufacture hydrogen by electrolysis of water using grid electricity. Whereas the first station in Birmingham (**Figure 1(b)**) had used green biohydrogen and the 2015 ITM station in Rotherham had used wind-power green electricity, other units depended on the Grid which is not green and generally too expensive with prices ranging from £100/MWh to above £160/MWh which leads to a retail price in Birmingham of £23/kg, far too high to compete with

diesel at current prices. The fact is that electricity price for powering electrolysis is the main factor raising green hydrogen costs. £10/kWh is required at the retail point, so the price at the hydrogen manufacturer must be much less, around £5/kg or lower [9]. £10/kg is near the German retail price, which is subsidised [10]. California also appears to have a grid problem since 2023 retail hydrogen price rocketed to $36/kg from the original $13/kg. This makes grid sourced hydrogen non-competitive with fossil fuelled transport.

4. Combining wind and solar with hydrogen in vehicles and buildings

The profitable supply chain model described here was evaluated first in 2022 [9], using Keele University community of 12,000 people as an example of a private wire integrated renewable energy system using green hydrogen as energy storage material. At present, the system is running according to the model supply chain illustrated in **Figure 3** [11].

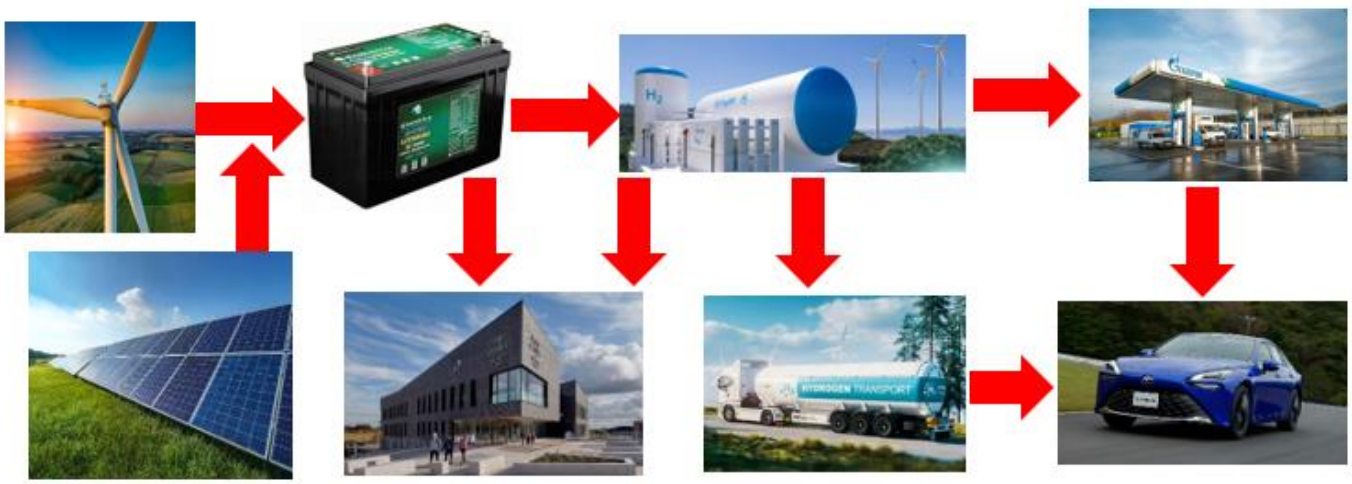

Figure 3. Diagram of the supply chain for a green private wire community starting on left with solar/wind charging a battery that feeds buildings and powers an electrolyser /hydrogen store leading to hydrogen for shipping plus vehicle refuelling and buildings energy.

The wind is combined with solar electricity on the left of **Figure 3** to feed a battery that can bridge short-term fluctuations (minutes) while feeding buildings to replace the usual grid power. Surplus electricity is produced at peak wind/solar operation, feeding a water electrolyser with low pressure storage that powers buildings with CHP (combined heat and power by fuel cell) when renewable electricity is low. The hydrogen is compressed to 500 bar to feed tube trailer storage on the right of Fig3 which can bridge a day of low renewables, and which can also ship and dispense hydrogen. 500 bar hydrogen runs the hydrogen refueller for trucks and buses, while 700 bar compression is needed for cars and vans.

Keele may be viewed as a village community of 12,000 souls requiring 7 MW on average, whereas a larger private site may rise to 30,000 people, a town requiring about 20 MW for homes. In 2022, the Keele Smart Energy Network Demonstration (SEND project) was opened to cut grid electricity input to Keele by half, saving

approximately £2 M per annum, at a capital investment of £8.1 M for design/build by Siemens and run by Equans [12]. Experimental quantities around 0.2 MW of green hydrogen were also produced but insufficient to make Keele campus fully green, which would require 5 MW of electrolyser capacity to absorb peak renewable electricity production, producing 2 tons per day of hydrogen to be stored for bridging a day of low wind/solar generation.

Early results shown smoothed in **Figure 4** reveal that a typical low-power autumn Keele day provides excess power from solar around noon for several hours, with 2 MWh of energy fed back into the National Grid. This was a day where wind was near zero, so solar input dominated. The National Grid buying price was low, about £50/MWh which is normal in the UK because the Grid is a monopoly that commands low prices for spare electricity. To avoid this, the excess Keele green power could be fed experimentally to the water electrolyser manufacturing green hydrogen for storage as shown in **Figure 3**, electrolysing water to make green hydrogen for application in buildings and vehicle refueling. To go fully green, the renewable energy input would need to be 12 MW_{peak} such that 40 MWh of hydrogen could be stored to avoid using the Grid as a reservoir. Better yet would be a heat storage tank underground to make use of renewable electricity generation not accepted by the electrolyser. Because green hydrogen should retail at £10/kg when refueling cars, it was estimated that the average surplus 10 MWh/day grid-fed at £50/MWh (i.e., £500) would generate £700,000/a from retail hydrogen at £10/kg, four times more than Grid receipts for feed-in of spare Keele electricity generated.

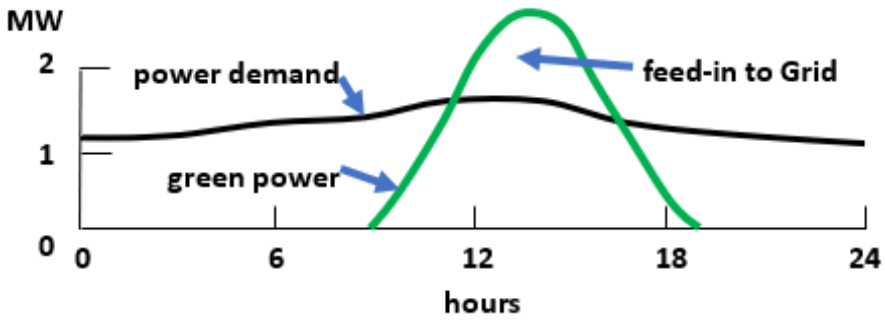

Figure 4. Smoothed Keele results [9] for 24 h on 27 September 2022 showing surplus green electricity fed-in to Grid when it could alternatively produce green hydrogen.

5. Moving to 100% green using hydrogen storage

Right now, Keele private wire community of 12,000 people is half-green and is paying back the original £8.1 M investment in about 4 years, owing to the approximate £2 M/a saved from utility bills. The prediction is that another £2 M/a will be saved by installing 6 more MW of renewable electricity, with a predicted similar payback time. However, investment cost must rise because more green hydrogen needs to be produced by electrolysis to give energy storage supplying days of stored energy which can drive campus buildings through CHP driven by fuel cells when wind and solar inputs are low. Going from the 3 MW electrolyser needed now to 10 MW in 2025 will utilise most of the excess renewable electricity, more than

absorbed by buildings and vehicles, producing stored hydrogen gas in bigger low-pressure containers. Typically, the electrolyser can then be run for about 12 h per day when sun and wind are good, manufacturing 2000 kg/day of green hydrogen worth £20000/day at retail (£3.6 M/a). The extra equipment requiring investment includes the electrolyser, storage, hydrogen pipes and fuel cells in buildings. Further excess electricity production can be stored in a hot water tank for heating buildings.

The key point about the Keele proposed plant is that it uses only renewable electricity that would have returned to the grid at £0.05/kWh and so can produce green hydrogen at a low electricity cost of £2/kg, contrasting with £8/kg for Grid electricity at Tyseley station (**Figure 1(a)**) [9]. This high Grid electricity price dominates hydrogen cost, with the other costs mainly for electrolyser, compressors and storage tanks. The conclusion is that green hydrogen can be produced at Keele community site at a cost near £5/kg whereas the existing Tyseley refueller (**Figure 1**) makes un-green hydrogen costing about £12/kg, leading to £23/kg price for consumers at retail.

6. Comparing green vehicle and buildings model with the UK government plan

If the Keele community project can be completed to approach 100% green, with hydrogen used as the major energy storage medium on-site, and an attractive pay-back time of about 4 years, then it is timely to consider the benefits of multiplying this technology across the UK.

Recent analyses of the existing Government plan to supply UK electricity from extensive offshore wind farms [13] suggest that the green energy for 2035 is planned to be transmitted along the National Grid to all citizens, or converted to hydrogen that can be piped across the country. This sounds fine but there are substantial difficulties that must be considered: First, the chemical industry already makes by-product hydrogen using grid electricity which needs to go green at low cost [14]; Second, there are only about 100 km of UK hydrogen pipelines at present, but it is believed that 2000 km of the natural gas pipes could be repurposed to convey hydrogen instead [15]; Third, the National Grid pylon network would need to expand by a factor 5 to carry all the electricity required to power transport, buildings and industries that currently use petroleum or gas. This erection of 80,000 unsightly new overhead cable structures could create a public backlash like that occurring in the 1940s when the original National Grid was established [16]. Both hydrogen pipes and electric cables are under consideration, but a key alternative is combined onshore wind turbines and solar farms banned by David Cameron in 2015 because he disliked their appearance. The dilemma this decade is choosing between pylons and turbines, which are discussed now.

7. Doubling onshore wind turbines or quadrupling pylons

The UK government effectively stopped wind turbines onshore in 2015. If a single person complained about a wind turbine, the installation could be halted, and planning consent deleted. Yet, the government now plans to double the number of National Grid pylons soon and is going ahead in 2023 [17]. There will probably be a

negative reaction to this from the public, many of whom are concerned about living near transmission lines [18]. Keele University installed its 2 MW of wind turbines by reducing their height, hiding them behind trees and responding to answer all complainants. They also installed the solar farm shown in **Figure 5** without serious questions from the public.

Figure 5. The Keele renewable generator equipment shows the two small wind turbines generating 2 MW, plus the solar panel array contributing 4.4 MW.

Pylons in the UK number around 22,000, far more than the 10,000 onshore wind turbines approved before the 2015 ban. Yet, the British government has produced a model of the UK running completely on grid electricity and therefore is beginning to erect between 2 and 5 times more pylons because the grid must replace both natural gas and petroleum to achieve net zero by 2050. The plausible outcome of this policy is that 80,000 pylons might be required, to be detested by many citizens (**Figure 6)**

Instead of considering a logical scheme for distributed power based on local energy sources like solar and wind within every community, the utility companies are planning to continue the 20th-century concept of hundreds of remote power plants feeding the national wire grid, rather than millions of renewable generators on all buildings, University sites, industry parks, retail areas, etc. [19].

In this paper, we suggest that hydrogen vehicles will be distributed across the UK, leading to a requirement for thousands of distributed green hydrogen refueling stations on private wire sites, each containing a 5 MW wind turbine and 5 MW of solar panels, modelled on the Keele experiment. 10,000 such filling stations would produce green hydrogen for communities, buildings and vehicles, totalling 100 GW_{peak} of new clean peak power to replace fossil gas and petroleum. For large quantities of locally stored hydrogen, above 1 ton, regulations will need to be applied [20], depending on the analysis of future green hydrogen demand [21].

The map of **Figure 6** shows the UK Midlands problem, that almost no wind turbines exist in the Birmingham region, whereas Scotland and coastal areas have close access to green wind generated hydrogen, which should accelerate green-

hydrogen-transportation in those areas. The final tally of onshore wind turbines required to solve the UK green transport problem should reach 20,000 by 2035, still less than the existing 22,000 pylons, and far neater than the 80,000 new pylons predicted by the government eventually. Several solutions have been proposed to overcome this grid problem for charging millions of electric vehicles, but none have yet been demonstrated [22]. However, the future possibilities for green hydrogen have been discussed widely [10,11,21,23].

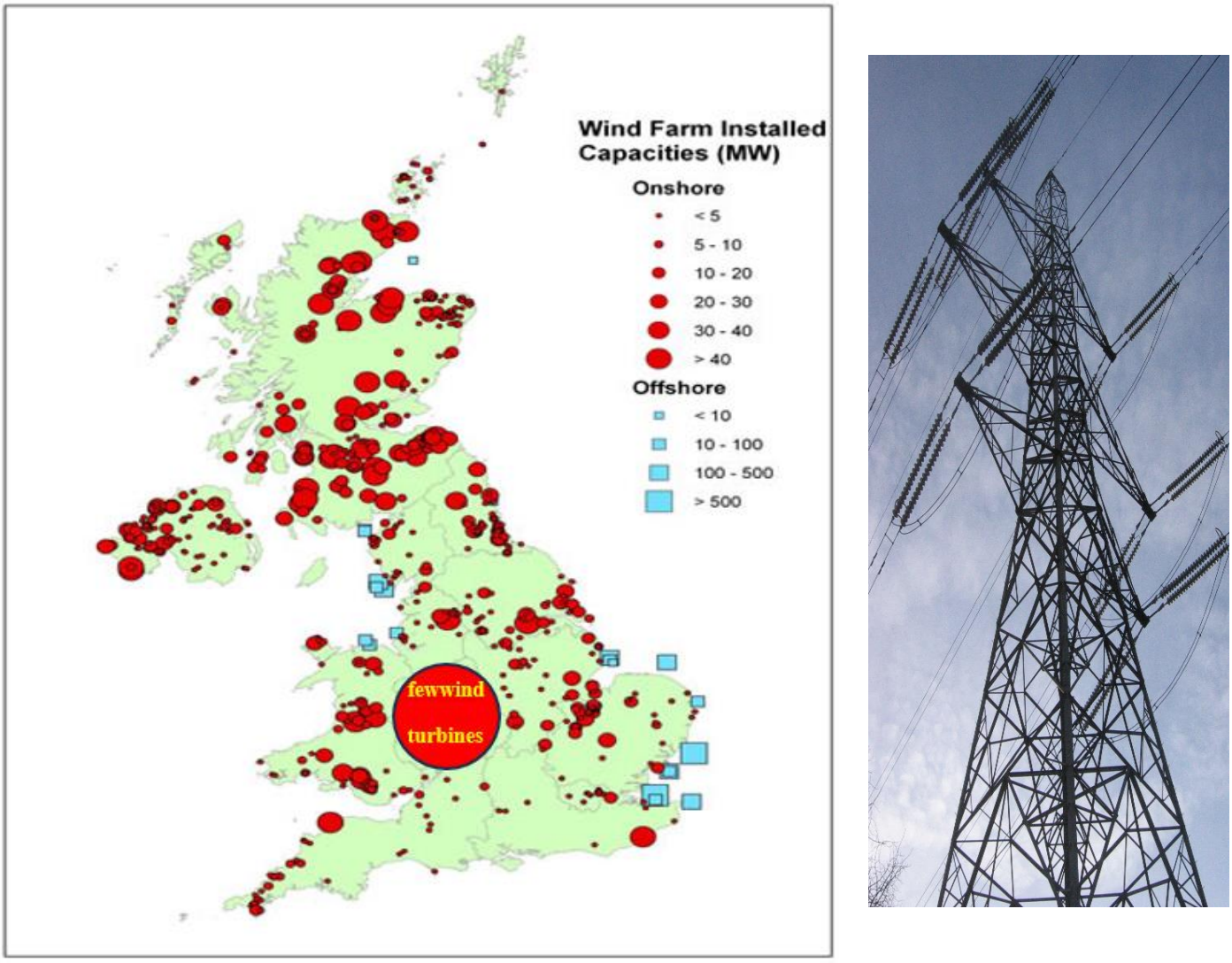

(a) **(b)**

Figure 6. (a) Map of onshore and offshore wind turbines across the UK showing the lack of wind power in the West Midlands [19]; **(b)** a typical Grid pylon in UK.

8. Conclusions

The existing UK electrical and hydrogen pipeline grids cannot develop fast enough to replace fossil energy by 2030. Therefore, it is essential now to consider distributed renewable electricity storing energy in hydrogen gas, because wind and solar are naturally spread thin on energy content while being the lowest cost generator installations. In such a distributed energy system, green hydrogen is the

ideal storage molecule that allows fluctuating renewables, wind, and solar, to be stored successfully and economically, powering vehicles and buildings, our main fossil carbon problem sectors.

The Keele private wire local community model has demonstrated that combined wind and solar energy can power the campus, potentially using green hydrogen as the main storage medium, producing a new standard for energy prices, replacing the current UK grid support, which has prices among the highest in Europe, too high to manufacture competitive green hydrogen. Such local new private grids, wind-solar-electric combined with hydrogen storage, could power all UK vehicles and buildings without major increases in the grid pylon numbers.

If this Energy Community at Keele turns out to be an optimum dimension near 10 MW of wind/solar capacity, driving catalytic water electrolysers on peak renewable power, then it could be reproduced across the UK 10,000 times to power distributed vehicles and buildings giving 100 GW_{peak} of new UK power generation, with an estimated cost of £100 bn and payback time of around 4 years.

Funding: This research was funded by HydrogenUnited.org, a UK charity based in Birmingham, England.

Acknowledgments: Thanks are due to Dr Sharon George at Keele University for discussing this project with the author and explaining the Keele model.

Conflict of interest: The author declares no conflict of interest.

References

1. Kendall K. Green Hydrogen in the UK: Progress and Prospects. Clean Technologies. 2022, 4(2): 345-355. doi: 10.3390/cleantechnol4020020
2. Lobo RFM. A Brief on Nano-Based Hydrogen Energy Transition. Hydrogen. 2023, 4(3): 679-693. doi: 10.3390/hydrogen4030043
3. Geschwindt S. EU set to make solar panels mandatory. Available online: https://buildindigital.com/ (accessed on 27 May 2022).
4. Gill T. How many people have solar panels in the UK? Available online: https://www.theecoexperts.co.uk/solar-panels/popularity-of-solar-power (accessed on 28 January 2024).
5. La Camera F. Renewable Power Generation Costs in 2020. IRENA; 2021. pp. 1–179.
6. BEIS. UK energy in brief 2022. Available online: www.gov.uk/government/statistics/uk-energy-in-brief-2022 (accessed on 28 January 2024).
7. Quinn B, Davies R. UK poised to drop plans to replace home gas boilers with hydrogen alternatives. Available online: https://www.theguardian.com/environment/2023/jul/13/uk-poised-to-drop-plans-for-hydrogen-to-replace-natural-gas-in-homes (accessed on 28 January 2024).
8. BBC. Product life cycle. Available online: Product life cycle - Product - Higher Business management Revision - BBC Bitesize (accessed on 28 January 2024).
9. Kendall K. Economic green hydrogen for UK refueling stations and buildings. Renewable and Sustainable Energy. Published online 2023. doi: 10.55092/rse20240001
10. Jałowiec T, Grala D, Maśloch P, et al. Analysis of the Implementation of Functional Hydrogen Assumptions in Poland and Germany. Energies. 2022, 15(22): 8383. doi: 10.3390/en15228383
11. Wulf C, Kaltschmitt M. Hydrogen Supply Chains for Mobility—Environmental and Economic Assessment. Sustainability. 2018, 10(6): 1699. doi: 10.3390/su10061699
12. Fan Z, Cao J, Jamal T, et al. The role of 'living laboratories' in accelerating the energy system decarbonization. Energy Reports. 2022, 8: 11858-11864. doi: 10.1016/j.egyr.2022.09.046

13. Bamisile O, Hatton L, Jansen M, Staffell I. Enabling the UK to Become the Saudi Arabia of Wind? The Cost of Green Hydrogen from Offshore Wind. Energy Futures Lab; 2023.
14. Ostadi M, Paso KG, Rodriguez-Fabia S, et al. Process Integration of Green Hydrogen: Decarbonization of Chemical Industries. Energies. 2020, 13(18): 4859. doi: 10.3390/en13184859
15. McCarty M. National grid studying UK hydrogen pipeline network potential. Available online: https://pgjonline.com/news/2021/may/national-grid-studying-uk-hydrogen-pipeline-network-potential (accessed on 28 January 2024).
16. Pratley N. The next UK net zero battleground is electricity pylons. Available online: https://www.theguardian.com/business/nils-pratley-on-finance/2023/sep/26/the-next-uk-net-zero-battleground-is-electricity-pylons (accessed on 28 January 2024).
17. National Grid. Substations, pylons and overhead lines. Available online: https://www.nationalgrid.com/electricity-transmission/who-we-are/running-our-network/substations-pylons-and-overhead-lines (accessed on 28 January 2024).
18. Copes R, Barn P. Is living near power lines bad for your health? BC Medical J. 2008; 50(9): 494.
19. Kendall K. Midlands green hydrogen: Climate emergency-action expo. Available online: https://www.hydrogenunited.org/event-details/midlands-green-hydrogen-2030-climate-emergency-action-expo (accessed on 28 January 2024).
20. Majumder-Russell G, Rihoy C, Mitchell K. Hydrogen Law, Regulations and strategy in the UK. Available online: https://cms.law/en/int/expert-guides/cms-expert-guide-to-hydrogen/united-kingdom (accessed on 28 January 2024).
21. Yusaf T, Laimon M, Alrefae W, et al. Hydrogen Energy Demand Growth Prediction and Assessment (2021–2050) Using a System Thinking and System Dynamics Approach. Applied Sciences. 2022, 12(2): 781. doi: 10.3390/app12020781
22. Deilami S, Muyeen SM. An Insight into Practical Solutions for Electric Vehicle Charging in Smart Grid. Energies. 2020, 13(7): 1545. doi: 10.3390/en13071545
23. Guan D, Wang B, Zhang J, et al. Hydrogen society: from present to future. Energy & Environmental Science. 2023, 16(11): 4926-4943. doi: 10.1039/d3ee02695g

Mechanical Engineering Advances 2024, 2(1), 1140.
https://doi.org/10.59400/mea.v2i1.1140

Article

The main distinguishing characteristic of active vibration control

Zine Ghemari*, Salah Belkhiri

Mohamed Boudiaf University of M'sila, Ichbilya street, M'sila 28000, Algeria
*** Corresponding author:** Zine Ghemari, zine.ghemari@univ-msila.dz

CITATION

Ghemari Z, Belkhiri S. The main distinguishing characteristic of active vibration control. Mechanical Engineering Advances. 2024; 2(1): 1140.
https://doi.org/10.59400/mea.v2i1.1140

ARTICLE INFO

Received: 11 November 2023
Accepted: 25 December 2023
Available online: 5 January 2024

Abstract: Active Vibration Control (AVC) stands out as a prominent technique in the realm of vibration mitigation and structural dynamics. Unlike passive vibration control methods that rely on dampers or isolators, AVC systems actively manipulate forces or motions within a structure in real-time to counteract undesirable vibrations. In this paper, the main distinguishing characteristic of AVC lies in its proactive approach, wherein control algorithms and actuators are employed to actively sense and respond to dynamic changes in the system. The application of Newton's second law allows a model of the vibration sensors operation, followed by simulations to improve their performance, which contributes to the advancement of the active vibration control system by enabling more precise detection and measurement of vibrations.

Keywords: vibration; sensors; active vibration control

1. Introduction

Vibration analysis for Active Vibration Control (AVC) is a critical aspect of the overall process, involving the assessment and monitoring of vibrations within a structure to inform the dynamic response of the Active Vibration Control system [1–6]. This analysis is essential for designing an effective AVC system and ensuring its optimal performance [7–12].

The process of vibration analysis begins with the strategic placement of sensors throughout the structure [13–18]. These sensors, including accelerometers, strain gauges, and displacement sensors, are selected and positioned carefully to capture comprehensive data on the structure's vibrations [19–22]. Continuously collecting real-time data on the vibrations, these sensors provide crucial information regarding amplitude, frequency, and phase, forming the basis for understanding the structure's dynamic behavior and designing an effective Active Vibration Control (AVC) system [23–29].

Vibration analysis entails conducting frequency analysis to identify the natural frequencies of the structure. This analysis helps in determining which frequencies contribute significantly to the vibrations, guiding the tuning of the AVC system to address specific resonant frequencies effectively. By leveraging the insights gained from vibration analysis, engineers can optimize the AVC system's performance and mitigate structural vibrations efficiently [30–32].

Vibrations in multi-story buildings pose a critical challenge to both structural integrity and occupant comfort. Dynamic forces from sources like wind, earthquakes, and machinery can lead to undesirable oscillations, necessitating advanced solutions for effective mitigation [33–35]. Active Vibration Control (AVC) has emerged as a sophisticated technology designed to address these concerns by actively counteracting vibrations in real-time. This article provides an insightful exploration into the

principles of Active Vibration Control and its specific application in three-story buildings [36–41].

In this examination, the article delves into the key components of Active Vibration Control, including sensors, actuators, and advanced control algorithms. The sensors, strategically placed within the building, continuously monitor vibrations, providing real-time data to the AVC system. Electromagnetic, hydraulic, or piezoelectric actuators generate forces to counteract detected vibrations, working in tandem to stabilize the structure. Advanced control algorithms, such as adaptive and predictive strategies, interpret sensor data to ensure precise and dynamic adjustments tailored to specific structural characteristics and environmental conditions [42–47].

The application of Active Vibration Control to a three-story building involves addressing structural resonance, wind-induced vibrations, seismic events, and internal sources of vibrations such as machinery. The technology actively identifies and counteracts resonant frequencies, minimizes wind-induced swaying, enhances seismic resilience, and improves overall occupant comfort by mitigating vibrations caused by internal sources [48–52].

As Active Vibration Control continues to evolve, its integration into building design and construction practices holds significant promise for creating safer, more resilient, and more comfortable structures. This abstract provides a comprehensive overview of the challenges associated with vibrations in multi-story buildings, the principles of AVC, and its specific application in mitigating vibrations in three-story structures [53–55].

2. Understanding active vibration control

The management of vibrations in structures is a critical consideration in the realm of engineering, particularly in the construction of multi-story buildings and industrial facilities. Active Vibration Control (AVC) has emerged as a cutting-edge technology aimed at addressing this challenge with unparalleled precision. By leveraging an intricate interplay of sensors, actuators, and advanced control algorithms, AVC represents a proactive and dynamic approach to counteract and minimize unwanted vibrations in real-time [56].

In stark contrast to passive damping systems, which dissipate energy after vibrations have already occurred, Active Vibration Control intervenes actively as vibrations happen. This proactive strategy enables the system to instantaneously counterbalance the forces responsible for the vibrations, providing a level of responsiveness and precision that traditional methods lack.

At the heart of AVC are sensors strategically placed within the structure to continuously monitor vibrations. These sensors, including accelerometers, strain gauges, and displacement sensors, generate real-time data essential for the system's timely response. Actuators, the driving force behind AVC, then come into play. Whether electromagnetic, hydraulic, or piezoelectric, these actuators generate forces to actively counteract and mitigate the detected vibrations [56].

The sophistication of Active Vibration Control is further emphasized by the implementation of advanced control algorithms. These algorithms interpret the data provided by sensors, determining the optimal response from the actuators. The

proactive nature of AVC, combined with these algorithms, allows for precise control and adjustment, enabling the system to address specific frequencies and amplitudes of vibrations with unparalleled accuracy (see **Figure 1**).

Figure 1. Active vibration control.

In this dynamic landscape of structural engineering, where the integrity of buildings and the comfort of occupants are paramount, Active Vibration Control stands out as a technology that goes beyond traditional passive solutions. This introduction sets the stage for a deeper exploration of the principles and applications of AVC, unveiling its potential to revolutionize the mitigation of structural vibrations and enhance the overall performance of diverse structures.

3. Importance of active vibration control

Active Vibration Control (AVC) plays a pivotal role in various industries and applications due to its significance in mitigating and managing unwanted vibrations in structures. The importance of Active Vibration Control is underscored by several key factors [57]:

Structural stability: Active Vibration Control is crucial for maintaining the structural stability of buildings and infrastructure. By actively countering and minimizing vibrations, it prevents long-term structural damage, ensuring the safety and durability of constructed assets.

Occupant comfort: Uncontrolled vibrations in structures can lead to discomfort for occupants, particularly in tall buildings or those situated in regions prone to seismic activity. AVC contributes to a more comfortable living and working environment by minimizing vibrations caused by external forces like wind or internal sources such as machinery.

Preservation of equipment and machinery: In industrial settings, vibrations can negatively impact the performance and longevity of machinery. Active Vibration Control helps preserve equipment by reducing dynamic forces, preventing premature wear and tear, and maintaining operational efficiency.

Enhanced performance in sensitive environments: In environments where precision is critical, such as laboratories or medical facilities, AVC is essential for protecting sensitive equipment from vibrations. This is crucial for applications where accurate measurements or delicate processes are integral to operations.

Seismic resilience: In earthquake-prone areas, AVC becomes a vital technology for enhancing a structure's resilience. By actively responding to seismic forces in real-time, it minimizes the potential damage caused by ground motion, ensuring the safety of occupants and protecting against structural failures.

Optimization of industrial processes: Active Vibration Control is instrumental in optimizing industrial processes by reducing vibrations that could affect manufacturing accuracy and efficiency. It contributes to smoother and more reliable production processes, minimizing disruptions and improving overall operational performance.

Compliance with regulations: Many industries are subject to regulations and standards related to vibrations to ensure the safety and well-being of occupants and the surrounding environment. AVC systems assist in meeting these regulatory requirements, preventing legal and safety issues.

Cost efficiency: While the initial investment in AVC systems may be substantial, the long-term benefits include significant cost savings. By minimizing structural damage, reducing maintenance costs, and prolonging the lifespan of equipment, AVC contributes to overall cost efficiency in both construction and industrial sectors.

4. Dynamic response spectrum

A dynamic response spectrum is a graphical representation of a structure's response to seismic ground motion over a range of frequencies [57]. This spectrum is a fundamental tool in structural engineering and earthquake analysis, providing a visual depiction of how a structure is likely to react to various seismic inputs (see **Figure 2**).

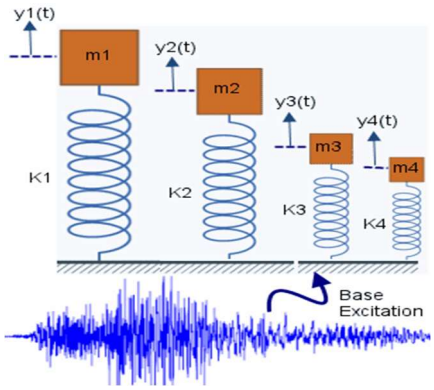

Figure 2. Structure is likely to react to various seismic inputs.

In simpler terms, the dynamic response spectrum illustrates how a building or structure responds to ground shaking at different frequencies during an earthquake. It plots the maximum responses, such as accelerations, velocities, or displacements, that the structure experiences at different natural frequencies [57–58].

The dynamic response spectrum is a graphical representation of how the structure responds to different frequencies of ground motion or external forces. Analyzing the dynamic response spectrum assists in identifying critical frequencies that need attention in the AVC system design (see **Figure 3**).

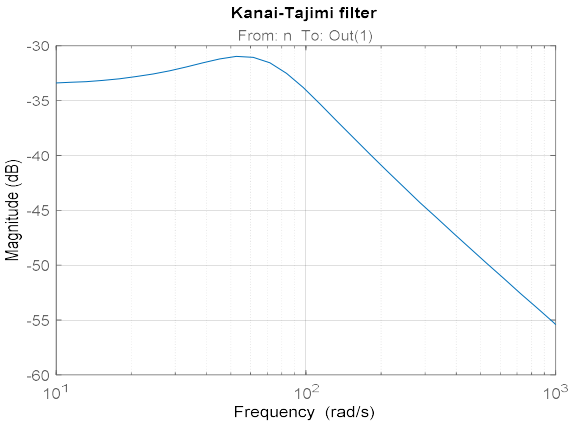

Figure 3. Response spectrum.

The horizontal axis of the spectrum represents the range of frequencies, while the vertical axis depicts the corresponding response amplitudes. Engineers use this information to assess the vulnerability of a structure to different seismic frequencies, aiding in the design and optimization of structures for earthquake resistance.

Dynamic response spectra are crucial in seismic design because they help engineers understand the potential vulnerabilities and weaknesses of a structure under specific earthquake scenarios. By analyzing these spectra, engineers can make informed decisions about the design parameters and materials to enhance a structure's seismic resilience and ensure the safety of its occupants.

5. Components of active vibration control

Active Vibration Control (AVC) systems consist of several key components working in tandem to actively counteract and minimize unwanted vibrations in structures. These components include sensors, actuators, and control algorithms, each playing a crucial role in the overall functionality of the system.

5.1. Sensors

Sensors are integral to the Active Vibration Control system, as they continuously monitor and measure vibrations in real time. Various types of sensors, such as accelerometers, strain gauges, and displacement sensors, are strategically placed throughout the structure to capture data on the dynamic forces affecting the building. This real-time information is essential for the system to make prompt and accurate adjustments (see **Figure 4**).

Figure 4. Vibration sensor.

A vibration sensor is a sensor affixed directly to a vibrating structure to gauge its vibrations. Operating in tandem with the structure, it captures not the absolute movement $y(t)$ but rather the relative movement $z(t)$. This relative movement is subject to analysis to derive insights into the absolute movement [58].

The vibration sensor itself functions as a system, comprised of a mass, a spring, and a damper, denoted by m, K, and C, respectively.

The established accelerometer model operates on the fundamental principle of motion. This model, elaborated in references [58], is expressed through Equations (1) and (2). The objective of this model is to enhance measurement accuracy by minimizing measurement errors to 1%, achieved through the judicious selection of the damping rate.

$$Z = Y\,\omega^2/\omega_n^2\,[(1-(\omega/\omega_n)^2)^2 + (2\zeta\omega/\omega_n)^2]^{1/2} \quad (1)$$

$$E = (\ddot{z}/\ddot{Y}) - 1 = [1/(1-(\omega/\omega_n)^2)^2 + (2\zeta\omega/\omega_n)^2] - 1 \quad (2)$$

Z: The relative movement modulus of the sensor; E: The measurement error; Y: The amplitude of movement; ξ: The damping rate, ω_n: The natural frequency of the sensor; ω: Relative frequency.

It's noteworthy that when the relative frequency value approaches the natural frequency of the accelerometer, a resonant frequency ($\omega = \omega_n$) emerges. To ensure proper accelerometer operation while averting resonance, it is imperative that the relative frequency remains equal to or less than one-third of the natural frequency ($\omega_n/3$). The selection of the accelerometer is contingent upon the gain of the vibration frequency.

In order to ascertain the most effective damping rate that minimizes measurement errors, two tests were systematically conducted. The outcomes of these tests were graphically represented in curves illustrating the sensor's damping rate.

In general, commercial accelerometers typically exhibit a damping rate of approximately 0.65, which effectively minimizes measurement error to a value equal to 2%. Damping is a critical characteristic of accelerometers, as it influences the sensor's ability to accurately measure vibrations. A damping rate of 0.65 indicates that the accelerometer's response to vibrations is sufficiently damped, allowing it to provide precise measurements while minimizing errors. This level of damping ensures that the accelerometer's output accurately reflects the true vibration levels experienced by the system under observation. Additionally, the 2% measurement error represents the degree of deviation between the accelerometer's measurements and the actual vibration levels, indicating a high level of accuracy and reliability in the sensor's performance. In this paper, by closely examining and comparing the data presented in **Figures 5** and **6**, it becomes evident that the optimal damping rate, which effectively limits the measurement error to 1%, is identified as 0.675. This specific damping rate has proven to be the most advantageous in achieving the desired precision and accuracy in measurements, making it the preferred parameter for optimizing the performance of the accelerometer in the given context.

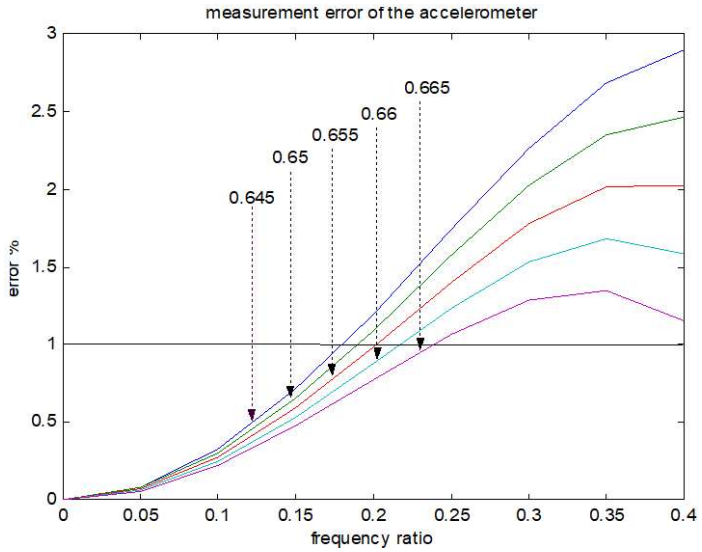

Figure 5. Results of first test.

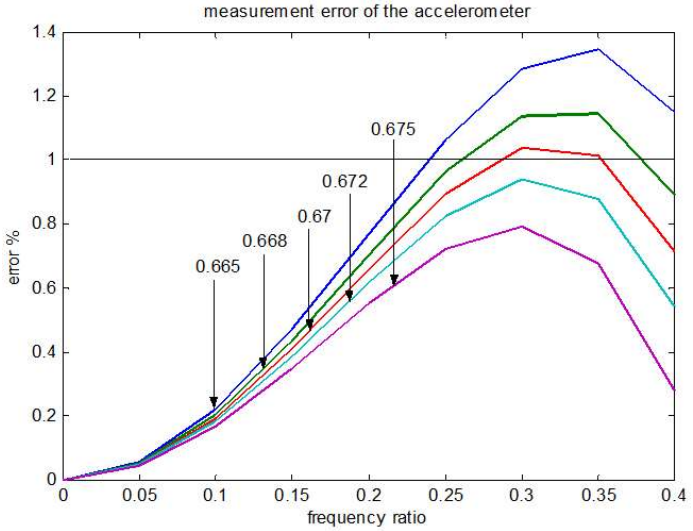

Figure 6. Results of second test.

From **Figures 5** and **6**, the acquired results have the potential to enhance measurement precision to its maximum capacity, thereby contributing to the advancement of accelerometer performance. By identifying and implementing the optimal damping rate, as determined through careful testing and analysis, the accuracy of measurements can be significantly improved. This improvement in precision is essential for obtaining reliable and precise data from the accelerometer, ultimately leading to enhanced performance in various applications and fields. The refined measurement precision ensures that the accelerometer operates at its best, providing more accurate and reliable information about the vibrations and movements of the monitored structure. This, in turn, supports the overall effectiveness and functionality of the accelerometer in its intended use.

The ultimate goal of this approach was to enhance the operation of the Active Vibration Control (AVC) system. By obtaining a precise and reliable mathematical model of the vibration sensor and ensuring high-precision measurement performance with low error, we were able to contribute to the overall improvement of the AVC

system. A more efficient and precise AVC system enables faster and more accurate detection and correction of undesirable vibrations, resulting in better protection of structures and equipment, reduced damage, and increased safety and reliability of the systems.

5.2. Actuators

Actuators are devices responsible for generating forces to actively counteract the detected vibrations. These devices come in different forms, including electromagnetic, hydraulic, and piezoelectric actuators, depending on the specific application and requirements [59,60]. Actuators are strategically positioned within the structure to apply dynamic forces that oppose and mitigate the effects of external and internal vibrations (see **Figure 7**).

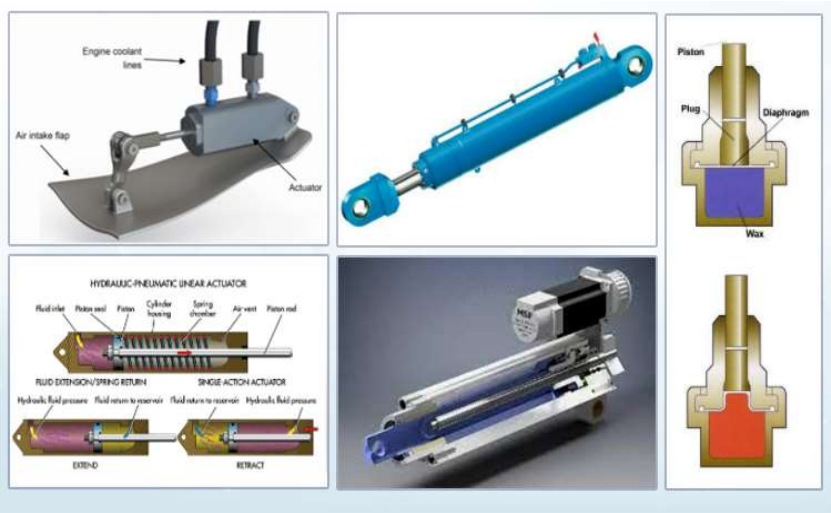

Figure 7. Different type of actuators.

5.3. Control algorithms

The effectiveness of Active Vibration Control relies on advanced control algorithms. These algorithms interpret the data provided by the sensors and determine the appropriate response from the actuators. Two common types of control strategies are adaptive control and predictive control. Adaptive control allows the system to adjust its parameters based on changing conditions, while predictive control anticipates future vibrations, enabling proactive measures. These algorithms ensure precise and dynamic adjustments tailored to specific structural characteristics and environmental conditions (see **Figure 8**).

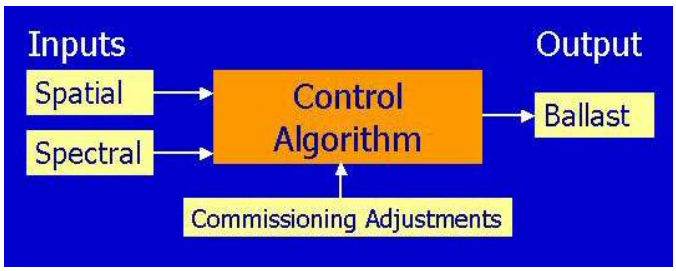

Figure 8. Control algorithms.

The collaboration of these components enables Active Vibration Control systems to function proactively in real-time. Sensors continuously gather data, control algorithms analyze this information, and actuators generate forces to actively counterbalance the forces causing vibrations. This holistic approach allows for precise control and adjustment, providing a highly effective solution to mitigate structural vibrations in diverse settings, from buildings to industrial facilities [61–63].

6. Conclusion

Vibration analysis for Active Vibration Control is a comprehensive process that involves sensor deployment, data collection, frequency and mode shapes analysis, dynamic response spectrum examination, algorithmic processing, and system design optimization. This meticulous analysis ensures that the AVC system is tailored to effectively counteract vibrations and enhance the structural performance of the targeted system or building.

In this study, we began by dissecting the operation of vibration sensors using fundamental principles of physics, notably Newton's second law. This law states that the force applied to an object is equal to the mass of the object multiplied by its acceleration. By applying this law to the context of vibration sensors, we were able to establish a mathematical model describing the relationship between the force applied to the sensor, its mass, and the acceleration it measures.

Once the mathematical model was established, we subjected it to simulation tests. These simulations allowed us to analyze the behavior of the sensor in various vibration scenarios and verify the validity of the model. We adjusted the parameters of the model to optimize the sensor's performance, aiming to minimize measurement error to a value below 1% and increase precision to 99%.

Author contributions: Conceptualization, ZG and SB; methodology, ZG; software, ZG; validation, ZG and SB; formal analysis, SB; investigation, ZG and SB; resources, ZG; data curation, ZG; writing—original draft preparation, ZG; writing—review and editing, ZG; visualization, SB; supervision, ZG; project administration, SB; funding acquisition, SB. All authors have read and agreed to the published version of the manuscript.

Conflict of interest: The authors declare no conflict of interest.

References

1. Ghemari Z, Saad S, Khettab K. Improvement of the Vibratory Diagnostic Method by Evolution of the Piezoelectric Sensor Performances. International Journal of Precision Engineering and Manufacturing. 2019; 20(8): 1361-1369. doi: 10.1007/s12541-019-00154-5
2. Reguieg SK, Ghemari Z, Benslimane T, et al. Modeling and Enhancement of Piezoelectric Accelerometer Relative Sensitivity. Sensing and Imaging. 2018; 20(1). doi: 10.1007/s11220-018-0222-y
3. Ghemari Z. Progression of the vibratory analysis technique by improving the piezoelectric sensor measurement accuracy. Microwave and Optical Technology Letters. 2018; 60(12): 2972-2977. doi: 10.1002/mop.31436
4. Ghemari Z. Study and analysis of the piezoresistive accelerometer stability and improvement of their performances. International Journal of System Assurance Engineering and Management. 2017; 8(S2): 1520-1526. doi: 10.1007/s13198-017-0622-8

5. Luo D, Hu T, Chang Y, et al. Second order linear active disturbance rejection control for active ultra-low frequency vibration isolation. In: Proceedings of the 2021 36th Youth Academic Annual Conference of Chinese Association of Automation (YAC); 28-30 May 2021; Nanchang, China. pp. 852-856. doi: 10.1109/yac53711.2021.9486609
6. Ma Z, Luo Y, Xie S, Zhang Y. Active Vibration Control of Cantilever Beam in fast Maneuvering Flight Environment. In: Proceedings of the 2022 16th Symposium on Piezoelectricity, Acoustic Waves, and Device Applications (SPAWDA); 10-14 October 2022; Nanjing, China. pp. 351-355. doi: 10.1109/SPAWDA56268.2022.10046023
7. Li M. Piezoelectric active vibration control method of rigid flexible hybrid manipulator based on PSO. In: Proceedings of the 2021 13th International Conference on Measuring Technology and Mechatronics Automation (ICMTMA); 16-17 January 2021; Beihai, China. pp. 431-435. doi: 10.1109/ICMTMA52658.2021.00099
8. Li S, Wang J, Yang M, et al. An Auxiliary Function-Based Active Vibration Control Scheme for Flexible Cantilever Beams Using Piezoelectric Actuators. In: Proceedings of the 2023 IEEE 3rd International Conference on Information Technology, Big Data and Artificial Intelligence (ICIBA); 26-28 May 2023; Chongqing, China. pp. 1553-1557. doi: 10.1109/ICIBA56860.2023.10165337
9. Lujin Z, Juan L, Ruikang Q, et al. Active Disturbance Rejection Vibration Control based on Delay Compensator for an All-Clamped Plate with Inertial Actuator. 2023 IEEE 12th Data Driven Control and Learning Systems Conference (DDCLS); 12-14 May 2023; Xiangtan, China. pp. 899-903. doi: 10.1109/ddcls58216.2023.10166276
10. Ghemari Z, Belkhiri S. Mechanical Resonator Sensor Characteristics Development for Precise Vibratory Analysis. Sensing and Imaging. 2021; 22(1). doi: 10.1007/s11220-021-00361-3
11. Belkhiri S, Ghemari Z, Saad S, et al. Improvement of the Vibratory Analysis by Enhancement of Accelerometer Characteristics. Sensor Letters. 2020; 18(1): 39-42. doi: 10.1166/sl.2020.4185
12. Ghemari Z, Saad S. Development of measurement precision of sensor vibration. Journal of Vibration and Control. 2012; 19(10): 1480-1486. doi: 10.1177/1077546312445595
13. Reguieg SK, Ghemari Z, Benslimane T. Extraction of the relative sensitivity model and improvement of the piezoelectric accelerometer performances. In: Proceedings of the 2018 International Conference on Signal, Image, Vision and their Applications (SIVA); 26-27 November 2018; Guelma, Algeria. pp. 1-5. doi: 10.1109/siva.2018.8661159
14. Berta S, Goga V, Murin J. Active Vibration Damping of Cantilever Beam using LabVIEW. 2022 Cybernetics & Informatics (K&I); 11-14 September 2022; Visegrád, Hungary. pp. 1-6. doi: 10.1109/ki55792.2022.9925924
15. Suranek P, Sreethar S, Strambersky R. Experimental Model for Active Vibration Control on Lattice Structure. In: Proceedings of the 2021 22nd International Carpathian Control Conference (ICCC); 31 May-1 June 2021; Velké Karlovice, Czech Republic. pp. 1-4. doi: 10.1109/iccc51557.2021.9454629
16. Cui M, Tang W, Han Y, Li Z. Smart Active Vibration Control System Using Piezoelectric Materials. In: Proceedings of the 2020 Chinese Control and Decision Conference (CCDC); 22-24 August 2020; Hefei, China. pp. 2611-2615. doi: 10.1109/CCDC49329.2020.9164082
17. Xin Z, Gao D, Lu S, et al. Research of Active Vibration Control for Cantilever Beam Based on Macro Fiber Composite Actuators. In: Proceedings of the 2022 International Conference on Cyber-Physical Social Intelligence (ICCSI); 18-21 November 2022; Nanjing, China. pp. 573-577. doi: 10.1109/ICCSI55536.2022.9970636
18. Yan H, Zhang C, Wang G. Experimental Study on Dual-channel Active Control Method for Transverse Vibration of Ship Propulsion Shaft System. In: Proceedings of the 2023 7th International Conference on Transportation Information and Safety (ICTIS); 04-06 August 2023; Xi'an, China. pp. 1353-1356. doi: 10.1109/ICTIS60134.2023.10243796
19. Ghemari Z, Saad S. Development of Model and Enhancement of Measurement Precision of Sensor Vibration. IEEE Sensors Journal. 2012; 12(12): 3454-3459. doi: 10.1109/jsen.2012.2210789
20. Ghemari Z. Improvement of the piezoelectric sensor by the progress of the measurement accuracy. In: Proceedings of the IEEE International Conference on Smart Materials and Spectroscopy (SMS'2018); 12-15 October 2018, Hammamet, Tunisia.
21. Ghemari Z, Saad S. The use of mechanical sensitivity model to enhance capacitive sensor characteristics. Analog Integrated Circuits and Signal Processing. 2019; 99(2): 349-357. doi: 10.1007/s10470-018-01383-w
22. Ghemari Z, Saad S. Enhancement of capacitive accelerometer operation by parameters improvement. International Journal of Numerical Modelling: Electronic Networks, Devices and Fields. 2019; 32(3). doi: 10.1002/jnm.2568

23. Ghemari Z, Salah S, Defdaf M. Appropriate Choice of Damping Rate and Frequency Margin for Improvement of the Piezoelectric Sensor Measurement Accuracy. Journal of Advanced Manufacturing Systems. 2021; 20(3): 537-548. doi: 10.1142/s0219686721500256
24. Ghemari Z, Saad S. Parameters improvement and suggestion of new design of capacitive accelerometer. Analog Integrated Circuits and Signal Processing. 2017; 92(3): 443-451. doi: 10.1007/s10470-017-0970-y
25. Ghemari Z, Saad S, Amrouche A, et al. New model of piezoelectric accelerometer relative movement modulus. Transactions of the Institute of Measurement and Control. 2014; 37(8): 932-941. doi: 10.1177/0142331214549572
26. Khot SM, Yelve NP, Kumar P. Investigation on Performances of Different types of Classical Controllers in Active Vibration Control. In: Proceedings of the 2021 4th Biennial International Conference on Nascent Technologies in Engineering (ICNTE); 15-16 January 2021; NaviMumbai, India. pp. 1-6. doi: 10.1109/ICNTE51185.2021.9487586
27. Rodriguez-Torres A, Morales-Valdez J, Yu W. Active Vibration Control for Building Structures based on $\mathscr{H}\infty$ Synthesis Problem. In: Proceedings of the 2020 17th International Conference on Electrical Engineering, Computing Science and Automatic Control (CCE); 11-13 November 2020; Mexico City, Mexico. pp. 1-6. doi: 10.1109/CCE50788.2020.9299118
28. Du L, Ji L, Luo Y, et al. Simulation and Experiment of an Active-Passive Isolator for Micro-Vibration Control of Spacecraft. In: Proceedings of the 2020 15th Symposium on Piezoelectrcity, Acoustic Waves and Device Applications (SPAWDA); 16-19 April 2021; Zhengzhou, Henan Province, China. pp. 227-232. doi: 10.1109/SPAWDA51471.2021.9445543
29. Che B, Huang Y, Chen L. Simulation and Experimental Research on Adaptive Active Vibration Control for Test Model in wind tunnel. In: Proceedings of the 2021 33rd Chinese Control and Decision Conference (CCDC); 22-24 May 2021; Kunming, China. pp. 1134-1139. doi: 10.1109/CCDC52312.2021.9601472
30. Ghemari Z, Saad S. Modeling and enhancement of mechanical sensitivity of vibration sensor. Journal of Vibration and Control. 2013; 20(14): 2234-2240. doi: 10.1177/1077546313486507
31. Ghemari Z, Chouaf F, Saad S. New Formula for the Piezoresistive Accelerometer Motion Acceleration and Experimental Validation. Journal of Advanced Manufacturing Systems. 2017; 16(1): 57-65. doi: 10.1142/s0219686717500044
32. Ghemari Z, Saad S. Improvement of piezoresistive accelerometer performance. In: Proceedings of the 3rd International Conference on Systems and Control; 29-31 October 2013; Algiers, Algeria. pp. 759-762. doi: 10.1109/icosc.2013.6750943
33. Cai C, Zhao T. Active Vibration Control of Thin Plate Milling Using Piezoelectric Actuator. In: Proceedings of the 2021 4th World Conference on Mechanical Engineering and Intelligent Manufacturing (WCMEIM); 12-14 November 2021; Shanghai, China. pp. 62-69. doi: 10.1109/WCMEIM54377.2021.00022
34. Yatim HM, Darus IZM, Talib MHAb, et al. Active Vibration Control of Flexible Manipulator using Genetic Algorithm with Parameter Exchanger. In: Proceedings of the 2022 IEEE 8th International Conference on Smart Instrumentation, Measurement and Applications (ICSIMA); 26-28 September 2022; Melaka, Malaysia. pp. 232-236. doi: 10.1109/ICSIMA55652.2022.9928820
35. Muhammadistan, Wei T, Cao W, et al. Designing of Robust FeedForward Active Vibration Control System using Online-Secondary Path modeling with Variable Step Size. In: Proceedings of the 2020 17th International Bhurban Conference on Applied Sciences and Technology (IBCAST); 14-18 January 2020; Islamabad, Pakistan. pp. 285-289. doi: 10.1109/IBCAST47879.2020.9044582
36. Chang X, Xu W, Shao M, et al. Micro-vibration Active Control based on FXAPA algorithm. In: Proceedings of the 2021 40th Chinese Control Conference (CCC); 26-28 July 2021; Shanghai, China. doi: 10.23919/CCC52363.2021.9550252. pp. 712-716.
37. Ghemari Z. Upgrading of piezoresistive accelerometer response. In: Proceedings of the 2016 8th International Conference on Modelling, Identification and Control (ICMIC); 15-17 November 2016; Algiers, Algeria. pp. 544-547. doi: 10.1109/ICMIC.2016.7804172
38. Ghemari Z, Saad S. Reducing the Measurement Error to Optimize the Sensitivity of the Vibration Sensor. IEEE Sensors Journal. 2014; 14(5): 1527-1532. doi: 10.1109/jsen.2014.2298493
39. Ghemari Z, Saad S. Defects Diagnosis by Vibration Analysis and Improvement of Vibration Sensor Measurement Accuracy. Sensor Letters. 2019; 17(8): 608-613. doi: 10.1166/sl.2019.4118
40. Ghemari Z. Decrease of the resonance phenomenon effect and progress of the piezoelectric sensor correctness. In: Proceedings of the 2018 International Conference on Electrical Sciences and Technologies in Maghreb (CISTEM); 28-31 October 2018; Algiers, Algeria. pp. 1-5. doi: 10.1109/CISTEM.2018.8613612

41. Ghemari Z, Saad S. Simulation and Experimental Validation of New Model for the Piezoresistive Accelerometer Displacement. Sensor Letters. 2017; 15(2): 132-136. doi: 10.1166/sl.2017.3792
42. Saad S, Ghemari Z, Herous L, Hadjadj OE. Transducer (Accelerometer) Modeling and Simulation. Asian Journal of Information Technology. 2007; 6(1): 54-57.
43. Lin X. Research on Active Micro Vibration Control Strategy Based on Variable Step FxLMS Algorithm. In: Proceedings of the 2023 2nd International Symposium on Aerospace Engineering and Systems (ISAES); 19-21 May 2023; Nanjing, China. pp. 167-172. doi: 10.1109/ISAES58852.2023.10281356
44. Tuma J, Strambersky R, Pavelka V. Modeling the Use of the Patch Piezo-Actuators for Active Vibration Control. 2021 22nd International Carpathian Control Conference (ICCC); 31 May-1 June 2021; Velké Karlovice, Czech Republic. pp. 1-4. doi: 10.1109/ICCC51557.2021.9454636
45. Zhang B, Dong W, Li X, et al. Design of Active-Passive Composite Vibration Isolation System of Magnetic Levitation and Spring Based on Fuzzy PID Control. 2020 Chinese Automation Congress (CAC); 6-8 November 2020; Shanghai, China. pp. 2381-2386. doi: 10.1109/CAC51589.2020.9326769
46. Yonezawa A, Yonezawa H, Kajiwara I. Vibration Control System Construction Method without Controlled Object Modeling. 2021 9th International Conference on Control, Mechatronics and Automation (ICCMA); 11-14 November 2021; Belval, Luxembourg. pp. 61-66. doi: 10.1109/ICCMA54375.2021.9646195
47. Pavelka V, Suranek P, Strambersky R. Thin Plate Active Vibration Control. In: Proceedings of the 2021 22nd International Carpathian Control Conference (ICCC); 31 May-01 June 2021; Velké Karlovice, Czech Republic. pp. 1-4. doi: 10.1109/ICCC51557.2021.9454648
48. Ghemari Z, Lakehal A. Vibration sensor mechanical sensitivity improvement. 2014 International Conference on Electrical Sciences and Technologies in Maghreb (CISTEM); 3-6 November 2014; Tunis, Tunisia; pp. 1-5. doi: 10.1109/CISTEM.2014.7076933
49. Ghemari Z. Modeling, Simulation and Experimental Analysis of the Vibration Sensor (Accelerometer) [PhD thesis]. Université de M'sila; 2013.
50. Ghemari Z, Belkhiri S, Saad S. Improvement of the relative sensitivity for obtaining a high performance piezoelectric sensor. IEEE Instrumentation & Measurement Magazine. 2023; 26(4): 49-56. doi: 10.1109/mim.2023.10146563
51. Ghemari Z. Enhancement of the vibratory analysis technique by the accelerometer characteristics evolution. In: Proceedings of the 7th International Conference on Control Engineering & Information Technology; 24-26 October 2019; Tetouan, Morocco.
52. Ghemari Z, Belkhiri S, Saad S. A capacitive sensor with high measurement accuracy and low electrical energy consumption. Applied Physics A. 2023; 129(5). doi: 10.1007/s00339-023-06644-8
53. Liu A, Zhang X, Tong S. Active Vibration Control for Flexible High-Rise Building System based on PDE Model. In: Proceedings of the 2022 China Automation Congress (CAC); 25-27 November 2022; Xiamen, China. pp. 5981-5986. doi: 10.1109/CAC57257.2022.10055511
54. Wang Y. Design and implementation of a real-time control system for a piezoelectric semi-active vibration suppression technique. In: Proceedings of the 2021 8th International Forum on Electrical Engineering and Automation (IFEEA); 3-5 September 2021; Xi'an, China. pp. 111-115. doi: 10.1109/IFEEA54171.2021.00030
55. Shavaev AA, Girs RA, Yakhutlov UM, et al. Active Control and Management of Vibrations of the Manipulator Positioning System Structures. In: Proceedings of the 2021 International Conference on Quality Management, Transport and Information Security, Information Technologies (IT&QM&IS); 6-10 September 2021; Yaroslavl, Russian Federation. pp. 402-406. doi: 10.1109/ITQMIS53292.2021.9642821
56. Wang A, Xu X, Wang S, et al. Terminal Sliding Mode Control for Microgravity Electromagnetic Active Vibration Isolation System. In: Proceedings of the IECON 2023 49th Annual Conference of the IEEE Industrial Electronics Society; 16-19 October 2023; Singapore, Singapore. pp. 1-6. doi: 10.1109/IECON51785.2023.10312478
57. Yang X, Zou WT, Shi MC, et al. Theoretical and Experimental Research on Active Control by Piezoelectric Smart Disc Structure. In: Proceedings of the 2022 16th Symposium on Piezoelectricity, Acoustic Waves, and Device Applications (SPAWDA); 10-14 October 2022; Nanjing, China. pp. 28-32. doi: 10.1109/SPAWDA56268.2022.10045942
58. Ghemari Z, Belkhiri S, Morakchi MR. Improvement of the vibration analysis technique by optimizing the parameters of the piezoelectric accelerometer. In: Proceedings of the 2022 IEEE 21st international Conference on Sciences and Techniques of

Automatic Control and Computer Engineering (STA); 19-21 December 2022; Sousse, Tunisia. pp. 183-186. doi: 10.1109/STA56120.2022.10018991

59. Metin M, Yilmaz FC. Model Reference Adaptive Control of Vertical Vibrations of a High-Speed Railway Vehicle. In: Proceedings of the 2020 8th International Conference on Control, Mechatronics and Automation (ICCMA); 6-8 November 2020; Moscow, Russia. pp. 144-148. doi: 10.1109/ICCMA51325.2020.9301578
60. Xu H, Li J, Yang K, et al. Vibration Suppression of Active Magnetic Bearing System with Precise Frequency Estimation Method. In: Proceedings of the 2022 International Conference on Electrical Machines (ICEM); 5-8 September 2022; Valencia, Spain. pp. 171-177. doi: 10.1109/ICEM51905.2022.9910910
61. Xu T, Li F, Qian F, et al. Youla Parameterized Adaptive Vibration Control for Vehicle Seats. In: Proceedings of the 2022 2nd International Conference on Consumer Electronics and Computer Engineering (ICCECE); 14-16 January 2022; Guangzhou, China. pp. 408-411. doi: 10.1109/ICCECE54139.2022.9712775
62. Wang W, Zhang S, Wu X. Active Vibration Suppression of Floating Wind Turbine Based on Fuzzy PID Controller. In: Proceedings of the 2023 IEEE/IAS Industrial and Commercial Power System Asia (I&CPS Asia); 7-9 July 2023; Chongqing, China. pp. 681-686. doi: 10.1109/ICPSAsia58343.2023.10294553
63. Zhu W, Zong Q, Tian B, et al. Disturbance Observer-Based Active Vibration Suppression and Attitude Control for Flexible Spacecraft. IEEE Transactions on Systems, Man, and Cybernetics: Systems. 2022; 52(2): 893-901. doi: 10.1109/tsmc.2020.3010518

Mechanical Engineering Advances 2024, 2(1), 1214.
https://doi.org/10.59400/mea.v2i1.1214

Article

Simulations of the operation of the fast light innovative regional train from "Serbian Railways" in traction and electric braking mode

Branislav Gavrilovic[1,*], Vladimir Aleksandrovich Baboshin[2]

[1] Department: Railway College, Academy of Technical and Art Applied Studies Belgrade, Zdravka Celara 14, 11000 Belgrade, Serbia
[2] Department of Reconstruction of Automation, Telemechanics and Communication Devices on Railways, Military Institute (Railway Troops and Military Communications), 190000 Sankt Peterburg, Russia
*** Corresponding author:** Branislav Gavrilovic, gavrilovicbranislav5@gmail.com

CITATION

Gavrilovic B, Baboshin VA. Simulations of the operation of the fast light innovative regional train from "Serbian Railways" in traction and electric braking mode. Mechanical Engineering Advances. 2024; 2(1): 1214. https://doi.org/10.59400/mea.v2i1.1214

ARTICLE INFO

Received: 25 August 2023
Accepted: 30 October 2023
Available online: 25 November 2023

Abstract: In the paper, the MATLAB-Simulink model of simulation of operation of the fast light innovative regional train from "Serbian Railways" in traction and braking mode is exposed where changes are observed: stator currents of three-phase traction motors, traction electric motor speeds and electric multiple units, electromagnetic torque on the rotor shaft of the traction electric motor, and direct current bus voltage. The model allowed review of the listed parameters for: different allowed values of contact network voltage and total voltage distortion at the place of connection of the electric multiple unit to the contact network; different mechanical loads of the electric multiple unit and traction electric motor; and different train speeds and rotations of traction electric motors. Appropriate conclusions were made through the analysis of the simulation results obtained.

Keywords: simulations; electric multiple unit; Serbian Railways

1. Introduction

The fast, light, innovative regional train "Serbian Railways" is a low-floor, four-part passenger train of "Serbian Railways" manufactured by the Swiss company Stadler (Company: Stadler Bussnang AG, Ernst-Stadler-Strasse 4, 9565 Bussnang, Schweiz). This fast, light, innovative regional train (FLIRT) is a specially designed electric multiple unit (EMU) of the latest generation, "FLIRT 3". At the beginning of 2014, twenty-one "FLIRT 3" were put into operation on the electric tracks of "Serbian Railways", and the procurement of thirty-one more is in progress (**Figure 1**) [1].

Figure 1. The fast, light, innovative regional train—FLIRT 3.

Basic technical data of the fast, light, innovative regional train "FLIRT 3" are shown in **Table 1** [1].

Table 1. Technical data.

Track gauge	1435 mm
Max velocity	160 km/h
Axle arrangement	Bo' 2' 2' 2' Bo'
Traction mode:	25 kV AC, 560 Hz
Maximum power on the wheel	1540 kW
Maximum starting tractive force	160 kN
Traction transformer—Main data	
Marked power	605 kVA
Maximum power per traction winding	500 kVA
Nominal voltage of traction windings	Approx. 25 kV/500 V and no load
Traction converter—Line inverter—AFE	
Input voltage	Approx. 500 VAC
Maximum input current	Approx. 1020 per AFE (2040 total)
Nominal DC-link	950 V (Under 1000 V)
Maximum output power	Approx. 525 per AFE (1050 total)
Bus capacity	85 mF
Train wide AFE synchronization	6 converters—3 EMU in multiple traction
Motor inverter—Traction three phase inverter	
Power in traction	385 kW (at wheel)
Output voltage traction	20 Hz to 120 Hz approx. from 211 V to 630 V 120 Hz to 215.7 Hz approx. 675V
Output maximum current	Approx. 780 Hz (700 Hz switching frequency)
Traction motor data	
Traction motor are three-phase asynchronous motors type	TMF 54-32-4
Continuous power	300 kW
Transmission ratio	1:5.9714

The traction equipment of the fast, light, innovative regional train "FLIRT 3" consists of:

- One pantograph for 25 kV AC.
- One traction transformer.
- Two power converters and four traction motors (2 traction motors per one power converter).
- Single-axle drive with three-phase asynchronous motors.

The traction motor is installed in the motor bogie. Wheelset axle shaft, traction motor, tooth coupling, and the gearbox together form an axle drive. There are two axle drives per motorbike. The traction motor transmits the torque to the gearbox through the tooth coupling transmission ratio of 1:5.9714. The gearbox transmits the drive torque through the wheelset axle shaft to the wheels and the tracks [1].

The traction system of the train is shown in **Figure 2**.

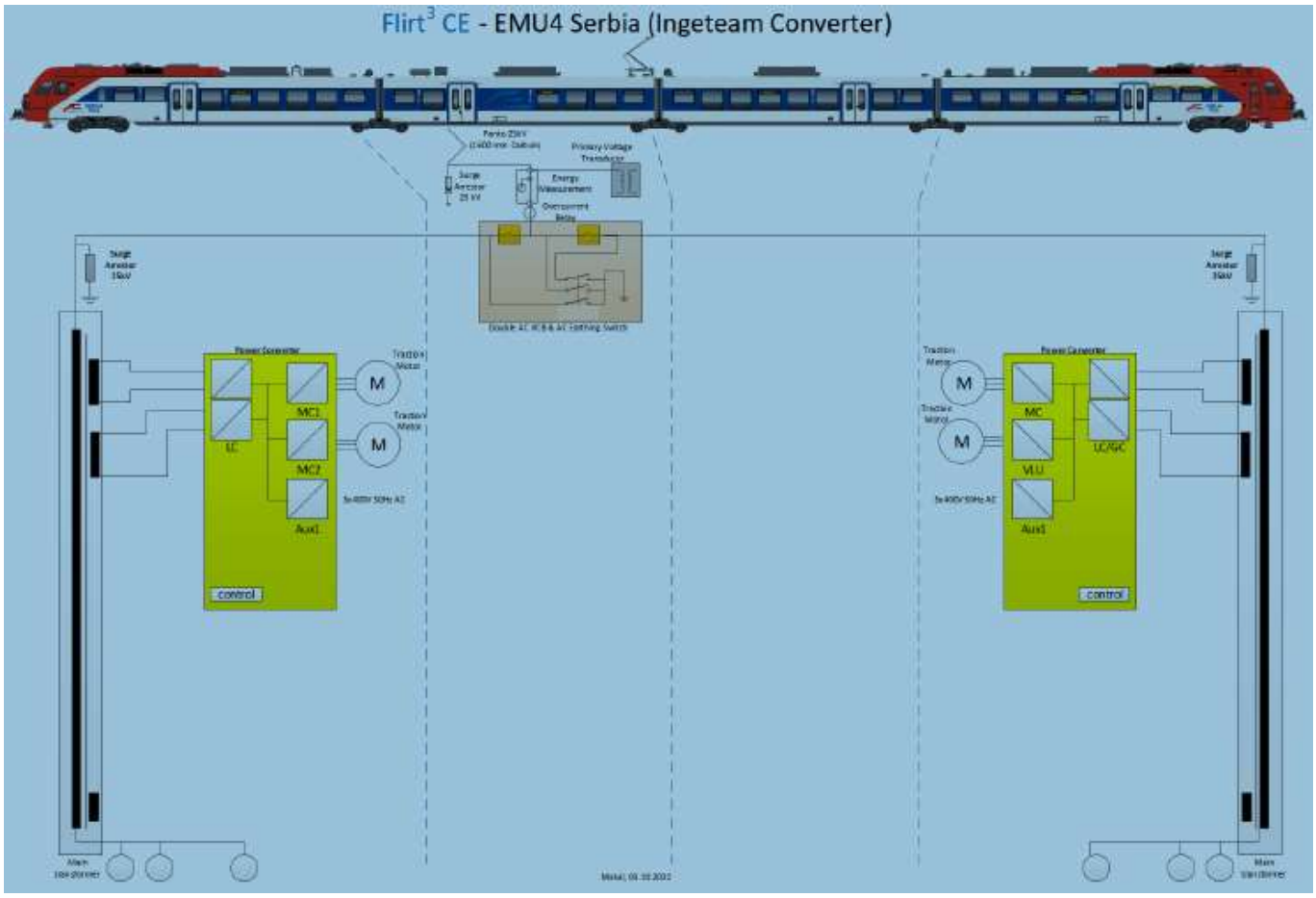

Figure 2. Principle circuit diagram main current of "FLIRT 3".

Figure 3 shows the tractive force-speed characteristics of the fast, light, innovative regional train "FLIRT 3" [1,2].

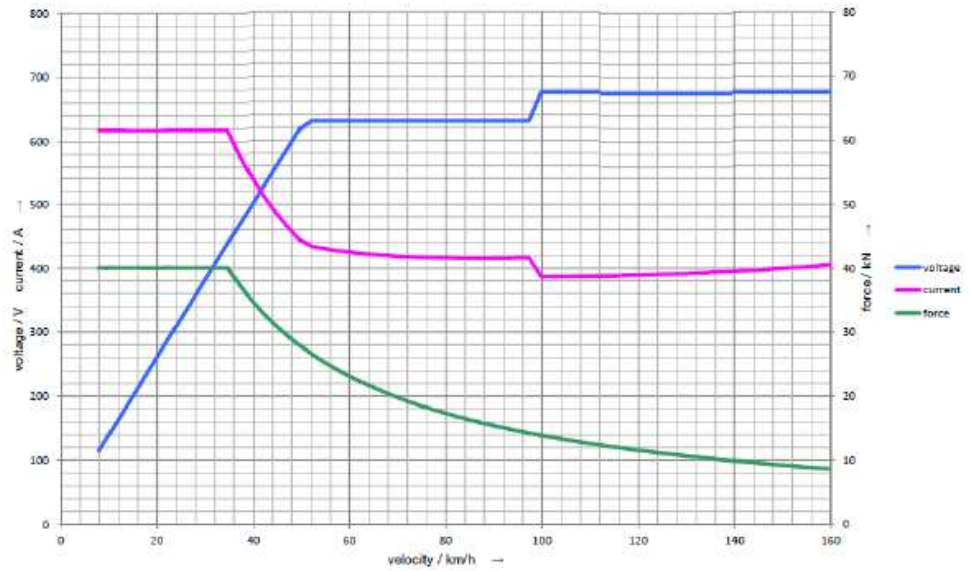

Figure 3. Traction force characteristic.

Figure 4 shows the power dependent on the line voltage of the fast, light, innovative regional train "FLIRT 3".

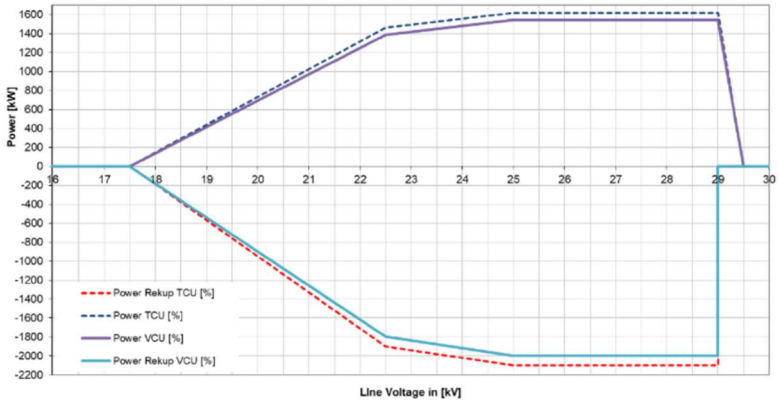

Figure 4. Power dependent on the line voltage.

2. Modeling "FLIRT 3" in MATLAB-Simulink

Modeling of the fast, light, innovative regional train "FLIRT 3" shown in MATLAB-Simulink is shown in the **Figure 5**.

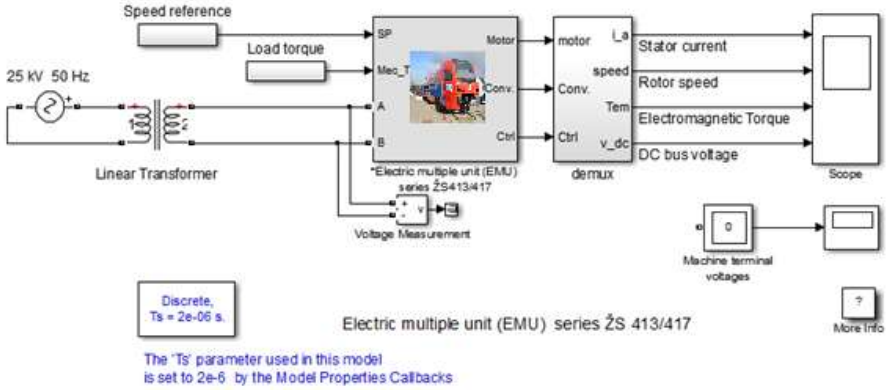

Figure 5. Simulink model of the fast, light, innovative regional train "FLIRT 3".

The high level block of the fast, light, innovative regional train "FLIRT 3" schematic shown below is built from six main blocks (**Figures 6** and **7**). The traction transformer, the induction motor, the three-phase inverter, and the mono-phase diode rectifier models are provided with the SimPowerSystems™ library. The speed controller, the braking chopper, and the DTC controller models are specific to the drive library.

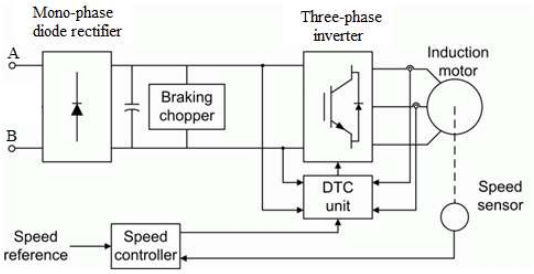

Figure 6. The high level block schematic of "FLIRT 3".

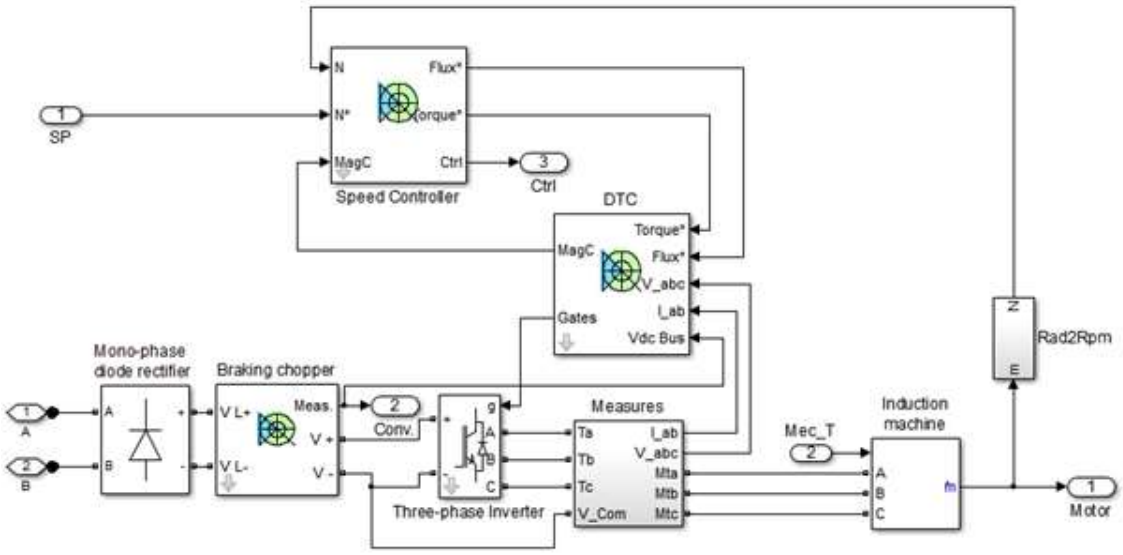

Figure 7. Simulink schematic of the fast, light, innovative regional train "FLIRT 3".

2.1. Speed controller

The speed controller is based on a PI regulator, shown below. The output of this regulator is a torque set point applied to the DTC controller block [3–15].

The high-level block diagram as well as the Simulink model of the speed controller are shown in **Figures 8** and **9** [3–15].

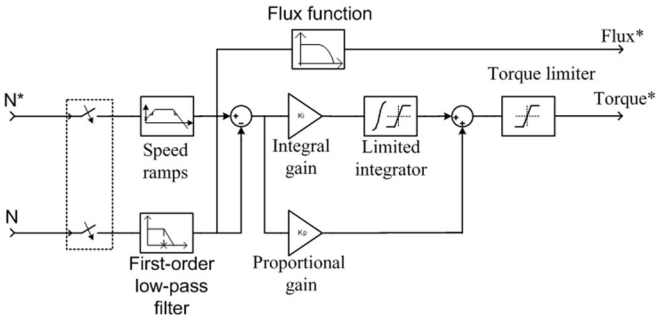

Figure 8. The high level block schematic of speed controller.

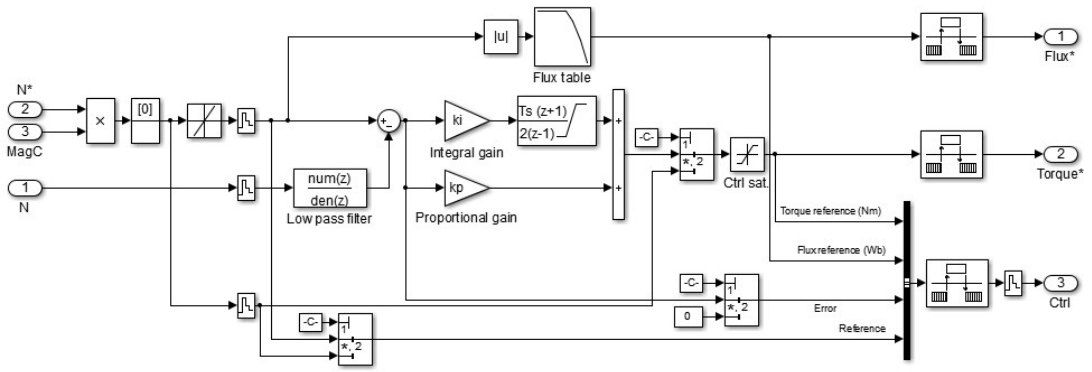

Figure 9. Simulink model of speed controller.

2.2. Braking chopper

The braking chopper block contains the DC bus capacitor and the dynamic

braking chopper, which is used to absorb the energy produced by a motor deceleration. The Simulink model of braking chopper is shown in **Figure 10** [3–15].

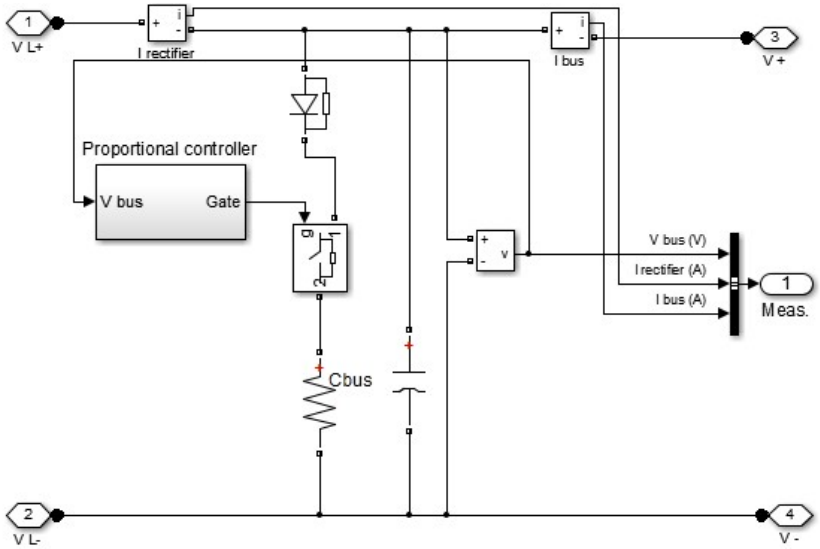

Figure 10. Simulink model of braking chopper.

2.3. DTC controller

The direct torque and flow control (DTC) controller contains five main blocks, shown in **Figure 11** [3–5].

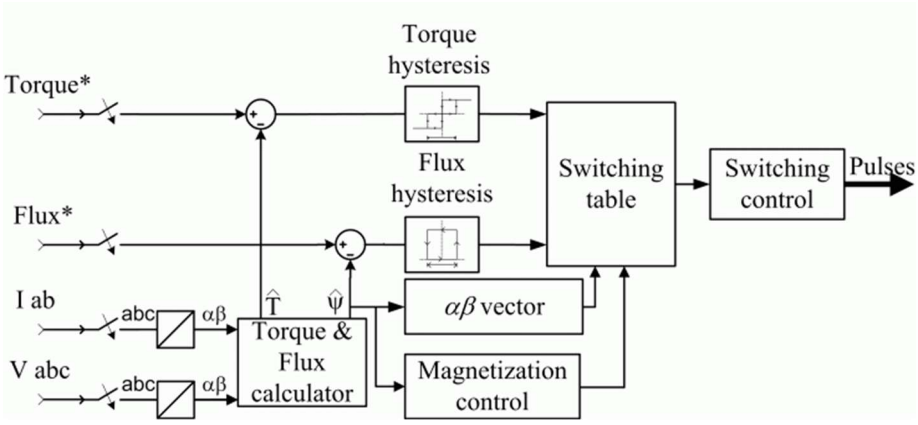

Figure 11. The direct torque and flow control (DTC) controller.

The torque & flux calculator block is used to estimate the motor flux $\alpha\beta$ components and the electromagnetic torque. This calculator is based on motor equation synthesis.

The $\alpha\beta$ vector block is used to find the sector of the $\alpha\beta$ plane in which the flux vector lies. The $\alpha\beta$ plane is divided into six different sectors spaced by 60 degrees.

The flux and torque hysteresis blocks contain a two-level hysteresis comparator for flux control and a three-level hysteresis comparator for torque control. The description of the hysteresis comparators is available below.

The switching table block contains two lookup tables that select a specific voltage vector in accordance with the output of the Flux & Torque Hysteresis comparators. This block also produces the initial flux in the machine.

The switching control block is used to limit the inverter commutation frequency to a maximum value specified by the user.

The high-level block diagram as well as the Simulink model of direct torque and flux control of the drive induction motor are shown in **Figures 11** and **12** [3–15].

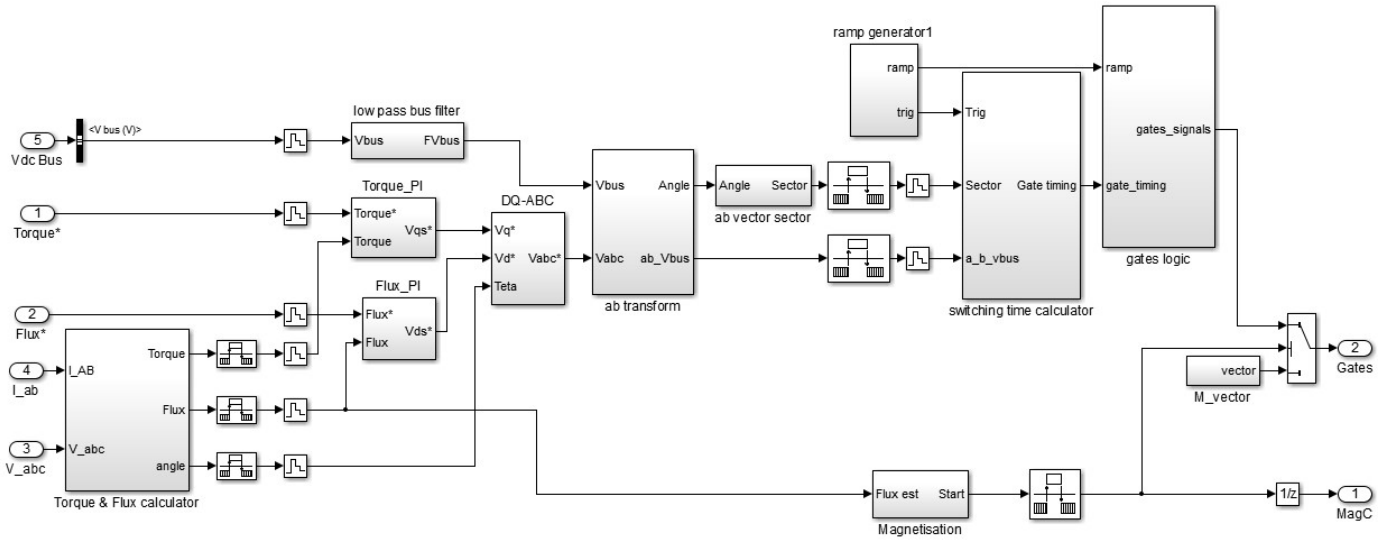

Figure 12. Simulink model of DTC (direct torque and flux control) of the drive induction motor.

2.4. Measurements

In this model, the voltage of the contact network at the connection point of the fast, light, innovative regional train "FLIRT 3" is taken as an input variable electrical quantity. This voltage can be changed within the limits of 17.5–27.5 kV according to the provisions of EN 50163. All other parameters of the Simulink model blocks are determined by the technical data of the train's devices and equipment. Electrical quantities that are measured during dynamic processes are: the stator current of the traction electric motor and the DC bus voltage converter.

The given input mechanical parameters of the model are: the desired final speed of rotation of the rotor of the traction electric motor (ω_r) and the resistive torque of the train movement (T_m). Mechanical quantities that are measured during dynamic processes and achieving the desired rotation speed are: the reverse electromagnetic torque of the traction electric motor (T_e) and the change in the rotation speed of the rotor of the traction electric motor (ω_r).

When calculating the reverse electromagnetic moment on the shaft of the traction electric motor (T_e), the equation of the dynamic balance of the train drive train was used [16–22].

$$T_e = J\frac{d}{dt}\omega_r + F\omega_r + T_m \quad (1)$$

wherein:

ω_r—speed of rotation of the rotor of the electric motor,

J—the moment of inertia of all rotating masses reduced to the rotor side of the electric motor,

F—coefficient of viscous friction,

T_m—resistance moments of movement reduced to the rotor side of the electric

motor.

By measuring and knowing the value of the reverse electromagnetic torque of the traction electric motor (T_e) and the change in the rotation speed of the rotor of the traction electric motor (ω_r), the traction force between the wheel and the rail (F_v), i.e., the translational speed of the train (v), is fully determined. The relationship between the rotating electromagnetic torque of the traction electric motor (T_e) and the traction force (F_v), i.e., the rotation speed of the rotor of the traction electric motor (ω_r) and the translation speed of the train (v), is given by the following Equation [2]:

$$F_v = \frac{2 \cdot i \cdot \eta}{D} \cdot T_e \; F_v = \frac{2i\eta}{D} T_e \tag{2}$$

$$v = \frac{D}{2i} \omega_r \tag{3}$$

wherein:

i—transmission ratio of the reducer (5.9714),

η—degree of utilization of the reducer (0.94),

D—the diameter of monobloc wheel (new/worn: 760/690 mm),

In order to monitor the change in stator current, rotation speed, and electromagnetic torque of the drive motor as well as DC bus voltage, a Simulink measurement block was modeled as in **Figure 13**.

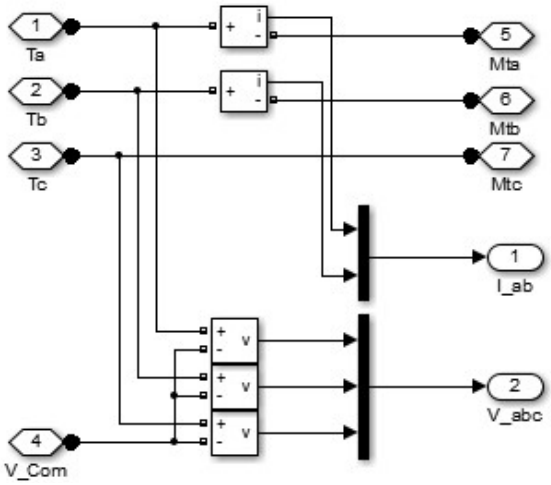

Figure 13. Simulink model of measures.

3. Results of simulations

Assuming that the given conditions are such that the fast, light, innovative regional train “FLIRT 3”.

- supplies with a stable sinusoidal voltage of 25 kV, 50 Hz,
- starts from rest at time t = 0 s: up to the speed of rotation of the electric motor (v = 90 km/h),
- load so that the resistance torque on the electric motor shaft is 792 Nm in an interval 0.5–1.5, and after 1.5 s it is equal to −792 Nm,
- starts braking from the moment t = 1 s. and so on.

The simulation results are given in **Figure 14**.

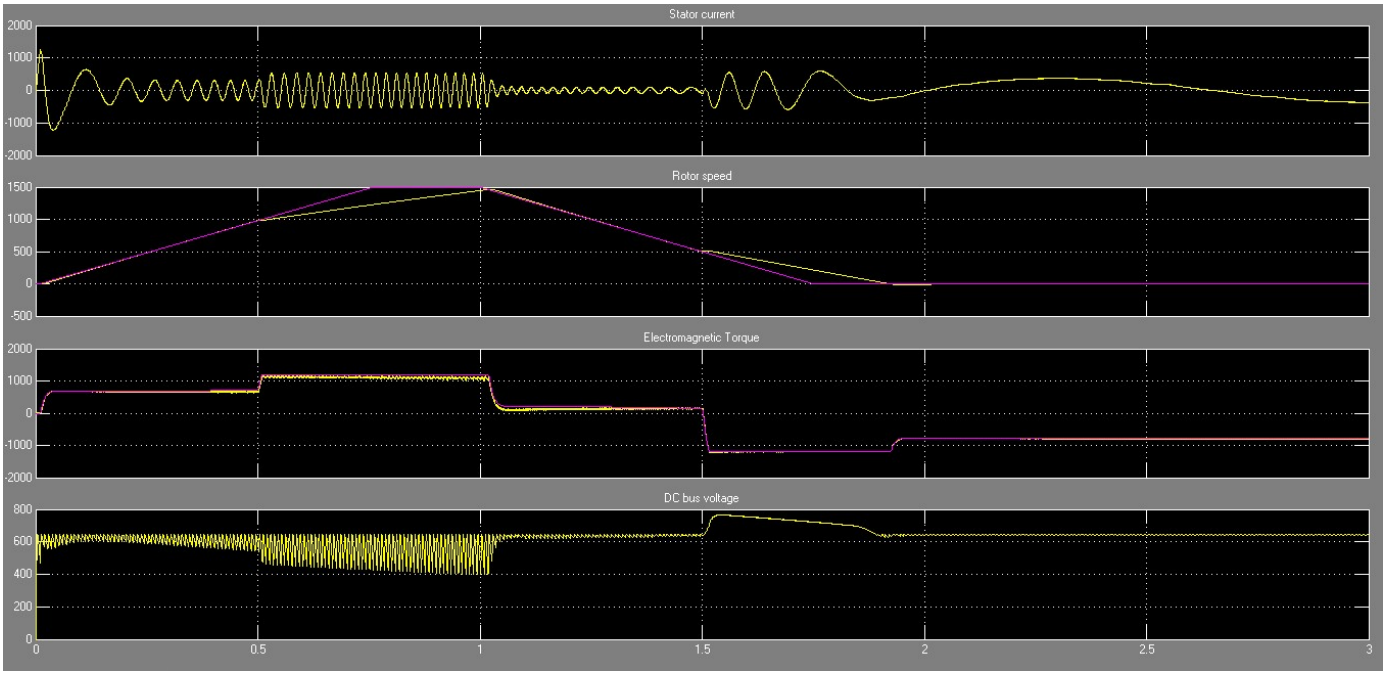

Figure 14. Changes in the stator current, rotation speed and electromagnetic moment of the electric motor and DC bus voltage of the direct current medium of the inverter FLIRT 3 for $\omega_r = 1500$ rpm and $T_m = \pm 792$ Nm.

The results shown in **Figure 14** were obtained after a number of running simulations with the initial conditions specified above. The version number of the software MATLAB-Simulink is 2013a (8.1.0.604, win 64, License Number: 8746166).

The simulation results show that the acceleration of the train up to t = 0.5 s is achieved with a constant electromagnetic moment on the electric motor shaft of $T_e = 810$ Nm, and when the load on the electric motor increased, the electromagnetic moment also increased to $T_e = 1050$ Nm. The speed of the electric motor $\omega_r = 1500$ rpm (v = 90 km/h) is reached at the moment t = 1 when braking starts until t = 1.75 s when the electric multiple unit stops. It is interesting to note that the speed of $\omega_r = 1500$ rpm is not reached before t = 1 s and if the limiters allow it even earlier. The rotating electromagnetic torque on the electric motor shaft is very small during braking in the interval from t = 1–1.5 s because the motor brakes due to the drag resistance of $T_m = +792$ Nm, and from t > 1.5 s a negative (braking) electromagnetic is generated the moment that overcomes the inertial drag resistance of $T_m = -792$ Nm, bringing the train to rest.

With these input parameters, the stator current of the electric motor does not exceed 1000 A, and the DC bus voltage is 800 V.

If the same input parameters of the system as in the previous example are assumed, but now with a new set speed of the electric motor of $\omega_r = 500$ rpm (v = 30 km/h), the change in the output values is shown in **Figure 15** (such conditions exist when the train driver wants to accelerate the train more slowly with the same traction resistances as in the previous example, but up to the train speed limit of v = 30 km/h).

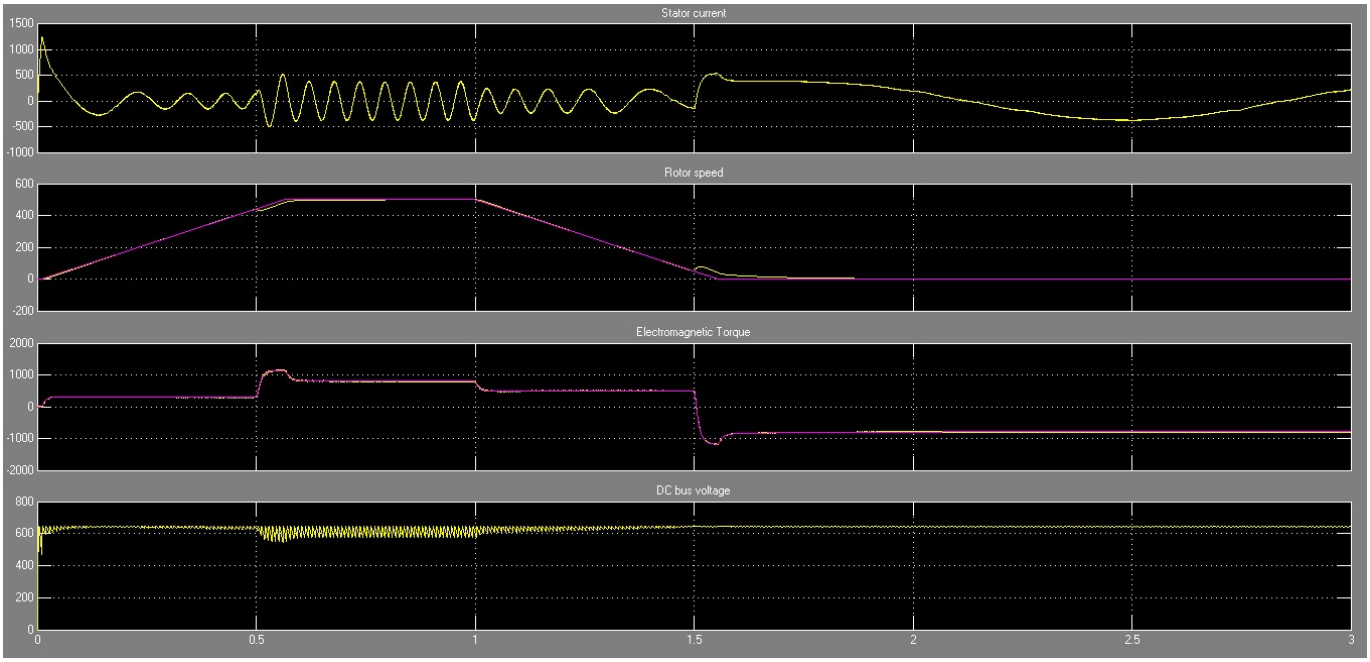

Figure 15. Changes in the stator current, rotation speed and electromagnetic moment of the electric motor and DC bus voltage of the direct current medium of the inverter FLIRT 3 for $\omega_r = 500$ rpm and $T_m = \pm 792$ Nm.

The results shown in **Figure 15** were obtained after a number of running simulations with the initial conditions specified above.

In this case, the starting of the electric motor from rest is done with a smaller electromagnetic moment $T_e = 200$ Nm until the moment t = 0.5 s when the electric motor is loaded with $T_m = 792$ Nm and increases to the value $T_e = 810$ Nm.

The set speed of $\omega_r = 500$ rpm (v = 30 km/h) is reached at the moment t = 0.6 s and is maintained until the moment t = 1 s when the start of braking is set. Braking starts with an electromagnetic torque T_e smaller than the positive resistive torque of $T_m = +792$ Nm and lasts until a complete stop at the moment t = 1.5 s. For $t > 1.5$ s the electric motor remains braked due to the generation of a negative electromagnetic moment T_e that overcomes the negative resistance of $T_m = -792$ Nm.

With these input parameters, the stator current of the electric motor does not exceed 600 A, and the DC bus voltage is 620 V.

Numerous simulations with the specified input parameters, but now with variable and permitted contact network voltage values of 19.5–27.5 kV and a total voltage distortion equal to or less than 8% (the European Standard SRPS EN 50162:2010), show the same or approximately the same change in output values as in **Figures 14** and **15**.

This fact indicates a very important feature of the fast, light, innovative regional train "FLIRT 3", which is that the train's electric traction drive has completely eliminated the influence of the contact network voltage. Due to the mentioned fact, it can be concluded that these electric multiple units represent a good driving railway solution.

The presented simulation results are fully confirmed with the experimental results presented in the literature [1].

It should be noted that the described MATLAB-Simulink model of the operation

simulation of the fast, light, innovative regional train “FLIRT 3” in the traction and braking mode enables the analysis of numerous other initial operating conditions related to the changing conditions of the train's power supply from the contact network, i.e., to changing conditions of the mechanical load of the train.

The described model enables the monitoring of changes in stator current, speed, and electromagnetic torque of traction motors for different permitted values and distortions of contact network voltage as well as for different mechanical loads during FLIRT 3 movement speed regulation.

4. Conclusion

The described simulation model completely objectively depicts the operation of the fast, light, innovative regional train “FLIRT 3” in traction and braking mode. The model made it possible to observe the electrical and mechanical parameters of the drive three-phase asynchronous motors for different permissible voltage values and voltage distortions at the point of connection of the multiple power unit to the contact network, different mechanical loads, and different rotation speeds of traction electric motors.

The described model enables the monitoring of changes in stator current, speed, and electromagnetic torque of traction motors for: different permitted values and distortions of contact network voltage as well as for different mechanical loads during FLIRT 3 movement speed regulation.

Numerous simulations show a very important feature of the electric multiple unit of the fast, light, innovative regional train “FLIRT 3”, which is that the vehicle's automatic regulation system has completely eliminated the influence of changing voltage value and voltage distortion in the contact network on the vehicle's operation. This stability of the drive to changes in voltage value and voltage distortion in the contact network is very important in the exploitation of railway electric traction vehicles and represents a special quality of this electric multiple unit.

The results of the simulations were fully confirmed by the experimental measurements performed at the fast, light, innovative regional train “FLIRT 3”.

Author contributions: Conceptualization, BG and VAB; methodology, BG; software, BG; validation, BG and VAB; formal analysis, BG and VAB; investigation, BG; resources, BG; data curation, BG; writing—original draft preparation, BG; writing—review and editing, BG; visualization, BG; supervision, BG; project administration, BG; funding acquisition, BG. All authors have read and agreed to the published version of the manuscript.

Conflict of interest: The authors declare no conflict of interest.

References

1. Stadler. Train Description- L-4547 Flirt 3 EMU Serbia. Document No PR_5382875. Stadler; 2023.
2. Gavrilovic B, Bundalo Z, Blagojevic Z. Regenerative braking of electric multiple unit serie 413/417 of joint stock company for passenger railway transport, Serbia Voz. In: Proceedings of the18th International Symposium INFOTEH-JAHORINA; 20-22 March 2019; Jahorina, Bosnia and Herzegovina.
3. Bose BK. Modern Power Electronics and AC Drives. Prentice-Hall; 2002.

4. Grelet G, Clerc G. Electric Actuators (French). Éditions Eyrolles, Paris; 1997.
5. Krause PC. Analysis of Electric Machinery. McGraw-Hill; 1986.
6. Gavrilovic BS. Research and Analysis in the Electric Traction System of the Serbian Railways. Eliva Press; 2023.
7. Boldea I, Nasar SA. Nasar: Electric Drives, 3rd ed. CRC Press; 2017.
8. Nondahl TA. Microprocessor Control of Motor Drives and Power Converters. IEEE Industry Application Society; 1993.
9. Bolton W. Mechatronics: Electronic Control Systems in Mechanical and Electrical Engineering, 3rd ed. Pearson Education; 2004.
10. Kaur H. Electric Drives and Their Controlling Techniques, 1st ed. Scholar's Press London; 2019.
11. Mohan N, Raju S. Analysis and Control of Electric Drives: Simulations and Laboratory Implementation. John Wiley & Sons; 2021.
12. Merabet A (editor). Advanced Control Systems for Electric Drives. MDPI; 2020.
13. Dorji C. Review of Electric Motor Drives. Available online: https://www.researchgate.net/profile/Cheku-Dorji-3/publication/282249201_REVIEW_OF_ELECTRIC_DRIVES/links/5a2657a80f7e9b71dd0a043f/REVIEW-OF-ELECTRIC-DRIVES.pdf (accessed on 12 November 2023).
14. Golnaraghi F, Kuo BC. Automatic Control Systems, 9th ed. John Wiley & Sons; 2010.
15. Kryukov OV, Blagodarov DA, Dulnev NN, et al. Intelligent Control of Electric Machine Drive Systems. 2018 X International Conference on Electrical Power Drive Systems (ICEPDS); 3-6 October 2018; Novocherkassk, Russia. pp. 1-4. doi: 10.1109/icepds.2018.8571670
16. Hughes A. Electric Motors and Drives—Fundamentals. In: Types and Applications, 3rd ed. Elsevier; 2006.
17. Schröder D. Electric Drives—Basics (German). Springer Berlin Heidelberg; 2007. doi: 10.1007/978-3-540-73005-7
18. Jauch C, Tamilarasan S, Bovee K, et al. Modeling for drivability and drivability improving control of HEV. Control Engineering Practice. 2018; 70: 50-62. doi: 10.1016/j.conengprac.2017.09.014
19. Brkić R, Adamović Ž, Bukvić M. Modeling of reliability and availability of data transmission in railway system. Advanced Engineering Letters. 2022; 1(4). doi: 10.46793/adeletters.2022.1.4.3
20. Hidirov S, Guler H. Reliability, availability and maintainability analyses for railway infrastructure management. Structure and Infrastructure Engineering. 2019; 15(9): 1221-1233. doi: 10.1080/15732479.2019.1615964
21. Mosayyebi M, Shakibian H, Azmi R. Statistical and Reliability Analysis of the Iran Railway System as a Complex Network. International Journal of Web Research. 2022; 5(1). doi: 10.22133/ijwr.2022.346545.1121
22. Adamović Ž, Josimović L. Technical Diagnostics. Society for Technical Diagnostics of Serbia; 2020.

Mechanical Engineering Advances 2024, 2(1), 1239.
https://doi.org/10.59400/mea.v2i1.1239

Article

Evaluating automobile's vibration in frequency domain

Yujie Jia[1,2], Vanliem Nguyen[1,2,*]

[1] School of Mechanical and Electrical Engineering, Hubei Polytechnic University, Huangshi 435003, China
[2] Hubei Key Laboratory of Intelligent Convey Technology and Device, Hubei Polytechnic University, Huangshi 435003, China
*** Corresponding author:** Vanliem Nguyen, xuanliem712@gmail.com

CITATION

Jia Y, Nguyen V. Evaluating automobile's vibration in frequency domain. Mechanical Engineering Advances. 2024; 2(1): 1239. https://doi.org/10.59400/mea.v2i1.1239

ARTICLE INFO

Received: 23 October 2023
Accepted: 1 December 2023
Available online: 15 December 2023

Abstract: Excitation of the low frequency not only influences the driver's health but also strongly affects the durability of the automobile's structures. To research the automobile's vibration in the low-frequency region, a dynamic model of the automobile is established to calculate the vibration equations of the automobile in the time region. Based on the theory of the Laplace transfer function, the automobile's vibration equations in the time region are transformed and converted to the automobile's vibration equations in the frequency region. Then, the effect of the automobile's design parameters and operation parameters on the characteristic of the automobile's acceleration-frequency is simulated and analyzed to evaluate the automobile's comfort as well as the durability of the automobile's structures in the frequency region. The research results show that the design parameters of stiffness, mass, and road wavelength remarkably affect the characteristic of the automobile's acceleration frequency. To reduce the resonant amplitude of the acceleration frequency in the vertical and pitching directions of the automobile, the stiffness parameters of the automobiles and tires should be reduced while the mass of the automobile's body should be increased. Additionally, the road's roughness also needs to be decreased, or the road's quality needs to be enhanced to reduce the resonant amplitude of the automobile's acceleration frequency.

Keywords: automobile's dynamic model; complex domain; ride comfort; frequency region

1. Introduction

The isolation systems of the automobile have been used to reduce the vibration excitations from the road surface transmitted to the automobile's body. In the design process of the vehicle's suspension systems, the structures of the suspension system were designed by the spring and damper with the stiffness parameter and damping parameter. The study showed that these parameters greatly affected the ride comfort of the vehicle [1]. In order to enhance the ride comfort of the vehicle or automobile, these design parameters were optimized by the genetic algorithm [2,3]. By searching for the best stiffness and damping parameters for the automobile's suspension systems, the automobile's ride comfort has been then improved in comparison with the passive suspension systems. However, the automobile's ride comfort was still low under the high speeds of the automobile's moving or the automobile's moving on the poor road surface roughness. Therefore, the automobile's suspension systems were improved by using the control damping forces of semi-active suspension systems [4,5] or semi-active air suspension systems [6]. The research results showed that with the control damping forces of the semi-active suspension systems used, the automobile's ride comfort was better than that of the automobile's optimal suspension systems under different operation conditions. However, the research also indicated that the control performance of the semi-active suspension systems strongly depended on the control

method and control rule of the algorithm programs [7,8]. To enhance the control performance, advanced control methods using the Adaboost algorithm and machine learning were applied [9,10]. In the above studies, the dynamic model was established to calculate the vibration equations of the automobile. Then, these vibration equations were built and simulated to compute the automobile's acceleration responses in the time region. The root mean square values of these acceleration responses were then computed to assess the automobile's ride comfort based on ISO 2631-1:1997 [11].

However, ISO 2631-1 showed that the ride comfort and health of the driver were also strongly affected by the vehicle's vibration excitations in the frequency region [11], especially at the excitations in the low frequency from 0.5 to 10 Hz of the road surface when the vehicle is moving. From the random excitations of the road surface built based on ISO 8068 [12], the interaction models of the vehicle and random road surface were established and studied the vibration of the vehicle or cab in the low frequency region [13,14]. Besides, the effect of the design parameters of the isolation systems on the vehicle's vibrations at low frequencies was also evaluated [15,16]. The results indicated that the density of resonant frequencies and resonant amplitudes of the automobile's acceleration-frequency response appeared very much in the low-frequency region, especially at excitations from 0.5 to 4.0 Hz. This not only affected the driver's health but also strongly affected the durability of the automobile's structures and road surfaces. Thus, the resonant frequencies and resonant amplitudes in the automobile's acceleration-frequency response in this excitation range needed to be minimized. These resonant frequencies and resonant amplitudes were directly impacted by the design parameters and operation parameters of the automobiles, such as the stiffness, mass, speed, road surface, etc. Therefore, the effect of the design parameters and operation parameters of the automobiles on the driver's health and the durability of the automobile's structures under different frequency excitations need to be researched and analyzed. However, this issue has not been considered in the existing research.

In the study of free vibrations of beam structures or doubly curved shell panels, the finite element method is applied to calculate the free vibrations of the models [17–20]. The finite element method easily determines the natural vibration frequencies of the structure to calculate the detailed durability. This method can also be applied to research the vibration of the automobile. However, the disadvantage of this method is that it is difficult to evaluate the influence of the automobile's dynamic parameters during movement. Therefore, to research the effect of the design parameters and operation parameters of the automobiles on the driver's health and the durability of the automobile's structures under different frequency excitations of the road surface, a dynamic model of the automobile is established to calculate its vibration equations in the time region. Based on the theory of the Laplace transfer function [21], the automobile's vibration equations in the time region are transformed and converted to the automobile's vibration equations in the frequency region. Then, the effect of the automobile's design parameters and operation parameters on the characteristic of the automobile's acceleration-frequency is simulated and analyzed to evaluate the automobile's ride comfort as well as the durability of the automobile's structures in the frequency region. Enhancing the working performance of the automobile is the goal of this study.

The practical significance of this research is that from the automobile dynamics model, the theory of the Laplace transfer function is applied to study the low-frequency vibrations of the automobile. The influence of automobile design parameters is evaluated in the low-frequency region. From the research results, the automobile's resonant frequencies are determined. This is the basis for determining initial parameters during the vehicle design process to reduce the resonance amplitude in the low-frequency region of the automobile. This can improve the ride comfort and structural strength of the automobile suspension system.

2. Automobile's mathematical model

2.1. Calculating the vibration equations of the automobile in the time region

In order to compute an automobile's vibration equations based on its actual structure, a 2-D automobile dynamics model is established and shown in **Figure 1**. Where four degrees of freedom of the automobile, including the automobile body's vertical vibration, automobile's pitch vibration, front axle's vibration, and rear axle's vibration, are defined by z, j, z_1, and z_2, respectively. The mass of the automobile's body, front axle, and rear axle are also defined by m, m_1, and m_2, respectively. The stiffness and damping parameters of the front and rear axles are also defined by $\{c_1$ and $k_1\}$ and $\{c_2$ and $k_2\}$. The stiffness and damping parameters of front and rear tires are also defined by $\{c_{t1}$ and $k_{t1}\}$ and $\{c_{t2}$ and $k_{t2}\}$. $l_{1,2}$ and $q_{1,2}$ are the distances and vibration excitations of the automobile and tires.

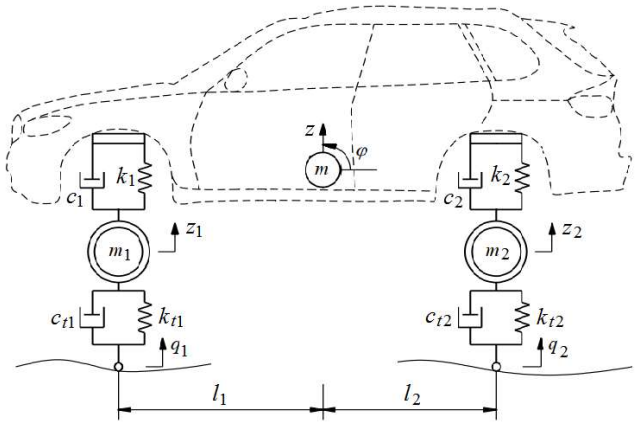

Figure 1. The dynamic model of the automobile.

The four degrees of freedom of the automobile, including the automobile body's vertical vibration, the automobile's pitch vibration, the front axle's vibration, and the rear axle's vibration, are defined by z, j, z_1, and z_2, respectively. The mass of the automobile's body, front axle, and rear axle are also defined by m, m_1, and m_2, respectively. The stiffness and damping parameters of the front and rear axles are also defined by $\{c_1$ and $k_1\}$ and $\{c_2$ and $k_2\}$. The stiffness and damping parameters of front and rear tires are also defined by $\{c_{t1}$ and $k_{t1}\}$ and $\{c_{t2}$ and $k_{t2}\}$. $l_{1,2}$ and $q_{1,2}$ are the distances and vibration excitations of the automobile and tires.

To facilitate the establishment of the vibration equations of the automobile, some

assumptions are made as follows: (1) The deformation of the automobile floor is very small; it is considered absolutely rigid. (2) Under vertical vibration excitation from the road surface when the automobile moves, the horizontal vibration of the automobile body is very small and is ignored. (3) The friction force of the automobile suspension and tires is very small, and it is calculated in the resistance force of the automobile suspension and wheels.

Therefore, from the automobile's dynamics model shown in **Figure 1**, its vibration equations are then written by:

$$\begin{cases} m\ddot{z}+(c_1+c_2)\dot{z}+(k_1+k_2)z+(c_1l_1+c_2l_2)\dot{\varphi}+(k_1l_1+k_2l_2)\varphi-c_1\dot{z}_1-k_1z_1-c_2\dot{z}_2-k_2z_2=0 \\ I\ddot{\varphi}+(c_1l_1^2+c_2l_2^2)\dot{\varphi}+(k_1l_1^2+k_2l_2^2)\varphi+(c_1l_1-c_2l_2)\dot{z}+(k_1l_1-k_2l_2)z-c_1l_1\dot{z}_1-c_1l_1z_1+ \\ +c_2l_2\dot{z}_2+c_2l_2z_2 \qquad =0 \\ m_1\ddot{z}_1+(c_1+c_{t1})\dot{z}_1+(k_1+k_{t1})z_1-c_1\dot{z}-k_1z-c_1l_1\dot{\varphi}-k_1l_1\varphi=c_{t1}\dot{q}_1+k_{t1}q_1 \\ m_2\ddot{z}_2+(c_2+c_{t2})\dot{z}_2+(k_2+k_{t2})z_2-c_2\dot{z}-k_2z+c_2l_2\dot{\varphi}+k_2l_2\varphi=c_{t2}\dot{q}_2+k_{t2}q_2 \end{cases} \quad (1)$$

In the research of the automobile's vibration, the automobile's vibration in the time region is mainly applied for assessing the automobile's comfort. However, based on ISO 2631-1:1997 [11], the automobile's vibration responses in the frequency region also greatly affected the ride comfort and structure in the automobile's systems. Therefore, in this study, the vibration characteristic of the automobile in the frequency region will be researched and evaluated under different operation conditions of the automobile.

2.2. Calculating the vibration equations of the automobile in the frequency range

To establish the automobile's vibration equations in the frequency region as well as evaluate the vibration characteristic of the car in the frequency region, based on the automobile's vibration equation in the time region in Equation (1), the Laplace transfer function [21] is then used to convert Equation (1) in the time region (t) to the image function (s) in the frequency region with the excitation frequency of ω. Herein, $\omega = 2\pi f$ and $s = d/\mathrm{d}t$.

The theory of the Laplace transfer function is described by: If a vibration function of $n(t)$ operates and depends on the variable time of $t > 0$ in its operation range defined by $\{a \text{ and } b\}$, based on the method of the Laplace transfer function, the image function of $n(t)$ defined by $N(s)$ is expressed as follows:

$$N(s) = \int_b^a e^{-st} n(t)\mathrm{d}t \,, s = i\omega \quad (2)$$

or

$$n(t) \to N(s) \quad (3)$$

Similarly, based on the theory of the Laplace transfer function, the derivative equations of the image function of $n(t)$, $\dot{n}(t)$, and $\ddot{n}(t)$ are also written by Dang [21]:

$$\begin{cases} n(t) \to N(s) \\ \dot{n}(t) \to sN(s) - N(0) \\ \ddot{n}(t) \to s^2N(s) - sN(0) - N(0) \\ \ldots \\ \dddot{n}^{(n)}(t) \to s^nN(s) - s^{n-1}N(s) - \ldots - N(0) \end{cases} \quad (4)$$

From the dynamic model of the car in **Figure 1**, at the initial condition of the automobile moving when $t = 0$, the vibration responses of the automobiles and front/rear wheel axles are equal to zero ($z(t) = 0$, $\varphi(t) = 0$, $z_1(t) = 0$, and $z_2(t) = 0$). Therefore, the derivative equations of their image function at the initial condition when $t = 0$ are also equal to zero ($N(0) = 0$).

Based on the Laplace transfer function in Equations (3) and (4), the derivative equations of the automobile body's vertical vibration $z(t)$, automobile body's pitch vibration $\varphi(t)$, front axle's vibration $z_1(t)$, and rear axle's vibration $z_2(t)$ calculated in Equation (1) at the time region are described by the image functions (s) of $Z(s)$, $\Psi(s)$, $Z_1(s)$, and $Z_2(s)$ in the frequency region as follows:

$$\begin{cases} z(t) \to Z(s) \\ \dot{z}(t) \to sZ(s) \\ \ddot{z}(t) \to s^2 Z(s) \end{cases}, \begin{cases} \varphi(t) \to \Psi(s) \\ \dot{\varphi}(t) \to s\Psi(s) \\ \ddot{\varphi}(t) \to s^2 \Psi(s) \end{cases}, \begin{cases} z_{1,2}(t) \to Z_{1,2}(s) \\ \dot{z}_{1,2}(t) \to sZ_{1,2}(s) \\ \ddot{z}_{1,2}(t) \to s^2 Z_{1,2}(s) \end{cases}, \text{ and } \begin{cases} q_{1,2}(t) \to Q_{1,2}(s) \\ \dot{q}_{1,2}(t) \to sQ_{1,2}(s) \end{cases} \tag{5}$$

Thus, the automobile's vibration equation of Equation (1) in the time region is rewritten by the automobile's vibration equation at the frequency range via the theory of Laplace functions as follows:

$$\begin{cases} a_{11}Z(s) + a_{12}\Psi(s) + a_{13}Z_1(s) + a_{14}Z_2(s) = 0 \\ a_{21}Z(s) + a_{22}\Psi(s) + a_{23}Z_1(s) + a_{24}Z_2(s) = 0 \\ a_{31}Z(s) + a_{32}\Psi(s) + a_{33}Z_1(s) + 0 = b_3 Q_1(s) \\ a_{41}Z(s) + a_{42}\Psi(s) + 0 + a_{44}Z_2(s) = b_4 Q_2(s) \end{cases} \tag{6}$$

By dividing Equation (6) by $Q_1(s)$, the matrix of Equation (6) has been rewritten by:

$$\begin{bmatrix} a_{11} & a_{12} & a_{13} & a_{14} \\ a_{21} & a_{22} & a_{23} & a_{24} \\ a_{31} & a_{32} & a_{33} & 0 \\ a_{41} & a_{42} & 0 & a_{44} \end{bmatrix} \begin{bmatrix} Z(s)/Q_1(s) \\ \Psi(s)/Q_1(s) \\ Z_1(s)/Q_1(s) \\ Z_2(s)/Q_1(s) \end{bmatrix} = \begin{bmatrix} 0 \\ 0 \\ b_3 \\ b_4 Q_2(s)/Q_1(s) \end{bmatrix} \tag{7}$$

where $s = i\omega$, $s^2 = -\omega^2$, $a_{11} = -m\omega^2 + (k_1 + k_2) + i(c_1 + c_2)\omega$, $a_{12} = (k_1 l_1 + k_2 l_2) + i(c_1 l_1 + c_2 l_2)\omega$, $a_{31} = a_{13} = -k_1 - ic_1\omega$, $a_{41} = a_{14} = -k_2 - ic_2\omega$, $a_{21} = (k_1 l_1 + k_2 l_2) + i(c_1 l_1 + c_2 l_2)\omega$, $a_{22} = -I\omega^2 + (k_1 l_1 l_1 + k_2 l_2 l_2) + i(c_1 l_1 l_1 + c_2 l_2 l_2)\omega$, $a_{32} = a_{23} = -k_1 l_1 - ic_1 l_1 \omega$, $a_{42} = a_{24} = -k_2 l_2 - ic_2 l_2 \omega$, $a_{33} = -m_1\omega^2 + (k_1 + k_{t1}) + i(c_1 + c_{t1})\omega$, $a_{34} = -m_2\omega^2 + (k_2 + k_{t2}) + i(c_2 + c_{t2})\omega$, $b_3 = k_{t1} + ic_{t1}\omega$, and $b_4 = k_{t2} + ic_{t2}\omega$, respectively.

Let $T_z = Z(s)/Q_1(s)$, $T_\varphi = \psi(s)/Q_1(s)$, $T_{z1} = Z_1(s)/Q_1(s)$, and $T_{z2} = Z_2(s)/Q_1(s)$, thus, T_z, T_φ, T_{z1}, and T_{z2} are defined as the vibration's transfer functions from the road to the automobile body and front/rear axles, respectively.

Based on the calculated results in the study of Dang [21], the result of the acceleration amplitude obtained via $T_n = \{T_z, T_\varphi, T_{z1}, \text{and } T_{z2}\}$ in Equation (7) under road's excitations $Q_1(s)$ are written as follows:

$$|\ddot{T}_n| = \omega^2 \sqrt{X_n^2 + Y_n^2} = \omega^2 f_n(\omega) \tag{8}$$

2.3. Road's excitations on car's wheels

When the automobile is traveling on the road, the vibration excitation of the road described by the harmonic function with its wavelength from 5 m to 10 m and its

height from 0.01 m to 0.012 m greatly affects the automobile's ride comfort and structure [12,22,23]. This harmonic function mainly causes resonant vibrations in the automobile's suspension system. Thus, this excitation is used to evaluate the vibration characteristic of the automobile at the frequency range. The road surface's vibration equation using the harmonic surface at time region has been described as:

$$q_1 = q_0 \sin \omega t = q_0 \sin(2\pi/T)t \quad (9)$$

With the frequency and wavelength of the road defined by L and l, Equation (9) is then rewritten in the traveling direction of X as follows:

$$q_1 = q_0 \sin L X = q_0 \sin(2\pi/l)X \quad (10)$$

With an unchanged speed of the automobile (v), thus, $X = vt$. Both Equations (9) and (10) are then rewritten by:

$$q_1 = q_0 \sin \omega t = q_0 \sin(2\pi v/l)t \quad (11)$$

The basic length of the automobile is defined by ($l_1 + l_2$), as shown in **Figure 1**, thus, the vibration excitation at the rear tire (q_2) calculated based on the vibration excitation at the front tire is expressed by:

$$q_2 = q_0 \sin \omega (t - t') = q_0 \sin \frac{2\pi v}{l_1 + l_2}(t - \frac{X}{v}) \quad (12)$$

From the ratio of q_2/q calculated based on Equations (11) and (12), the Laplace transformation T_q of q_2/q_1 is then described by:

$$T_q = Q_2(s)/Q_1(s) = \cos[2\pi(l_1 + l_2)/l] - i \sin[2\pi(l_1 + l_2)/l] \quad (13)$$

Equation (13) is then used as the vibration excitation of the automobile to evaluate the characteristic of the automobile's vibrations in the frequency region.

3. Simulation and analysis result

Based on the automobile's excitations using the road's harmonic function with q_0 = 10 mm and the road's wavelength l = 8 m as well as the dynamic parameters of the automobile listed in **Table 1**, the vibration characteristic of the automobile in the frequency region under the different operation conditions is then simulated and analyzed.

Table 1. Automobile's dynamic parameters.

Parameters	Values	Parameters	Values	Parameters	Values
m (kg)	1384	k_1 (N/m)	90,880	c_1 (Ns/m)	7733
m_1 (kg)	66	k_2 (N/m)	93,884	c_2 (Ns/m)	9804
m_2 (kg)	87	k_{t1} (N/m)	193,211	c_{t1} (Ns/m)	2000
I (kg·m^2)	11,632	k_{t2} (N/m)	226,422	c_{t2} (Ns/m)	2000
l_1 (m)	1.35	l_2 (m)	1.604	q_0 (mm)	10

3.1. Automobile's vibration characteristic under different stiffness of the suspension system

To evaluate the effect of stiffness parameters in the automobile's systems on the characteristic of the acceleration-frequency in the automobile, three different stiffness parameters of the automobile's suspension system, including K = [80%, 100%, 120%] × $\{k_{1,2}, k_{t1,2}\}$ are simulated when the automobile is traveling on the road surface with

the harmonic function of q_0 = 10 mm and wavelength l = 8 m at v = 20 m/s. Results in the acceleration-frequency of the automobile's body in the vertical and pitching vibrations have been shown in **Figure 2a**,**b**.

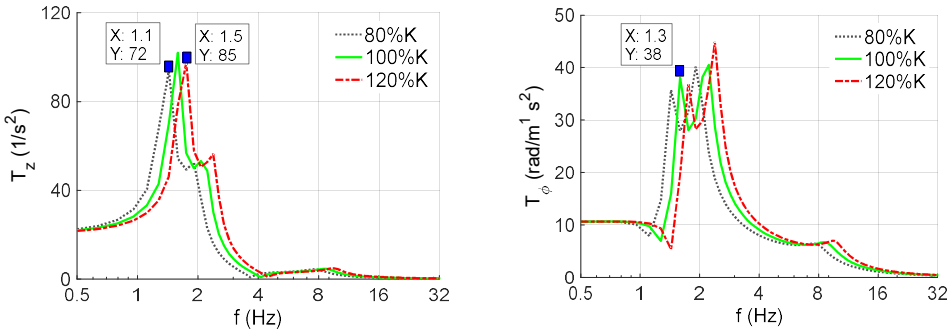

(a) **(b)**

Figure 2. The response of the automobile body's acceleration-frequency under different stiffness values; **(a)** the vertical acceleration-frequency; **(b)** the pitching acceleration-frequency.

The simulation results show that both the responses of the acceleration frequency of the automobile's body in the vertical and pitching directions are significantly affected by the different stiffness coefficients of the automobile's suspensions and wheels. Resonant frequencies in the vertical and pitching directions of the automobile in the low frequency region appeared at 1.1 Hz, 1.3 Hz, and 1.5 Hz when the stiffness parameters were reduced by 80% K, used by 100% K, and increased by 120% K, respectively. Additionally, the acceleration-frequency amplitude in the vertical and pitching directions of the automobile at low frequencies is also dependent on stiffness coefficients in the automobile's suspension systems and wheels. The automobile's acceleration-frequency amplitudes are increased with the increase of the stiffness parameters and vice versa. These results mean that the K of the automobile's suspensions and wheels not only influences the amplitude but also influences the resonant frequency of the automobile's acceleration frequency in both the vertical and pitching directions. In order to ameliorate the automobile's comfort as well as ensure the durability of the automobile's structures, the designed parameters in the stiffness of the automobile's suspensions and tires need to be chosen to minimize the amplitude of the automobile's acceleration frequency at resonant frequencies.

3.2. Automobile's vibration characteristic under different mass

The analysis results in Section 3.1 show that the automobile's acceleration-frequency amplitudes and resonant frequencies are affected by the stiffness parameters of the automobile. Besides, based on the formula used to determine the resonant frequency of the system, the resonant frequency is calculated by $f^2 = K/M$. Thus, the automobile's mass (M) is also influenced by the automobile's acceleration-frequency characteristic. To clearly illustrate this issue, the automobile's different masses, including M = [80%, 100%, 120%] × {m, m_1, m_2} are also simulated under the same excitation of the road surface in Section 3.1. The results of the acceleration-frequency of the automobile's body in the vertical and pitching vibrations are plotted in **Figure 3a,b**.

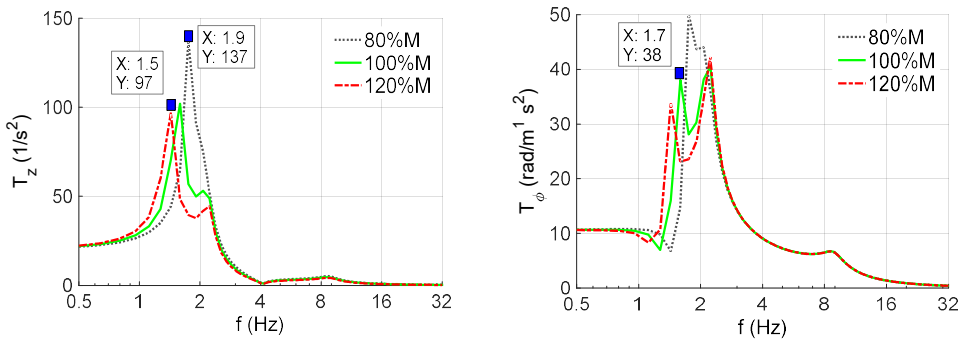

Figure 3. The response of the automobile body's acceleration-frequency under different load conditions; **(a)** the vertical acceleration-frequency; **(b)** the pitching acceleration-frequency.

The simulation results indicate that both the responses of the acceleration-frequency of the automobile's body in the vertical and pitching direction are also significantly affected by the different masses in the automobile's body and front/rear axles. The resonant frequencies in the vertical and pitching directions of the automobile in the low frequency region appear at 1.5 Hz, 1.7 Hz, and 1.9 Hz when the automobile's mass is increased by 120% *M*, used by 100% *M*, and reduced by 80% *M*, respectively. These resonant frequencies changed is due to the change of the automobile's mass under the same stiffness parameters of the automobile suspension system ($f = \sqrt{k/m}$). Besides, the amplitude of the acceleration-frequency in the vertical and pitching direction of the automobile in the low frequency region is also dependent on the automobile's mass. The automobile's acceleration-frequency amplitudes are increased when the automobile's mass is reduced and vice versa. This also means that the automobile's mass not only influences amplitudes but also influences resonant-frequencies of the automobile's acceleration frequency in both the vertical and pitching direction. The analysis results show that both the resonant frequencies and acceleration-frequency amplitudes of the automobile are mainly appeared in a low frequency region from 1.0 to 3.0 Hz under the effect of the automobile's mass. This frequency region greatly affects the driver's comfort and health, according to ISO 2631-1 [11]. In order to ameliorate automobile's comfort and ensure durability in the automobile's structures, in the design process of the automobile, both the mass *M* and stiffness *K* of the automobile's systems should be calculated and chosen to minimize the amplitude of the acceleration-frequency at the resonant frequencies.

3.3. Automobile's vibration characteristic under road's different wavelengths

In the automobile's condition traveling on the pavement, the road wavelength can affect the automobile's ride comfort. To clear this issue, three different wavelengths of the road, including l = 6 m, l = 8 m, and l = 10 m, at the same excitations of the road in Section 3.1, are simulated, respectively. The results of the acceleration-frequency of the automobile's body in the vertical and pitching vibrations are plotted in **Figure 4a,b**.

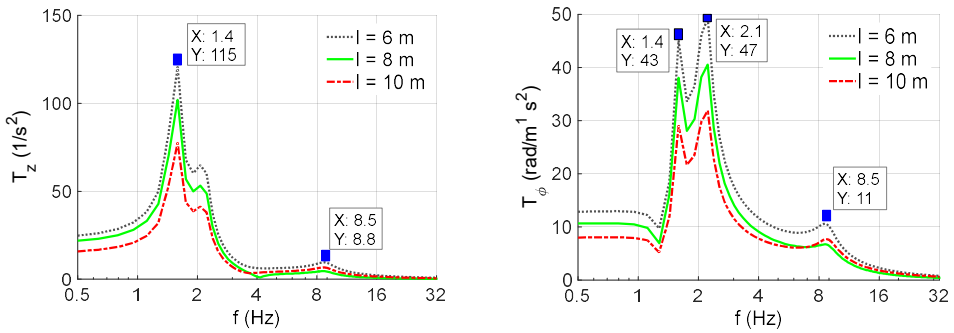

(a) **(b)**

Figure 4. The response of the automobile body's acceleration-frequency under road's different wavelengths; **(a)** the vertical acceleration-frequency; **(b)** the pitching acceleration-frequency.

Under the effect of the different wavelengths of the road surface, the simulation results in **Figure 4a,b** show that the resonant frequencies of the automobile's body in the vertical and pitching vibrations un-change and appear at 1.4 Hz, 2.1 Hz, and 8.5 Hz under the different values of the road wavelength. This means that the road wavelength does not influence the characteristics of the automobile's acceleration frequency. However, the amplitude of the acceleration-frequency in the vertical and pitching direction of the automobile in the low-frequency region is changed and affected by the road's different wavelengths. Their amplitude is increased when the road's wavelength is reduced, and vice versa. This is because the excitation frequency of the road surface wave length with l = 6 m nearly coincides with the natural frequency of the automobile suspension system, thus the automobile's acceleration frequency is increased. Thus, to reduce the amplitude of the acceleration-frequency in the vertical and pitching direction of the automobile, the road's wavelength needs to be increased. This means that the pavement's roughness needs to be decreased or the pavement's surface quality needs to be enhanced. In addition, during the road design process, the road surface wave length needs to be considered, limiting the road surface wave length to less than 6 m to reduce the resonance vibrations of vehicles when moving on the road surface. This contributes to improving vehicle comfort and structural durability and reducing the potential risk of traffic accidents. This issue is also proven and recommended in existing studies [24].

4. Conclusions

This study uses the complex-domain method for evaluating automobile's vibrations in the frequency region. The study can be summarized as follows:

The design parameters of stiffness, mass, and road wavelength remarkably affect the characteristics of the automobile's acceleration frequency.

To reduce resonant amplitudes of the automobile's acceleration frequency in both vertical and pitching directions, stiffness parameters in the automobile's suspensions and tires should be reduced while the mass of the automobile's body should be increased. However, the reduction of the stiffness of the automobile can lead to reduced stability and safety of movement of the automobile. To solve this issue, the automobile's suspension systems are researched and replaced by using air suspension

systems or active suspension systems.

The resonant amplitude of the acceleration-frequency in the vertical and pitching direction of the automobile is significantly affected by the road wavelength; thus, to reduce this resonant amplitude, the pavement's roughness needs to be decreased or the pavement's surface quality needs to be enhanced.

From the main findings of this study, the analysis of automobile vibrations in the low frequency region has shed light on the influence of automobile dynamic parameters such as automobile mass, suspension stiffness, and road surface wave length on the ride comfort of the automobile and the structural durability of the suspension system through the automobile's frequency-amplitude response. Therefore, the study method of automobile vibrations using the Laplace transfer function can be applied to research all multi-axle heavy trucks, commercial vehicles, or vibrating rollers. This is the advantage of this study.

Author contributions: study conception and design, YJ and VN; design of the vehicle model, simulation, analysis results, YJ; writing, VN. All authors have read and agreed to the published version of the manuscript.

Conflict of interest: The authors declare no conflict of interest.

References

1. Yang Y, Ren W, Chen L, et al. Study on ride comfort of tractor with tandem suspension based on multi-body system dynamics. Applied Mathematical Modelling. 2009; 33(1): 11-33. doi: 10.1016/j.apm.2007.10.011
2. Nariman-Zadeh N, Salehpour M, Jamali A, et al. Pareto optimization of a five-degree of freedom vehicle vibration model using a multi-objective uniform-diversity genetic algorithm (MUGA). Engineering Applications of Artificial Intelligence. 2010; 23(4): 543-551. doi: 10.1016/j.engappai.2009.08.008
3. Pekgökgöz R, Gurel M, Bilgehan M, et al. Active suspension of cars using fuzzy logic controller optimized by genetic algorithm. International of Journal Engineering Application Sciences. 2010; 2(4): 27-37.
4. Ghoniem M, Awad T, Mokhiamar O. Control of a new low-cost semi-active vehicle suspension system using artificial neural networks. Alexandria Engineering Journal. 2020; 59(5): 4013-4025. doi: 10.1016/j.aej.2020.07.007
5. Zhu Y, Bian X, Su L, et al. Ride Comfort Improvement with Preview Control Semi-active Suspension System Based on Supervised Deep Learning. SAE International Journal of Vehicle Dynamics, Stability, and NVH. 2021; 5(1). doi: 10.4271/10-05-01-0003
6. Wang H, Kin Wong P, Zhao J, et al. Observer-based robust gain-scheduled control for semi-active air suspension systems subject to uncertainties and external disturbance. Mechanical Systems and Signal Processing. 2022; 173: 109045. doi: 10.1016/j.ymssp.2022.109045
7. Félix-Herrán LC, Mehdi D, Rodríguez-Ortiz J de J, et al. H∞control of a suspension with a magnetorheological damper. International Journal of Control. 2012; 85(8): 1026-1038. doi: 10.1080/00207179.2012.674216
8. Maciejewski I. Control system design of active seat suspensions. Journal of Sound and Vibration. 2012; 331(6): 1291-1309. doi: 10.1016/j.jsv.2011.11.010
9. Wang L, Li J, Yang Y, et al. Active control of low-frequency vibrations in ultra-precision machining with blended infinite and zero stiffness. International Journal of Machine Tools and Manufacture. 2019; 139: 64-74. doi: 10.1016/j.ijmachtools.2018.11.004
10. Zhu T, Wan H, Wang Z, et al. Model reference adaptive control of semi-active suspension model based on adaboost algorithm for rollover prediction. SAE International Journal of Vehicle Dynamics, Stability, and NVH. 2022; 6(1): 71-86. doi:10.4271/10-06-01-0005
11. ISO 2631-1:1997. Mechanical Vibration and Shock-Evaluation of Human Exposure to Whole Body Vibration-Part 2. International Organization for Standardization; 1997.
12. ISO 8068. Mechanical Vibration Road Surface Profiles Reporting of Measured Data. International Organization for

Standardization; 1995.
13. Sun L. Optimum design of road-friendly vehicle suspension system subjected to rough pavement surfaces. Applied Mathematical Modelling. 2002; 25(5): 635-652. doi:10.1016/S0307-904X(01)00079-8
14. Sun X, Zhang J. Performance of earth-moving machinery cab with hydraulic mounts in low frequency. Journal of Vibration and Control. 2014; 20(5): 724-735. doi:10.1177/10775463124642
15. Ye S, Hou L, Zhang P, et al. Transfer path analysis and its application in low-frequency vibration reduction of steering wheel of a passenger vehicle. Applied Acoustics. 2020; 157: 107021. doi: 10.1016/j.apacoust.2019.107021
16. de Brett M, Butlin T, Nielsen OM. Analysis of nonlinear vibration transmission through a vehicle suspension damper at low audio frequencies. Journal of Sound and Vibration. 2023; 551: 117615. doi: 10.1016/j.jsv.2023.117615
17. Lakhdar Z, Chorfi SM, Belalia SA, et al. Free vibration and bending analysis of porous bi-directional FGM sandwich shell using a TSDT p-version finite element method. Acta Mechanica. 2024; 235: 3657-3686. doi: 10.1007/s00707-024-03909-y
18. Belabed Z, Abdelouahed T, Mohammed A, et al. On the elastic stability and free vibration responses of functionally graded porous beams resting on Winkler-Pasternak foundations via finite element computation. Geomechanics and Engineering. 2024; 36(2): 183-204. doi:10.12989/gae.2024.36.2.183
19. Bentrar H, Mohammed S, Belalia S, et al. Effect of porosity distribution on free vibration of functionally graded sandwich plate using the P-version of the finite element method. Structural Engineering and Mechanics. 2023; 88(6): 551-567. doi:10.12989/sem.2023.88.6.551
20. Mesbah A, Belabed Z, Amara K, et al. Formulation and evaluation a finite element model for free vibration and buckling behaviours of functionally graded porous (FGP) beams. Structural Engineering and Mechanics. 2023; 86(3): 291-309. doi: 10.12989/sem.2023.86.3.291
21. Dang V. Influence of Structural Parameters and Operating on Vietnam's Bus Ride Comfort. Hanoi University of Science and Technology, Vietnam; 1996.
22. Nguyen SD, Nguyen QH, Choi SB. A hybrid clustering based fuzzy structure for vibration control – Part 2: An application to semi-active vehicle seat-suspension system. Mechanical Systems and Signal Processing. 2015; 56-57: 288-301. doi: 10.1016/j.ymssp.2014.10.019
23. Zhu G, Du X, Liu W, et al. A novel method to solve the existed paradox of low-frequency vibration isolation and displacement attenuation in a nonlinear floating-slab on the wheel-rail loads. Mechanical Systems and Signal Processing. 2024; 208: 110985. doi: 10.1016/j.ymssp.2023.110985
24. Yang J, Nguyen V, Wang X, et al. Performance study of semi-active seat suspension added by quasi-zero stiffness structure under various vibratory roller models. Proc. IMechE, Part D: Journal of Automobile Engineering. 2023; 237(6): 1-15. doi:10.1177/ 0954407022114316

Mechanical Engineering Advances 2024, 2(1), 438.
https://doi.org/10.59400/mea.v2i1.438

Article

Fluid dynamics analysis for a production line

Nestor Antonio Flores Martínez[1,*], Valentín Guzmán Ramos[1], Ricardo Chapa García[2]

[1] Facultad de Ciencias Físico-Matemáticas, Universidad Autónoma de Nuevo León, San Nicolás de los Garza 66455, Nuevo León, Mexico
[2] Universidad Tecnológica General Mariano Escobedo, Escobedo 66050, Nuevo León, Mexico
*** Corresponding author:** Nestor Antonio Flores Martínez, janadioses@hotmail.com

CITATION

Martínez NAF, Ramos VG, García RC. Fluid dynamics analysis for a production line. Mechanical Engineering Advances. 2024; 2(1): 438.
https://doi.org/10.59400/mea.v2i1.438

ARTICLE INFO

Received: 20 November 2023
Accepted: 2 January 2024
Available online: 15 February 2024

Abstract: Magnetic filters are used on companies for mass flux and volume flux values that help to cover day-to-day production. This work begins by describing the problem of magnetic filter fractures as of industrial interest. A brief description of how magnetic filters must work on applications according to requirements on the process line. On the next section, it is possible to find the explanation of structural fractures and mistakes on the design or data sheet, which are usually not considered in guaranteed policy. Are mentioned more than one math modeling, taking the simplest to show the effective value of maximum pressure tolerated on magnetic filters differs from estimated for controlled conditions. Solutions shown in the article are a first approach to a future general model theory that could explain how applied science works in a factory where there is no time to stop production. This work relates the math model and some values to application, meaning both the project hypothesis modeling and factories requirements for their equipment. Results depict volume, velocity, density, and pipeline relation to the pressure increase over the values on the data sheet from quality department tests. Conclusions describe the connection of the math model analysis with real situations on the application or possible structural damage. And its relationship with the proper function of magnetic filters for the purpose of lifespan analysis on future works. This work is a proof that in a few weeks, companies can have a solution for their problems, letting them buy some time to avoid any future issues.

Keywords: magnetic filters; turbulence; mass flux; fluid dynamics; industry; production line; fluid pressure

1. Introduction

On every production line or quality assurance that requires constant flow on any section, there is a fluid (liquid, gas, or a mix of both) that could have ferromagnetic particles mixed with the product. Those particles could be harmful for the final customer for food production or processing. These metal particles can damage equipment and measuring instruments due to friction, eddy current generation, or a non-controlled pressure increment. For the cleaning of such materials, industries get magnetic filters installed as part of pipelines [1–4]. Filters use rare earth magnets on the inside of rods. Guarantee policy usually includes tables about pressure limits, temperature, and useful lifetime [5]. This data sometimes comes from experiments or factory tests asked for quality processes. Not all industries consider them for their process or quality control, due to the environmental conditions as pressure from an air injector (or water injector), as directors want something for every scenario possible.

Real environmental conditions [1,3,4,6,7] of magnetic filter usage seem not considered in experiments or theoretical studies. A lack of quality standards. Higher density, greater viscosity, noise (more than one kind) [8], and overheating are

conditions that make real systems work far beyond predictions [6,9–11]. Every time a fluid passes through the magnetic field, some physical effects occur; there is no control over the functioning [2,6]. Efficiency drops because of non-considered effects on the fluid [12] or magnetic dynamics.

Analyzing structure [1–4], thermal properties [6,7], side-effects [11], and phenomena [6,7,13] on manufacturing or cleansing processes as a research project is not possible for most factories. Numerical methods are limited to the precision and accuracy of math equations and are not considered for application. The so-called toy models are based on oversimplified, quick analysis of some physical phenomena. Even that kind of research can take months to years or decades to get a solution. That kind of investment (time and resources) is not an element for managers' protocols.

A brief math modeling should be studied as the process continues. Most dynamical systems include equations for virtual work and virtual energy resolutions [6]. Even with access to the process line, some conditions are not part of the analysis, like external environment conditions (air flux on the company, cleaning, shocks, external vibration, not controlled humidity, and heat sources). Rust, structural fracture, and vibration are elements that shorten the lifespan of equipment. Most of the predictive systems on quality assurance are modeled for a perfect environment that would not have irregularities, humidity, or changes in the working cycle.

Such filters are manufactured on several parts, having some magnetic rods on the inside (the amount depends on the factory and model). There are two kinds of alignment for the rods: 1) a circle near the metallic wall, and 2) a circle with a central rod. In both cases, the fluid collides against rods, generating a rotational system on two axes (up-down, side-to-side) for the fluids [13]. Other considerations could be part of the analysis for an approach: if there is some deposition of material or ferromagnetic particles on the lowest part of the vase.

2. Analysis of equipment operation

A magnetic filter has a constant incoming fluid [1–4] for different kinds of materials according to each factory. Ferromagnetic particles get attracted by the magnetic field of rods: viscous fluid gets inside, passes through magnets, and gets cleaned, retaining ferromagnetic contaminants, then it leaves the filter. There are several values of pressure on the filter [5]: max tolerated by the structure, expected pressure, and effective pressure. Turbulence, fluid rotational, torque, and force excess occur once the fluid passes [12]. On the process line, we find some complications: changes in pipeline diameter, acceleration of fluid for changes in direction, and open-closed valves.

Pressure can be defined as the effect of average collisions of molecules of a body (fluid or solid) against the container or internal collisions [6,8]. On real systems, turbulence means a constant increase of direction and acceleration, then pressure increases [5]. Molecules colliding with each other means an increase in temperature; this is another average measurement of the kinetic energy of molecules and their dynamics. Changing the heath can generate a volumetric expansion, with a pressure increase as a consequence.

All previous dynamics are related to fluid density, mass flux, and diameter of

pipeline. The technical data sheet comes with a table of pressure values expected from an extrapolation due to an experimental test on a controlled environmental system. Such tables are uncertain, as every factory has its own suppliers. Instead of calculating a table for each company, a complete math model can be developed.

Avoiding problems with measuring, the geometric structure is not analyzed with values. Instead, it can be described using proportions. From a list of products, the most bought have a four-inch radius. According to space and volume, the main characteristic is diameter variation. Using the percentage change. As greater the reduction in diameter, greater the pressure increase. As greater the change in pipeline, greater the turbulence factor.

There are two ways of analyzing. On one hand, net effective pressure is a characteristic that tells us how pressure by fluid collision has its max value inside the filter. On the other hand, changes in pressure can give information about the surplus for elements like the magnetic rods.

On factories, there is not enough time to measure the flow on pipelines, put pressure on every step, or stop processing [5]. Just some of the values can be measured, like pipeline diameter, initial flow velocity, and initial pressure.

3. Mathematical analysis

Some elements are not constant under the considerations of mechanical vibrations and torque direction. In this case, for fluid analysis [7,12], main characteristics are volumetric flux ($Q = Av\cos\theta = Av = \sqrt{H/sL}$) and mass flux ($\dot{m} = \rho VS$) for the dynamics. For quality department tests, the fluid is stablished under some controlled conditions with no vibrations, no turbulence, and underwater pressure (water injection on a short pipeline) [5]. Mechanical vibrations generate some noise on the fluid and a nonlinear turbulence as well as nonlinear rotational for the pressure [2,6,7,9,11–13]. As an approximation for the solution, are necessary both a toy model (no pressure gradient, no turbulence) and another with pressure as an experimental approach on the consideration of real data. The real phenomenon with no linearity was studied together.

For this brand, maximum pressure tolerance is estimated as 200 PSI (water pressure test for a short pipeline). Due to ISO and other normatives, filters can vary in their effectiveness by 10% [5]. Tolerance for the effective pressure on the processing, so the factories need to consider a greater value for the requirements of the clients. Max pressure is only information for the brand, not on the data sheet. Top values for every industry could not be the same.

Navier-Stokes [7] and Bernoulli equations for fluid mechanics describe a system with spatial and temporal dependence, with some factors like gravity and density, that most of the time are unknown. The first one can have a temporal variation, giving a real-time analysis. The second one represents how pressure, gravity, and geometry change force or its increase on the pipeline. The effective value for force, pressure, and flux comes from the nonlinear math analysis of fluid dynamics inside the filter once it collides with the magnetic rods.

Another not-known value is the original height (from the ground) for the pipeline, neither the final one if there is a variation. Is it possible to watch an industry's process

and measure those heights (as many other parameters)? Every factory has different infrastructure. Consider this height as constant on a long enough pipeline to avoid variation in calculus. The general view on the operation can be described as follows:

- Fluid travel through pipeline (no variations on structure) for an unknown extension.
- Fluid enters the filter. Turbulence and rotational dynamics are part of equations [13].
- After the cleaning, fluid flow out from filter with a different speed from the first step.

First and second are an issue for proper magnetic filter operation. Considering that once the fluid flow out, it keeps traveling through pipeline of a constant diameter. On the first equation, for Bernoulli on the non-compressible fluid transmission:

$$P_1 + \frac{1}{2}\rho v_1^2 + \rho g h_1 = P_2 + \frac{1}{2}\rho v_2^2 + \rho g h_2 \tag{1}$$

Height must be constant for at least one meter, for the math model to represent the real phenomenon according to experimental data. First pressure is the one from the pipeline before the filter, and the second pressure corresponds to the value inside the pipeline. Pressure as force per area unit, is useful to describe it with flux and time as parameters:

$$P = \frac{F}{S} = \frac{mv}{(Q/v)t} = \frac{mv^2}{Qt} = \frac{mQ^2}{A^2 t} \tag{2}$$

Such equation implies that increasing the mass flux can rise pressure (as a real application). Substitution of this factor as first pressure on pipeline on the Bernoulli equation, gives an identity for the second pressure (inside filter). According to density definition, if the volume changes, the density does too. For both considerations, pressure inside the filter:

$$P_2 = \frac{3}{2}\frac{\rho Q^2}{A^2} - \frac{1}{2}\rho v_2^2 \tag{3}$$

Once the fluid enters the filter, it expands due to the change in radius from the pipeline to the vase. Sometimes it can be compressed for a reduction in pipeline diameter. It depends on the factory.

Rotational and divergence are responsible for accelerations on all axes [7]. Physics, math, and technical concepts are not used in some factories, for them, there is no such thing as pressure gradient or variation. Those values cannot be evaluated. Initial velocity is determined by the pumps on the system or by free fall. The second speed (on the inside) is a function of the original velocity ($v_2 = v_2(v_1)$) and other parameters. There is a voracity, read as the natural frequency (or frequencies) of the fluid during the process:

$$\omega = \nabla \times v \tag{4}$$

Factories do not work under the same rules, protocol, or processes. Not all of them use top pressure as guidance [5,7]. Some consider other measures from several dynamics: mass flux, total inner volume, volume per minute, density, and some others. Some of them are necessary for the understanding of the proper use of the filters. For steady flow with no gravity [12], frequency can be approximated on the solution of a simple version of the Navier-Stokes equation [7]:

$$\frac{D\omega}{Dt} = \omega \cdot \nabla u + \nu \nabla^2 \omega \tag{5}$$

Represents the vorticity on the system. Four-dimension system, with spatial represented as a radius and angle. Is it possible to demonstrate that there is a trigonometric solution for a well-behaved case with a complex exponential time factor? To make math simple for non-specialized personnel, consider the definition of the vorticity through the rotational equation:

$$\omega = \omega_0 \frac{r_0^2}{r^2} = \frac{v_1}{r_0}\frac{r_0^2}{r^2} = \frac{Q}{A}\frac{r_0}{r^2} \tag{6}$$

Mass flux, PSI, flow velocity, and pressure are mandates on industries to understand the process; they don't mind if there are proper terms on the physical/engineering systems [5,12]. Using vorticity and the Bernoulli equation, the pressure of the filter vase can be estimated with parameters controlled as pipeline radius, vase radius, mass flux, and fluid density (if not known, can be approximated for water values):

$$P_2 = \frac{\rho Q^2}{2A^2}\left(\frac{3r_2^2 - r_0^2}{r_2^2}\right) \tag{7}$$

Forces and velocities (linear and angular) are implicit parameters of all equations depicted. Forces according to energies is an analysis for future works to stablish relations with the engines. Fluid elasticity allows to maintain the form during flowing. Also does the surface tension that breaks momentously once it enters the vase, generating a force (or a vacuum) that pulls fluid inside. That's the first acceleration. The other forces come from rotational due to the change in direction and change in velocity due to volume expansion [13]. Stablishing another Navier-Stokes variation [7] related to solid materials dynamics and structural analysis, substituting Equation (4) onto Equation (5), considering bulk modulus of fluid:

$$\frac{VB}{\Delta t}\nabla \cdot \vec{u} = m\omega \nabla \cdot (\nabla \times \vec{u})\Delta r \tag{8}$$

Partial differential equations, tensors, and stochastic equations are options for a solution on an approach to real applications [7]. The superposition principle requires a linear combination of solutions from different methods and conditions, even if they are nonlinear. The greater the number of solutions, the closer to reality. Tensorial equations are the middle point of complexity for solving, best for fluid dynamics. Considering pseudo-tensor using summation and dyadic for parameters: fluid volume and the mass flux using Equation (6). Solution as pressure that relates changes in group velocity (for perturbations), mass, and cross-sectional area proportion, making this an exchange of energy inside the pipeline. As well as proportion to bulk modulus and group velocity:

$$P \sim \frac{Br_2^2 V}{Qr_0}u_i = \frac{m}{A}\frac{\partial_i u_j \partial^2 \delta_{ij}}{u_i} \tag{9}$$

Even when Equation (9) still has derivatives, this is a tensor describing deformation of the fluid. Derivatives are not changing rate but still considered as an approach for application in a fast-working environment. Peak technology is not available in all factories, so there is no way to solve equations or evaluate functions constantly, neither using advanced programs. The best option for a real-time application is to use a simplified version, then evaluate the data.

Until now, the options for pressure function were: Equation (3) for the case of mass flux and velocity as main parameters; Equation (7) considering the change in velocity as a rate of pipeline diameter and filter size; and Equation (9) that analyzes pressure related to mechanical properties from the fluid conditions. Previous equations generate net pressure evaluation from mechanical and geometrical proportions as a system related to temperature, useful for applications:

$$(\Delta P)^2 = P_2^2 + P_3^2 = \left[\frac{\rho Q^2}{2A^2}\left(\frac{3r_2^2 - r_0^2}{r_2^2}\right)\right]^2 + \left[\frac{Br_2^2 V}{Qr_0}u_i\right]^2 \quad (10)$$

Group velocity is necessary to approach mass flux and volumetric flux. It is related to pipeline and fluid mechanical properties. Implicit parameters are out of reach of the article but still necessary for a better understanding: viscosity, elasticity, surface tension [7,10,12]. This velocity can be named effective flux:

$$u_i = \frac{Q}{AB}\frac{r_0}{r^2}\rho\partial_i u_j \partial^2 \delta_{ij} \quad (11)$$

Equation (10) is necessary for the close approach to application on industrial process lines. On future works, we must use a program to evaluate several parameters to stablish multiple tables for possible scenarios on the application. Thinking on the industries, the simple is to give them Equation (7) to evaluate easy-to-measure values and get some data for the quality process. Inquiring how close to optimal functionality are the magnetic filters.

4. Results and discussion

There is a nominal or expected pressure on magnetic filters [1–5]. Those are the values that a factory is expecting for a process line. Pressure can generate implosion of structure [11] if it is lower than optimal range. Above the maximum pressure value, it could cause structural fractures, leaks, or pipeline explosions. Calculating the effective pressure leads to understanding problems in the process. All the products studied have a tolerance for the maximum pressure supported. That can vary from 5% up to 15%. Depends on materials, operating conditions, manufacturing process, and environmental conditions.

That tolerance assures that fluid would exceed pressure on the filter without damage or explosion. If the production is not controlled, the pressure remains a problem, as it could exceed the maximum value. For factories that require the use of magnetic filters [1,3,4] the best option is to reduce mass flux, volume flux, or production per hour, meaning an incoming loss. The factories that produce the filters should build better equipment with greater maximum allowable pressure. Reporting a selected nominal pressure, stablishing two tolerances, one for the data sheet and the other (the highest one) for quality control.

The same for the lifespan and other characteristics. Due to any non-expected functioning conditions on the final customer installations.

Once the diameter changes at mass flowing from pipeline to filter, force, vorticity, and pressure increase can stay below the top pressure or under the tolerance rate. Could be greater than tolerance. Equations like Equation (7) calculate the excess of the pressure (PSI) on the filter due to the change of diameter and available space for the fluid.

Such a rate of variation seems negligible, but this is a percentage per cycle, not the entire process. The preferred use of the filters is to process the fluid and then stop using it some time for relaxing of the structure. After that, another cycle and go on. For the industry, the less time between cycles is the better. Process lines are designed for constant functioning, and even no shutdown is possible unless there is time for maintenance or repair.

Different mechanical properties for each fluid: density, viscosity, surface tension, elasticity, and heat capacity [7]. Applications should be a math development for every condition or a general model. Instead, a simplified version of the phenomenon can assure that tests on quality departments are not enough. Neither water nor air are common in the pipeline of industrial processes. If liquids are mixed with some solid particles or dust, the fluids have neither linear density nor pressure rating nor measuring.

Production of a week represents thousands of cycles of use per filter, then a greater than expected increase in pressure and heating for the cleaning. Thousands of cycles can mean near 1% of an increase. On that condition, the excess pressure on a constant use with no time for cooling would fracture the structure or reduce the magnetic intensity of rods.

For factories in Mexico, more production means more sales, more money (as a first thought). Maintenance is scheduled under data sheet recommendations and according to income. As mentioned before, the data sheet is calculated for ideal conditions. This kind of table depicted in the article should be on every factory that produces magnetic filters so they can offer their products according to customer needs.

Magnetic filter design and manufacturing can be improved through the study of a solution of tensorial mathematical model for general variables. Even considering volume increase at every time or compressions due to mass flux. There is an expansion generated by heat gradient, which is represented as percentual changes of some thermodynamic conditions (temperature, relative humidity, room atmospheric pressure) on quality departments.

Manufacturing implies the point between theory and application. Sometimes that theoretical modeling is only approximations, and simplified systems can be analyzed for the time allowed.

Tables 1 and **2** show how rates from pipeline to filter have a direct effect on pressure and volume change. As shown in equations, even if the diameter of the magnetic filter is greater than the pipeline, there should be a pressure change. Volume change (expansion and compression) on the pipe induces a pressure change, in most cases an increase. Even when there is more space (no significant pressure increasing), a heating process happens due to collisions on the new directions, i.e., the velocity gradient or rotational field [13–17].

International standards require that information should be reported to the public as values from the International Unit System (SI), but factories are still using the imperial system. Tolerances must be written as percentages due to the confusion from units on the imperial system to SI. These tables show information as PSI (pounds per square inch) and volume (meters) being the most mentioned on the data sheet, product catalog, and marketing.

Table 1. Values for excess of pressure per cycle on a process line for the smallest diameter.

Filter dimensions (inner radius) (1.5–2 IN/51 MM)						
Relative pipeline diameter						
%*	**Liquid fluid**		**Fibrous or doughy**		**Viscous or heavy**	
	Pressure (PSI)	**Volume (m^3)**	**Pressure (PSI)**	**Volume (m^3)**	**Pressure (PSI)**	**Volume (m^3)**
55	0.000943	0.001013	0.000646	0.009180	0.000267	0.003793
60	0.000793	0.001206	0.000543	0.007587	0.000224	0.003135
65	0.000675	0.001415	0.000463	0.006375	0.000191	0.002634
70	0.000582	0.001642	0.000399	0.005432	0.000165	0.002244
75	0.000507	0.001884	0.000347	0.004684	0.000144	0.001935
80	0.000446	0.002144	0.000305	0.004080	0.000126	0.001686
85	0.000395	0.002420	0.000271	0.003586	0.000111	0.001482
90	0.000352	0.002714	0.000241	0.003176	9.9721×10^{-5}	0.001312
95	0.000316	0.003023	0.000217	0.002833	8.95×10^{-5}	0.001171
100	0.000285	0.003350	0.000195	0.002543	8.0774×10^{-5}	0.001051

*The percentual variation from the pipeline before the magnetic filter to the opening.

Table 2. Values for excess of pressure per cycle on a process line for other model, considering simple fluids.

Filter dimensions (inner radius) (3.5–4 IN/102 MM)						
Relative pipeline diameter						
%**	**Liquid fluid**		**Fibrous or doughy**		**Viscous or heavy**	
	Pressure (PSI)	**Volume (m^3)**	**Pressure (PSI)**	**Volume (m^3)**	**Pressure (PSI)**	**Volume (m^3)**
55	0.018543	0.019920	0.012877	0.011432	0.009672	0.010390
60	0.015581	0.023706	0.010820	0.013833	0.008127	0.012365
65	0.013276	0.027822	0.009220	0.016463	0.006925	0.014512
70	0.011448	0.032267	0.007950	0.019321	0.005971	0.016831
75	0.009972	0.037041	0.006925	0.022408	0.005201	0.019321
80	0.008765	0.042145	0.006086	0.025723	0.004572	0.021983
85	0.007764	0.047577	0.005391	0.029267	0.00405	0.024816
90	0.006925	0.053339	0.004809	0.033040	0.003612	0.027822
95	0.006215	0.059431	0.004316	0.037041	0.003242	0.030999
100	0.005610	0.065851	0.003895	0.041271	0.002926	0.034348

**The percentual variation from the pipeline before the magnetic filter to the opening.

0.01039 m^3 equals 10,390 cm^3, which is a high value meaning a compression on the system. That compression raises the temperature and pressure. **Tables 1** and **2** show the increase of the volume once its diameter changes from the pipeline to the inside of the magnetic filter. Math correlation seems appropriate; as greater the inner radius of the filter, greater the volume expansion allowed. It is possible to analyze that as the inner radius of the filter increases, it can tolerate more compression on the volume of fluid. For a 55% diameter reduction, from the 1.5 inches (0.003793 m^3) change to the model to 3.5 inches (0.01039 m^3).

On the other hand, an increase in volume compression relates to pressure (PSI). Something beyond the objectives of this article can give a better understanding of

magnetic filter operation and lifespan. Indeed, the 3.5-inch radius model would generate more pressure on the inside, but the structure has more metal and better welding points. It is not just about the change in diameter; it is also important to know the structure, heat capacity, rod amount, and number of cycles per shift.

Solution to Equation (10) would consider even the operation in real time, considering flow velocity and mass flux [12]. Finally, Equation (8) has a direct relation with the medium of the fluid, like the metal, and the space of the magnetic filter. Solutions for the last one can include heat capacity, gravity action by free fall, and finally a more general perspective of the dynamics.

5. Conclusion

Space and time variables are explicit parameters. For a long enough time, in an enclosed environment with a constant flow, collisions randomly point to the same original direction (or proportional to it) as they enter the filter. This implies that velocity for some particles or volume sections turns negative [13], making a second gradient and rotational in the opposite direction from the original. This is a consideration for future solutions and applications. At the factories, this constant flux is part of everyday production, increasing the pressure to the point that filters start leaking even on the best quality for sealing.

Explicit thermal effect is not analyzed [14–17]. It just mentioned the action of the fluid on the pipeline for the pressure as the average effect of the collision of molecules.

The whole model and equations were solved in weeks due to a deadline at the factory. For an industry R&D department, a month or year of projects means money loss. An approximation is enough to improve the data sheet of equipment sold and installed. Lifespan can be predicted with high accuracy once the physical dynamics inside the filters can be determined and studied. This is an advantage for companies, no matter if they sell magnetic filters or use them. The efficiency of every filter is related to the proper pressure determination to consider the time it works on conditions beyond the designed purpose on optimal conditions.

Tables show that varying the space for fluid implies a pressure increase. Volume reduction or expansion generates heating on the material, the fluid, and noisy vibration causing fractures. The kind of fluid is important [10,12,14–17]; according to density and viscosity is the fluid dynamics studied; the closer the values to water ones, the better the analysis. Most equations are solved under water properties considerations.

Science researchers, engineers, industry workers, and society must collaborate to get better technology for making production more efficient. Once research gives information about lifespan production under real conditions, it is possible to prioritize preventive maintenance over corrective maintenance. As part of lifespan prediction, regulating the mass flux is necessary to avoid mistakes in the quality process or damage to the structural integrity of the factory.

The tables make it clear that using water for quality tests expresses wrong values or something that is not useful for all processes. Factories should produce new brands of magnetic filters with other materials that can resist heating, vibration, mechanical torsion, and other effects occurring during the cleaning process.

No deeper analysis of the cleaning, manufacturing, and food processing kind of

industry where this is applied.

6. List of symbols

A—cross section area of the pipeline, [m^2]

B—bulk modulus of fluids, [$\frac{\mathrm{N}}{\mathrm{m}^2}$]

$\frac{D\omega}{Dt}$—Laplacian plus time derivative of the vorticity expression, [$\frac{1}{\mathrm{t}^2}$]

$\partial_i u_j$—sum of all derivatives (tensorial form) for space and time variables of the group velocity of fluid motion, [$\frac{\mathrm{m}}{\mathrm{s}^2}, \frac{1}{\mathrm{s}}$]

$\partial^2 \delta_{ij}$—sum of all second derivatives (tensorial form) for space and time variables of the perturbation on the system, [$\frac{\mathrm{N}}{\mathrm{m}^2}$]

F—force due to molecules collisions on the fluid, [$\mathrm{N} = \frac{\mathrm{kgm}}{\mathrm{s}^2}$]

g—gravity, [$\frac{\mathrm{m}}{\mathrm{s}^2}$]

H—mean height of the fluid while traveling, [m]

h_1—height at the pipeline before the fluid enters the filter, [m]

h_2—height at the pipeline after the fluid goes out the filter, [m]

L—expected length of pipeline, [m]

$\dot{m} = \rho VS$—mass flux, [kgm^2]

m—mass of the fluid on the process during each cycle, [kg]

P—pressure at time *t*, [$\frac{\mathrm{N}}{\mathrm{m}^2}$]

ΔP—norm of the pressure on the filter, [$\frac{\mathrm{N}}{\mathrm{m}^2}$]

P_2—pressure on the filter due to rotational and gradient, [$\frac{\mathrm{N}}{\mathrm{m}^2}$]

P_3—pressure on the filter due to volume expansion, [$\frac{\mathrm{N}}{\mathrm{m}^2}$]

$Q = Av\cos\theta = Av = \sqrt{H/sL}$—mass flux, [$\frac{\mathrm{m}^3}{\mathrm{s}}$]

r_0—radius of the pipeline, [m]

r_2—radius of the magnetic filter, [m]

t—time, [s]

u_j—group velocity of the system inside the filter, [$\frac{\mathrm{m}}{\mathrm{s}}$]

v—velocity of the wave, [$\frac{\mathrm{m}}{\mathrm{s}}$]

v_1—velocity of the fluid on the pipeline, [$\frac{\mathrm{m}}{\mathrm{s}}$]

v_2—velocity of the fluid going out of the filter, [$\frac{\mathrm{m}}{\mathrm{s}}$]

ρ—density of the fluid, [$\frac{\mathrm{kg}}{\mathrm{m}^3}$]

$\omega = \nabla \times v$—vorticity inside the magnetic filter, [$\frac{1}{\mathrm{s}}$]

ω_0—natural frequency of the fluid inside the magnetic filter [$\frac{1}{\mathrm{s}}$]

V—volume of the fluid inside the magnetic filter, [m^3]

Author contributions: Conceptualization, NAFM and VGR; methodology, NAFM; validation, NAFM, VGR and RCG; formal analysis, NAFM; investigation, NAFM, VGR; resources, NAFM, VGR; data curation, NAFM, VGR and RCG; writing—

original draft preparation, NAFM; writing—review and editing, NAFM, RCG; visualization, NAFM; supervision, NAFM; project administration, NAFM, VGR, RCG. All authors have read and agreed to the published version of the manuscript.

Acknowledgments: Acknowledgement to Medrano Magnetics' personal for their help, access to information and constant communication during the research. Thank you for letting us know some design that they sell (structure, materials, manufacturing process) to use it on the math modeling.

Conflict of interest: The authors declare no conflict of interest.

References

1. Spevakova I, Ruditser L, Eroshenko V, et al. New Magnetic Filter for Chemical Industry. Magnetic and Electrical Separation. 1993; 5(1): 17-32. doi: 10.1155/1993/82842
2. Szatyłowicz E, Skoczko I. Magnetic Field Usage Supported Filtration Through Different Filter Materials. Water. 2019; 11(8): 1584. doi: 10.3390/w11081584
3. Flow Ezy Filters. Magnetic filtration: Sub-micron filtration for industrial fluids in precision applications. Available online: https://www.flowezyfilters.com/pdfs/magnetic/FlowEzyMagneticFiltration_master_catalog.pdf (accessed on 10 January 2024).
4. Eclipse Magnetics. Magnetic filtration systems: Sub-micron filtration for industrial fluids in precision machining & wash system applications. Available online: https://www.eclipsemagnetics.com/site/assets/files/23188/filt_-_etna_v14_english_2020.pdf (accessed on 10 January 2024).
5. Endoh S, Yamaguchi K. Characteristics of pressure drop across spongy nickel filter in magnetic separation process. Powder Technology. 1985; 45: 35-41.
6. Alton Everest F. The Master Handbook of Acoustics, 4th ed. McGraw Hill; 2000. pp. 50-64,110-115.
7. Aris R. Equations of Motion and Energy in Cartesian Coordinates. In: Vector, Tensors, and the Basic Equations of Fluid Mechanics. Dover Publications; 1989.
8. Tam AC. Applications of photoacoustic sensing techniques. Reviews of Modern Physics. 1986; 58(2): 381-431. doi: 10.1103/revmodphys.58.381
9. Bhattacharya K, Banerjee S, Mondal NK. Analytical computation of process noise matrix in Kalman filter for fitting curved tracks in magnetic field within dense, thick scatterers. The European Physical Journal C. 2016; 76(7). doi: 10.1140/epjc/s10052-016-4243-1
10. Morfey CL, Sorokin SV, Gabard G. The effects of viscosity on sound radiation near solid surfaces. Journal of Fluid Mechanics. 2011; 690: 441-460. doi: 10.1017/jfm.2011.449
11. Rosenhouse G. The Essence of Noise in Natura with Reference to Acoustics. WIT Transactions on Ecology and Environment; 2012. p. 160.
12. Rhoads BL. River Dynamics: Geomorphology to Support Management, 1st ed. Cambridge University Press; 2020. pp. 75-95.
13. Arteaga Marín J, Benavidez Muñoz H. Velocity profiles in a free-surface flow system with a hydraulic rotational vortex (Spanish). ESPAMCIENCIA. 2018; 9(1): 33-42.
14. Newland DE. Introduction to probability distributions and averages. In: An Introduction to Random Vibrations, Spectral and Wavelet Analysis, 3rd ed. Dover Publications; 2005.
15. Newland DE. Joint probability distributions, ensemble averages. In: An Introduction to Random Vibrations, Spectral and Wavelet Analysis, 3rd ed. Dover Publications; 2005.
16. Newland DE. Correlation. In: An Introduction to Random Vibrations, Spectral and Wavelet Analysis, 3rd ed. Dover Publications; 2005.
17. Newland DE. Spectral density. In: An Introduction to Random Vibrations, Spectral and Wavelet Analysis, 3rd ed. Dover Publications; 2005.

Mechanical Engineering Advances 2024, 2(1), 326.
https://doi.org/10.59400/mea.v2i1.326

Article

Thermochemistry of the dissolution of tetra-4-sulfophthalocyanine nickel in aqueous solutions KOH at 298.15 K

Olga Krutova*, Vladimir Maizlish, Michael Bazanov, Viktor Chernikov, Alexey Volkov, Pavel Krutov

Department of Analytical Chemistry, Ivanovo State University of Chemical Technology, 7 Sheremetevsky Ave., 153000 Ivanovo, Russia
*** Corresponding author:** Olga Krutova, kdvkonkpd@yandex.ru

CITATION

Krutova O, Maizlish V, Bazanov M, et al. Thermochemistry of the dissolution of tetra-4-sulfophthalocyanine nickel in aqueous solutions KOH at 298.15 K. Mechanical Engineering Advances. 2024; 2(1): 326. https://doi.org/10.59400/mea.v2i1.326

ARTICLE INFO

Received: 14 December 2023
Accepted: 1 February 2024
Available online: 4 March 2024

Abstract: We have obtained a nickel tetra-4-sulfophthalocyanine complex, soluble in water. The standard enthalpies of formation of a compound can be considered as the sum of the additive group contributions of fragments of these molecules. We assessed this value using a method based on group systematics with a Benson-type classification of fragments, taking into account the influence of the primary environment of the atoms. In order to obtain the value of the contribution of Ecompl(N)4-Ni, we used the bomb calorimetry method. The enthalpy of combustion of tetrakis (4-methoxyphenyl) porphine and its complex with nickel tetrakis (4-methoxyphenyl) porphine nickel were experimentally determined. Thermal effects of dissolution of crystalline nickel tetra-4-sulfophthalocyanine in aqueous solutions of various KOH concentrations (from 0.002 to 0.02 mol·L^{-1}) at 298.15 K were determined by the direct calorimetric method. The measurements were carried out in a calorimeter with an isothermal shell equipped with a reaction vessel with a volume of 60 cm^3, electric calibration at T = (293.15–308.15) ± 0.01 K and P = 100.5 ± 0.7 kPa, and automatic temperature registration. The standard enthalpy of formation of dissociation products of the tetra-4-sulfophthalocyanine complex with nickel in an aqueous solution has been calculated.

Keywords: thermodynamics; solutions; calorimeter; enthalpy; constant; phthalocyanines

Currently, studies of phthalocyanines (Pc) and their derivatives are intensively developing [1–5]. One of the directions of PC modification is the introduction of various substituents into the benzene rings of compounds. Currently, sulfophthalocyanines are used as dyes [6], effective catalysts for various redox reactions, models in the study of some biological processes [7], medicine, etc. [8–10]. There is no data in the literature on the enthalpies of dissolution of tetra-4-sulfophthalocyanines with nickel in aqueous solutions of alkalis. Despite the fact that this class of compounds is being studied very widely at present, it is known that the introduction of sulfo groups into the Pc molecule gives the compounds the ability to dissolve in aqueous solutions of alkalis. However, sulfophthalocyanines have been studied to a much lesser extent. We chose nickel as the complexing ion. Nickel ion is one of the important microelements for living organisms (bacteria, plants, animals, and humans). About biological the role of nickel (II) in an enzymatic catalyst (urease) more than 30 are known years.

In this work, the complexes of tetra-4-sulfophthalocyanine with nickel were chosen as the object of research (**Figure 1**).

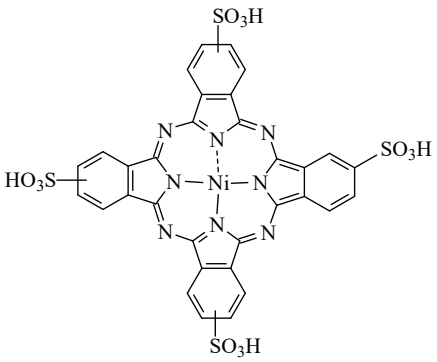

Figure 1. Tetra-4-sulfophthalocyanines nickel.

The aim of this work was to study standard enthalpies of the formation of complexes of tetra-4-sulfophthalocyanines with nickel and their dissociation products in aqueous solution by the thermal effects of dissolution of the preparations in water and in aqueous solutions of KOH at 298.15 K. We obtained data for calculating group contributions (E_{compl} $(N)_4$-Ni) to the enthalpy of formation of tetra-4-sulfophthalocyanines with nickel using an additive scheme for the first time. The combustion enthalpies of Tetrakis(4-methoxyphenyl)porphine (1) and tetrakis(4-methoxyphenyl)nickel porphine (2) were determined experimentally using bomb calorimetry. From these data, the contribution of (E_{compl} $(N)_4$-Ni) was isolated for the first time.

1. Experimental part

4-tetrasulfophthalocyanine with nickel was synthesized by the method of "urea fusion" [11]. The resulting melt was ground, dissolved in water, the solution was filtered, and the filtrate was evaporated. The substance was washed with concentrated hydrochloric acid to colorless filtrates and dried. The product was dissolved in water, the aqueous solution was passed through a column with KU-2-8 cationite, and then chromatographed using silica gel and molselect G-10 sequentially as an adsorbent, collecting the most colored zone. The resulting solution was evaporated, and the dry product was treated with organic solvents (methanol, acetone, and benzene) in a Soxlet apparatus. Dried under vacuum at 373–383 K. Output: 37%. ESP, λmax, nm (lgε) (DMSO): 665 (5.4), 610 (4.6), 336 (4.4), what corresponds to the literature data [11].

It is known that as a result of template synthesis, a mixture of randomizers is formed, the separation of which is a difficult task. In our case, the separation and isolation of individual randomers was not carried out.

The heat of dissolution of the investigated compound was determined experimentally in this work by the calorimetric method. The installation is described in detail in the work [12]. The operation of the installation was checked according to the calorimetric standard [13].

The heat of combustion was measured in a calorimeter of type B-08-MA with an isothermal shell, a stationary calorimetric bomb, and an improved measuring circuit, according to the method described earlier [14]. The temperature change in the calorimetric vessel was recorded using a platinum resistance thermometer included in the bridge circuit. The measured characteristic is the unbalance voltage of the bridge

(P-4053). The energy equivalent of the calorimeter, which was determined by burning K-1 benzoic acid, was 8348.5 ± 2.8 kJ/V. The initiation of the Gorenje reaction was carried out by discharging a capacitor onto a copper wire.

2. Results and discussion

It is advisable to use the Benson method to calculate the standard enthalpy of formation [15–17]. The calculation of the enthalpy of combustion and formation of the test compound was carried out according to the formula:

$$\Delta_{c(f)}H^0{}_{(cr)} = \sum_i^{\prod} A_i \Delta_{c(f)}\mathrm{H}_i^0, i = 1,2,3,\ldots.n \quad (1)$$

where $\Delta_{c(f)}H°_{(cr)}$ is the energy contribution to the enthalpy of combustion (formation) of a certain atomic group, A_i is the number of such atomic groups in the molecule, and n is the number of types of atomic groups in the molecule.

In the **Table 1**. the initial data for the calculation of $\Delta_fH^0{}_{cr.}$ ($C_{32}H_{16}$ $N_8O_{12}S_4Ni$) are presented.

Table 1. Numerical values of energy contributions to the values of the enthalpy of formation in accordance with the Benson classification.

№	Group	Number of groups (n)	$-\Delta_fH^0{}_{(cr.)i}$, kJ·mol^{-1}
1	$(C)_3$-CH	12	−19.9 ± 29.3
2	$(C)_3$-N	8	−102.0 ± 64.3
3	$(C)_4$-C	8	−9.4
4	$(C)_3$(S)-C	4	2.5
5	$(N)_3$(C)-C	8	−318.0
6	(C)-SO_3H	4	1495.4 ± 71.6
7	E_{compl} $(N)_4$-Ni	1	840.25 ± 14.32*

* experimentally determined in this paper.

In order to obtain the value of the contribution of Ecompl(N)4-Ni, we used the bomb calorimetry method. The enthalpy of combustion of tetrakis (4-methoxyphenyl) porphine and tetrakis (4-methoxyphenyl) nickel porphine was experimentally determined (**Figure 2**). The data are presented in **Tables 2** and **3**.

Table 2. Heat of combustion of tetrakis (4-methoxyphenyl) porphine.

№	m_{TMPP}, g	$\Delta T_{испр.}$, mkV	$\frac{m_{CO_2}{}^{exp.}}{m_{CO_2}{}^{calc.}}$	$q_{HNO_3} \cdot 10^{-3}$, kJ	$-\Delta_cU^B$, kJ·mol^{-1}
1	0.0487	193.9609	1.0001	5.66	24,248
2	0.0515	204.5898	-	6.75	24,236
3	0.0783	310.6317	1.0002	7.16	24,258
4	0.0846	335.3150	0.9998	8.34	24,232
5	0.0944	374.3164	-	9.26	24,246

$-\Delta_cU^B{}_{cp.}$ = 24,244 ± 13 kJ·mol^{-1}.

Table 3. Heat of combustion of tetrakis (4-methoxyphenyl) nickel porphine.

№	$m_{T_{(n\text{-MeOPh})PNi}}$, g	$\Delta T_{испр.}$, mkV	$\frac{m_{CO_2}{}^{exp.}}{m_{CO_2}{}^{calc.}}$	$q_{HNO_3} \cdot 10^2$, kJ	$-\Delta_c U^B$, kJ·mol^{-1}
1	0.03729	138.06	0.9989	3.12	24,233
2	0.05394	199.15	1.0003	4.05	24,229
3	0.05425	200.31	0.9998	4.06	24,231
4	0.05885	217.23	1.0001	4.42	24,238
5	0.06558	241.99	1.001	4.92	24,242

$-\Delta_c U^B_{cp.}$ = 24,246 ± 6 kJ·mol^{-1}.

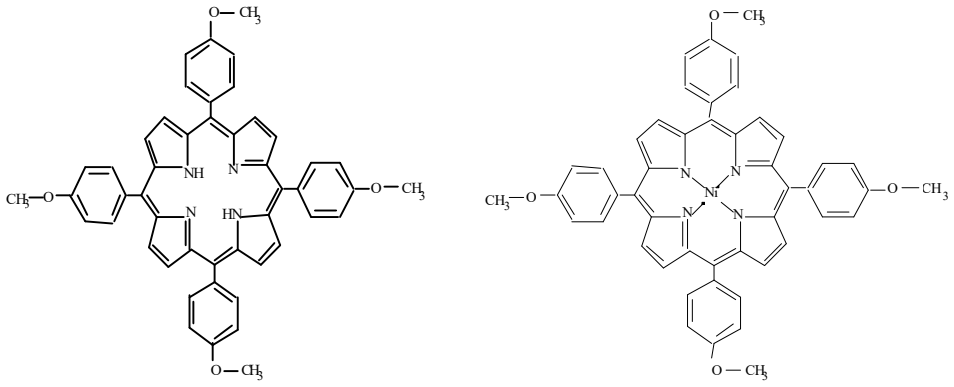

(a) **(b)**

Figure 2. (a) Tetrakis (4-methoxyphenyl) porphine; **(b)** tetrakis (4-methoxyphenyl) nickel porphine.

Compound (a) and (b) were obtained by Tarasov et al. [18].

Benzoic acid was used as an auxiliary substance for the difficult-to-burn compounds studied in this work. Therefore, when calculating the combustion energy, the correction for the heat of combustion of benzoic acid was taken into account.

The values of the combustion energy of the studied compounds are attributed to combustion reactions, which can be represented by the following schemes: for organic compounds:

$$C_m H_n N_p O_{q(cr.)} + \frac{(2m - q + n/2)}{2} O_{2(g)} = m\left(CO_{2(g)}\right) + n/2 H_2 O_{(sol.)} + p/2 N_{2(g)} \quad (2)$$

for complexes with metals:

$$C_m H_n N_p O_q Ni_{(cr.)} + \left[\frac{(2m - q + n/2)}{2} + 0.5\right] O_{2(g.)} = m\left(CO_{2(g.)}\right) + n/2 H_2 O_{(sol.)} + p/2 N_{2(g.)} \quad (3)$$

Nitrogen, which is part of the compound, is released in free form (N_2) as a result of the combustion reaction, and only a small part of it is found in the final products in the form of nitric acid, formed according to the equation:

$$1/2 N_{2(g.)} + 5/4 O_{2(g.)} + 1/2 H_2 O_{(sol.)} = HNO_{3(sol)} \quad (4)$$

The thermal effect of reaction (3) at 298.15K and dilution of 1:500 H_2O is 64.0 kJ·mol^{-1}. When calculating the value of $\Delta_c U^B$, a corresponding correction was introduced for the heat of formation of a nitric acid solution.

The combustion energy of the studied compounds was determined by the formula:

$$-\Delta_c U^B_{(cr.,298\,K)} = \frac{[W \cdot \Delta T_{cor.} - q_{b.} - q_{HNO_3} - Q_{.ac} \cdot m_{ac.}] \cdot M}{m} \quad (5)$$

where: W is the energy equivalent of a calorimeter, kJ/V; $\Delta T_{cor.}$—corrected temperature rise, V; $q_{b.}$—correction for the heat of combustion of copper wire, kJ; q_{HNO_3}—correction for the heat of formation of a solution of nitric acid, kJ; $Q_{.ac}$—the heat of combustion of benzoic acid, kJ/g; $m_{ac.}$—weight of the benzoic acid sample, g; M—molar mass of the compound under study, g/mol; m—mass of the sample under study, g.

The errors in determining the values of the combustion heats of porphyrins and their structural analogues were calculated similarly to the errors of the energy equivalent of a calorimeter with a confidence probability of 0.95.

The value of Δ_cU^B obtained as a result of the experiment refers to the isothermal combustion reaction of the studied compounds under real conditions of the process. To calculate the change in the internal energy of the combustion reaction of a substance under standard conditions, that is, when all the starting substances and combustion products are at a pressure of 1×10^5 Pa and a temperature of 298 K, the Washburn correction was determined, which took into account the thermal effects of the compression processes of the gas and liquid phases of the bomb, the dissolution of CO_2 and O_2 in the liquid phase of the bomb, and the evaporation of water into the gas phase.

The standard enthalpy of combustion (Δ_cH^0) of the studied compounds was calculated from the ratio:

$$\Delta_c H^0 = \Delta_c U^0 + \Delta nRT \quad (6)$$

where: Δn is the change in the number of moles of gas in the chemical equation for the combustion process of substances.

The standard enthalpy of formation (Δ_fH^0) of organic compounds was calculated by the formula:

For a complex with Ni, the calculation of Δ_fH^0 was carried out according to the equation:

$$\Delta_f H^0\left(\mathrm{C}_m H_n N_p O_q \mathrm{M}_{cr.,298\mathrm{K}}\right) = m\Delta_f H^0\left(CO_{2,g,298\mathrm{K}}\right) + n/2\Delta_f H^0\left(H_2O_{,sol,298\mathrm{K}}\right) + \Delta_f H^0\left(\mathrm{MO}_{cr.,298\mathrm{K}}\right) - \Delta_c H^0\left(\mathrm{C}_m H_n N_p O_q \mathrm{M}_{\mathrm{K.},298\mathrm{K}}\right) \quad (7)$$

The value of $\Delta_cU^B_{(cr,\ 298\ K)}$ refers to the combustion reaction of the TMPP under study:

$$C_{48}H_{38}N_4O_{4(cr)} + 55.5O_{2(g)} = 48CO_{2(g)} + 19H_2O + 2N_{2(g)} \quad (8)$$

According to experimental data, thermodynamic characteristics for tetrakis(4-methoxyphenyl) porphine are calculated using Equations (5), (7), and (8): Δ_cU^0 = –23,869 ± 13 kJ·mol^{-1}; Δ_cH^0 = –23,883 ± 13 kJ·mol^{-1}; Δ_fH^0 = –436.25 ± 13 kJ·mol^{-1}.

The value of $\Delta_cU^B_{(cr,298\ K)}$ is attributed to the combustion reaction T(n-MeOPh)Ni:

$$C_{48}H_{36}N_4O_4Ni_{(cr)} + 55.5O_{2(g)} = 48CO_2 + 18H_2O + NiO_{(cr)} + 2N_{2(g)} \quad (9)$$

During the combustion of the tablet of the drug under study, a precipitate of black NiO was formed; the amount of nickel and the composition of the precipitate were determined by atomic absorption analysis.

According to experimental data, the standard thermodynamic characteristics of the studied compound are calculated: Δ_cU^0 = −23,855 ± 6 kJ·mol^{-1}; Δ_cH^0 = −23,869 ± 6 kJ·mol^{-1}; Δ_fH^0 = −404 ± 6 kJ·mol^{-1}.

Based on the experimental values of the enthalpy of formation T(n-Me)Ph)P and its complex with Ni, the energy contribution associated with the complexation process is calculated. The calculation was carried out according to the formula:

$$E_{comp1.} = \Delta_f H^0_{(Me-EP-I)} - \Delta_f H^0_{(H_2EP-I)} \quad (10)$$

where: Δ_fH^0 is the standard enthalpy of formation of the tetrakis (4-methoxyphenyl) porphine nickel complex kJ·mol^{-1};

Δ_fH^0 is the standard enthalpy of formation of tetrakis (4-methoxyphenyl) porphine, kJ·mol^{-1} (**Table 4**). Thus, $E_{compl.}$ = −840.25 ± 14 kJ·mol^{-1}.

Table 4. Values of standard enthalpies of formation and complex formation energies T(n-ME)PH)P and NiT(n-MeOPh)P.

Compound	**Δ_fH^0, kJ·mol^{-1}**	**$E_{compl.}$, kJ·mol^{-1}**
T(n-MeOPh)P	436.25 ± 13	-
NiT(n-MeOPh)P	−404 ± 6	−840.25 ± 14.32

Based on the data obtained, we were able to calculate $\Delta_fH^0_{(cr.)}(C_{32}H_{16}N_8O_{12}S_4Ni)$= −3158.1 ± 101.6 kJ·mol^{-1}.

The process of dissolving in a KOH solution can be represented by the following scheme:

$$H_4L(cr.) + 4OH^-(sol., nH_2O) \rightarrow L^{4-}(sol., nH_2O) + 4H_2O \quad (11)$$

The experimental data of thermal effects of the dissolution of crystalline tetra-4-sulfophthalocyanine in aqueous solutions KOH at 298.15 K are presented in **Figure 3**. Experimental data are given in **Table 5**.

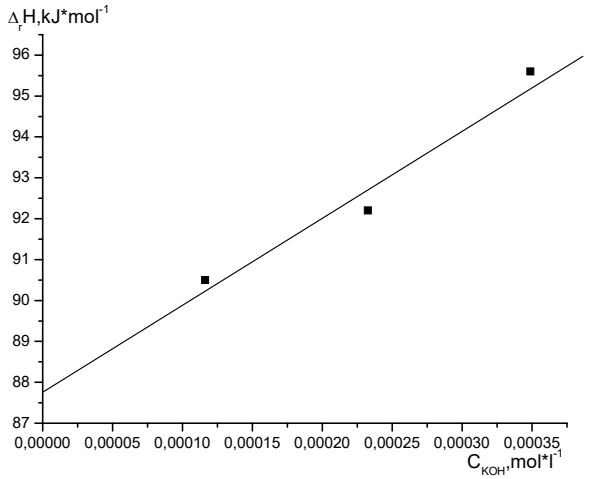

Figure 3. Graphical determination of the thermal effect of particle dissolution H_4L(cr.) in KOH solution with infinite dilution.

Table 5. Enthalpy of solubility of nickel tetra-4-sulfophthalocyanine in KOH solution at various concentrations and T = 298.15 K.

m 10^{-3}, g	**C_{KOH}. mol·L^{-1}**	**$-\Delta_{sol}H$ kJ·mol^{-1}**
0.0010		90.53 ± 0.36
0.0013	1.165×10^{-4}	90.65 ± 0.38
0.0012		90.48 ± 0.38
0.0020		92.25 ± 0.35
0.0021	2.326×10^{-4}	92.32 ± 0.36
0.0020		92.19 ± 0.38
0.0030		95.68 ± 0.35
0.0032	3.489×10^{-4}	95.66 ± 0.37
0.0030		95.65 ± 0.35

Practical testing of the Debye-Hückel theory has been the subject of numerous experimental works, including precision measurements of activity coefficients, heats of dilution, etc. A sufficiently rigorous test of the theory can be made, naturally, only in the region of extremely dilute solutions, where one can expect compliance with the limit law [19]. To process our data, we used the Equation (12) proposed by Vasiliev [19]:

$$\Delta_r H_i - \Delta Z^2 \psi(I) = \Delta_r H^\circ_i + bI, \quad (12)$$

where $\Delta_r H_i$ and $\Delta_r H^0_i$ are the thermal effects of process (11) at finite and zero values of the ionic strength.

Using the values of the standard enthalpies of formation of hydroxide ion $\Delta_f H^0$ (OH^-, sol., H_2O, std.s., 298.15 K) = −230.04 kJ·mol^{-1} and water (H_2O) in an aqueous solution $\Delta_f H^0$ (H_2O, lig, 298.15 K) = −285.83 kJ·mol^{-1}, recommended by Glushko [20], we calculated the standard enthalpy of formation of the deprotonated L^{4-} ion:

$$\begin{aligned}\Delta_f H^\circ(L^{4-}, sol., H_2O, std.s., 298.15\,K) \\ = \Delta_f H^\circ(H_4L, cr., 298.15K) + 4\Delta_f H^\circ(OH^-, sol., H_2O, std.s., 298.15K) + \Delta_r H^\circ_{(11)} \\ - 4\Delta_f H^\circ(H_2O, liq., 298.15K)\end{aligned} \quad (13)$$

The standard enthalpies of formation of HL^{3-}, H_2L^{2-}, H_3L^-, H_4L particles in an aqueous solution were calculated using the equations:

$$\begin{aligned}\Delta_f H^\circ(HL^{3-}, sol., H_2O, std., hyp., nedis., 298.15K) \\ = \Delta_f H^\circ(L^{4-}, sol., H_2O, std., 298.15K) - \Delta_{dis} H^\circ(HL^{3-}, 298.15K)\end{aligned} \quad (14)$$

$$\begin{aligned}\Delta_f H^\circ(H_2L^{2-}, sol., H_2O, std., hyp., nedis., 298.15K) \\ = \Delta_f H^\circ(HL^{3-}, sol, H_2O, std., 298.15K) - \Delta_{dis} H^\circ(H_2L^{2-}, 298.15K)\end{aligned} \quad (15)$$

$$\begin{aligned}\Delta_f H^\circ(H_3L^-, sol., H_2O, std., hyp., nedis., 298.15K) \\ = \Delta_f H^\circ(H_2L^{2-}, sol, H_2O, std., 298.15K) - \Delta_{dis} H^\circ(H_3L^-, 298.15K)\end{aligned} \quad (16)$$

$$\begin{aligned}\Delta_f H^\circ(H_4L, sol., H_2O, std., hyp., nedis., 298.15K) \\ = \Delta_f H^\circ(H_3L^-, sol, H_2O, std., 298.15K) - \Delta_{dis} H^\circ(H_4L, 298.15K)\end{aligned} \quad (17)$$

The values of $\Delta_{dis} H^\circ(H_4L, 298.15\,K)$, $\Delta_{dis} H^\circ(H_3L^-, 298.15\,K)$, $\Delta_{dis} H^\circ(H_2L^{2-}, 298.15\,K)$, $\Delta_{dis} H^\circ(HL^{3-}, 298.15\,K)$, were calculated by using the HEAT [21,22] computer program. The obtained values are presented in **Table 6**.

Table 6. Enthalpy of stepwise dissociation of Pc at a temperature of 298.15 K ($kJ \cdot mol^{-1}$).

Process	$\Delta_r H_{dis}$, (complex Ni)	pK_i
$H_4L \rightarrow H_3L^- + H^+$	52.3 ± 1.5	1.93 ± 0.35
$H_3L^- \rightarrow H_2L^{2-} + H^+$	98.6 ± 1.7	4.89 ± 0.35
$H_2L^{2-} \rightarrow HL^{3-} + H^+$	114.8 ± 1.9	9.31 ± 0.35
$HL^{3-} \rightarrow L^{4-} + H^+$	162.3 ± 1.6	12.32 ± 0.35

The thermodynamic characteristics of the dissolution of porphyrins obtained in our works [23,24] will allow us to evaluate the influence of the metal ion of the complexing agent, as well as the influence of the isimerism of the position of functional groups in the benzene ring. The values of the standard enthalpy of formation of Pc in an aqueous solution were obtained in this work for the first time. Variations in the central ion and the structure of substituents in the Pc molecule make it possible to change its thermodynamic properties, which is confirmed, in particular, by data on the heats of dissolution of copper tetra-3-carboxyphthalocyanine in a KOH solution ΔrH = −79.86 ± 0.4 kJ/mol and tetra-4-carboxyphthalocyanine copper ΔrH= −78.33 ± 0.4 kJ/mol [23], the replacement of the central metal ion with zinc makes this difference even more noticeable ΔrH(1) = −59.64 ± 0.4 kJ/mol [24]. The obtained values are presented in **Table 7**.

Table 7. Standard enthalpy of Pc formation and its dissociation products in Aqueous solution ($kJ \cdot mol^{-1}$).

Particles	Condition	$\Delta_f H°$(298.15 K), (complex Ni)
H_4L	cr.	−3158.1 ± 101.6
	sol., H_2O, st. s., hyp., nedis.	−3451.6 ± 101.6
H_3L^-	sol., H_2O, st. s., hyp., nedis	−3398.3 ± 101.6
H_2L^{2-}	sol., H_2O, st. s., hyp., nedis.	−3299.7 ± 101.6
HL^{3-}	sol., H_2O, st. s., hyp., nedis.	−3184.9 ± 101.6
L^{4-}	sol, H_2O, st. s.	−3022.6 ± 101.6

Author contributions: Writing—original draft, writing—review and editing, OK; conceptualization, VM and MB; formal analysis, VC; project administration, AV; investigation, PK. All authors have read and agreed to the published version of the manuscript.

Funding: The work was carried out at the Research Institute of Thermodynamics and Kinetics of Chemical Processes of the Ivanovo State University of Chemical Technology within the framework of the State Assignment (basic part), project № FZZW-2023-0008. The study was carried out using the resources of the Center for Shared Use of Scientific Equipment of the ISUCT (with the support of the Ministry of Science and Higher Education of Russia, grant N° (075-15-2021-671).

Conflict of interest: The authors declare no conflicts of interest.

References

1. Islam ZU, Tahir M, Syed WA, et al. Fabrication and Photovoltaic Properties of Organic Solar Cell Based on Zinc Phthalocyanine. Energies. 2020; 13(4): 962. doi: 10.3390/en13040962
2. Potlog T, Furtuna V, Rotaru C, et al. Material Properties of Zinc Phthalocyanine from FA Solution and Application in Organic Solar Cells. International Journal of Industrial Electronics and Electrical Engineering. 2018; 6(1): 40-46.
3. Znoyko SA, Elizavarova AP, Kustova TV, et al. Erbium and sandwich-type lutetium complexes containing fragments of tetraanthrachinoporphirazine and substituted phthalocyanines. Izvestiya vysshikh uchebnykh zavedenii khimiya khimicheskaya tekhnologiya. 2021; 64(4): 42-51. doi: 10.6060/ivkkt.20216404.6380
4. Koifman OI, Ageeva TA, Beletskaya IP, et al. Macroheterocyclic Compounds - a Key Building Block in New Functional Materials and Molecular Devices. Macroheterocycles. 2020; 13(4): 311-467. doi: 10.6060/mhc200814k
5. Shaposhnikov GP, Kulinich VP, Maizlish VE. Modified Phthalocyanines and Their Structural Analogues. Krasand; 2012. p. 480.
6. Maizlish VE, Shaposhnikov GP. Properties of Sulfoand Carboxy-Phthalocyanines. Advances in Porphyrin Chemistry. St. Petersburg State University; 2004. pp. 327-355.
7. Mironov AF. Lanthanide porphyrin complexes. Russian Chemical Reviews. 2013; 82(4): 333-351. doi: 10.1070/rc2013v082n04abeh004300
8. Petrov OA, Osipova GV, Maizlish VE, et al. Reactivity of Tetrakis(4-tert-butyl-5-phenylsulfanyl) phthalocyanine in Acid–Base Interactions with Organic Bases. Russian Journal of Organic Chemistry. 2021; 57(9): 1428-1434. doi: 10.1134/s1070428021090074
9. Shaposhnikov GP, Kulinich VP, Maizlish VE. Electrophysical, photoelectrophysical and optical properties of modified phthalocyanine. In: Golubchikova OA (editor). Advances in Porphyrin Chemistry. St. Petersburg: Research Institute of Chemistry of St. Petersburg State University; 1999. pp. 190-222.
10. Weber JH, Busch DH. Complexes Derived from Strong Field Ligands. XIX. Magnetic Properties of Transition Metal Derivatives of 4,4’,4",4”’-Tetrasulfophthalocyanine. Inorganic Chemistry. 1965; 4(4): 469-471. doi: 10.1021/ic50026a007
11. Maizlish VE, Mochalova NL, Snegireva FP, Borodkin VF. Synthesis and spectral properties of sulfonic acids of macroheterocyclic compounds and their metal complexes. Chemistry and Chemical Technology. 1986; 28(1): 3-20.
12. Lytkin AI, Chernikov VV, Krutova ON, Skvortsov IA. Standard enthalpies of formation of L-lysine and the products of its dissociation in aqueous solutions. Journal of Thermal Analysis and Calorimetry. 2017; 130: 457-460. doi: 10.1007/s10973-017-6134-6
13. Wadsö I, Goldberg RN. Standards in isothermal microcalorimetry (IUPAC Technical Report). Pure and Applied Chemistry. 2001; 73(10): 1625-1639.
14. Volkov AV, Platonocheva OY, Krutova ON, Degrees VB. The standard enthalpy of the formation of L-phenylalanine and its dissociation products in aqueous solution. Chemistry and Chemical Technology. 2009; 52(4): 7-10.
15. Tachistov AV, Ponomarev DA. Organic mass spectrometry (Russian). VVM; 2002. p. 346.
16. Kizin AN, Lebedev YA. Calculation of enthalpy of formation of poly-substituted aliphatic compounds in the solid phase. Docl. USSR Academy OF Sciences. 1982; 262(4): 914.
17. Krutova ON, Chernikov VV, Volkov AV, et al. Enthalpies of dissolution of 2,3-dicyano-5,7,7-trimethyl-6,7-dihydro-1h-1,4-diazepine in KOH aqueous solutions at 298.15 K. Journal of Molecular Liquids. 2020; 313: 113634. doi: 10.1016/j.molliq.2020.113634
18. Tarasov RP, Volkov AV, Bazanov MI, et al. The standard enthalpies of combustion and formation of crystalline cobalt tetrakis(4-metoxyphenyl) porphin complex. Russian Journal of Physical Chemistry A. 2009; 83(5): 868-869. doi: 10.1134/s003602440905032x
19. Vasiliev VP. Thermodynamic Properties of Electrolyte Solutions. Nauka; 1982.
20. Glushko VP (editor). Thermal Constants of Substances: A Handbook (Russian). VINITI; 1971.
21. Meshkov AN, Gamov GA. Mathematical Processing of Experimental Data Obtained with Ampoule and Titration Calorimeters Equipped with Different Types of Cells. Zhurnal fizicheskoy khimii. 2023; 97(2): 204-209. doi: 10.31857/s0044453723020164

22. Tyunina EYu, Krutova ON, Lytkin AI. Determination of the complexation parameters of L-asparagine with some biologically active pyridine derivatives in aqueous solutions from calorimetric results. Thermochimica Acta. 2020; 690: 178704. doi: 10.1016/j.tca.2020.178704
23. Krutova ON, Maizlish VE, Lytkin AI, et al. Thermochemistry of the Dissolution of Tetra-4-carboxymetallophthalocyanines in Aqueous Solutions of KOH at 298.15 K. Zhurnal fizicheskoy khimii. 2023; 97(2): 199-203. doi: 10.31857/s0044453723020115
24. Krutova ON, Maizlish VE, Chernikov VV, et al. Thermochemistry of the Dissolution of Tetra-4-(4'-carboxyphenyoxy)- and Tetra-4-(4'-carboxyphenylthio) phthalocyanines of Copper in Aqueous Solutions of KOH at 298.15 K. Zhurnal fizicheskoy khimii. 2023; 97(6): 794-799. doi: 10.31857/s0044453723060134

Mechanical Engineering Advances 2024, 2(1), 526.
https://doi.org/10.59400/mea.v2i1.526

Article

First and second law analysis of crack propagation in canvas painting

Mohammad Yaghoub Abdollahzadeh Jamalabadi

Faculty of Marine Engineering, Chabahar Maritime University, Chabahar 99717-56499, Iran; my.abdollahzadeh@cmu.ac.ir

CITATION

Jamalabadi MYA. First and second law analysis of crack propagation in canvas painting. 2024; 2(1): 526. https://doi.org/10.59400/mea.v2i1.526

ARTICLE INFO

Received: 30 January 2024
Accepted: 24 February 2024
Available online: 2 April 2024

Abstract: The knowledge of how the craquelures happen and their pattern on historical objects, especially paintings, is interested in the field of cultural heritage. Entropy generation and thermal analysis of crack growth are calculated numerically for the canvas painting. The painting is modeled as a three-layer composite with isotropic material properties. An in-house code is developed to model the plane strain elasto-static structural mechanics with hybrid-Trefftz finite element formulation. The results are benchmarked with numerical and analytical solutions. Entropy generation and temperature fields are simulated throughout stacking in mode I of a delamination process. The parameter study shows that the parameter of entropy has a great influence on the process of expectation of break proliferation in fast and low areas. It is likewise demonstrated that the use of the corruption entropy age hypothesis gives a technique for assessing the steady in the law of crack growth regarding the rate of entropy production.

Keywords: crack growth; thermodynamic analysis; entropy production; fatigue; thermal balance

1. Introduction

Almost all mechanical parts encountering cyclic stacking are helpless to building up a crack(s) that will in general proliferate and inevitably cause break disappointment, frequently abruptly and with calamitous outcomes. In this manner, it is nothing unexpected that numerous endeavors have been made to comprehend the idea of break development with cyclic stacking to prepare for crack. The stress intensity factor was created in 1957 by George R. Irwin, the man typically viewed as the first author of crack mechanics [1]. The stress intensity factor (K_I) for applied stress σ and crack length a is

$$K_I = \sigma F \sqrt{\pi a} \tag{1}$$

where F is a function of geometry.

When all is said and done, an article can be stacked toward any path comparative with a break. The sketch at the right shows a power vector in such an arbitrary direction. It is for the most part opposite to the split, yet additionally contains segments that produce in-plane and out-of-plane shear. At the point when this happens, the consistent activity is parceling the power into its basic segments. This procedure prompts the three stacking modes demonstrated as follows: Mode I loading happens frequently and produces the most harm. Along these lines, it normally gets the most consideration in examine, basic structure, disappointment investigation, and so forth. It is usually called the opening mode. Mode II corresponds to shearing of the broken face due to in-plane shear stresses. It presumably gets the second most consideration because the issue is as yet 2-D since all the activity is in-plane. Mode II stacking impacts split development heading in a manner that limits further Mode II stacking

while at the same time boosting Mode I. Mode III is the Tearing Mode for clear reasons. It is driven by out-of-plane shear pushing and doesn't appear to happen as regularly as the other two.

It is one of the most basic and valuable parameters in all of crack mechanics. The pressure force factor portrays the pressure state at a broken tip, is identified with the pace of split development, and is utilized to set up disappointment criteria because of crack. After two decades, Irwin indicated that Westergaard's outcome could be incredibly streamlined in the territory promptly encompassing the broken tip. He did as such by communicating in the district close to the broken tip. This disparity was utilized by Irwin to discover straightforward articulations (well, contrasted with the perplexing capacities). Irwin's improvement halted here, and this is for sure the characteristic spot to stop. In any case, in the years following Irwin's distribution, it got well known to incorporate. The two conditions have appeared in the diagram underneath. Unmistakably both are extremely close at the split-tip and wander as the good ways from the tip increments. The district of close understanding is roughly one may ask, why even waste time with Irwin's exact arrangement when Westergaard's accurate arrangement is accessible? There are a few reasons. In the first place, the estimated arrangement is, in fact, precise at the broken tip, and this is all that truly matters because the conditions at the split-tip direct (i) how quick the break develops, (ii) in which course it develops, and (iii) regardless of whether it flops disastrously. Second, the inexact arrangement uncovers the reliance of the pressure parts on totally depicting the seriousness of the pressure state at the split tip. Irwin perceived this and first utilized the term pressure force factor to depict the articulation.

Hypothetical models that use continuum harm mechanics essentially center around the debasement of the material before the commencement of a smaller scale break. Among outstanding commitments on the evaluation of split proliferation is the old-style work [1], which utilized the pressure power factor to land at an experimental connection for measuring the break spread. Other researchers adjusted the supposed by thinking about the impact of the average tension. Break conclusion impact was presented to portray the distinction between the consistency of the broken structure in airplane solid parts exposed to various loads.

When all is said and done, weakness in solids develops in 4 phases. The main phase includes the settlement or phase arrangement where separations happen and lasting groups are framed [2]. In the subsequent phase, separations to smaller-scale splits happen [3], and, in the third stage, the miniaturized scale breaks will, in general, arrange themselves opposite to the heading of greatest average pressure. A break is then shaped, and as it gets larger, it produces stress focused at the crack point. The last phase of exhaustion harm includes the spread of the large-scale break, described by striation and seashore mark development [4]. A large scale split quickly engenders until the last crack.

From the material's perspective, the development and proliferation of a visible crack are related to zone arrangement in front of the broken focus. The study right now is a wellspring of warmth age. The part of the plastic area changed over volume relies upon a few factors, for example, the yield strain, plastic strain, and strain solidifying. Research shows that 0.8 and 0.95 of work is changed to heat [5,6]. All the more, as of late, thermographic estimation systems have been utilized to increase further

knowledge into the idea of break spread. For instance, Breen et al. [7] utilized vitality scattering to break down weakness conduct in tempered steel. Other researchers [8] gave results to titanium combinations notwithstanding hardened steel. On the other hand

Chen et al. [9] revealed the spread of power esteems and demonstrated that versatile impact is prevailing in circumstances of average stress [10].

The thickness of cracks, direction (isotropy or anisotropy to grain), its change (smooth or jagged), square island frequency, and network (junctions, random) are the problems. For example, Italian has jagged cracks with a predominant direction, perpendicular to grain [11–14]. While Flemish straight cracks are parallel to grain with very small smooth islands. As well, Dutch cracks are jagged perpendicular to the longest side with medium-sized islands, but French curved cracks have no predominant direction with large smooth islands.

In old paintings, breaks of molecular bonds cause disorder in the network and cracks [15]. The painting film thickness plays a great role in crack propagation and the final geometry of each pattern [16]. As cracks of lateral area are powered by bulk stress energy, the critical force is related to film thickness and overcrack area to the power of 3/4 (see Equation (4) in Lazarus and Pauchard [16]). They found a relation between the average number of polygons and an analogy thermodynamic micro-canonical entropy. Another study [17] based on the porosity of the cement substrate on building coating shows that the change in entropy of the system causes greater defectiveness (probability of destruction). The entropic endurance level at the time crack initiation is measured in Karimian et al. [18]. They propose the entropy method to predict crack initiation. Entropy in crack networks in old paintings with saturation prospectus analyzed in other references [15,19–24]. Jamalabadi et al. [25–28] suggested that substrate material responsiveness to variations in relative humidity is the most dangerous condition for cracking a panel painting.

In the present paper, the plane strain electrostatic structural mechanics with hybrid-Trefftz finite element formulation [21] is used to model cracks in paintings. The numerical and analytical solutions are used to validate the used method. Entropy generation and temperature fields are simulated during cyclic loading on painting. The parameter study is used to study the entropy production rate.

2. Mathematical model

2.1. Second low analysis (entropy generation) in fatigue

Deformation is when an object changes its shape or size because of temperature or force. There are two types of energy release through fatigue: elastic deformation energy and plastic deformation energy. Elastic deformation is reversible, like when someone stretches a rubber band and it goes back to its original shape. Plastic deformation is irreversible, like when someone bends a steel rod and it stays bent even after letting it go. In the field of thermodynamics, fatigue damage is considered a process that cannot be reversed, and it releases energy, resulting in the creation of entropy. This irreversible process and the generation of entropy can be quantified by measuring the amount of thermal, strain, and acoustic energies that are dissipated when a system undergoes fatigue. The entropy generated through the fatigue process

at the absolute temperature of T, heat flux, and temperature gradients of ∇T calculated by summation of three components of plastic work, heat conduction, and thermodynamic work as

$$\dot{S_g} = \frac{W_p}{T} - \frac{\nabla T}{T^2} J_q - \frac{1}{T} A_k \dot{v_k} \tag{2}$$

where $A_k \dot{v_k}$ is the thermodynamic works consist of the state internal variables relating to irreversible deformation mechanisms (cyclic hardening/softening, phase transformation, surface traction, body force, and the so-called micro-forces, etc.), $\dot{v_k}$ and the conjugate thermodynamic forces associated with them A_k, and the plastic work W_p is defined as multiplication of stress tensor σ and plastic strain rate tensor $\dot{\varepsilon_p}$ as

$$W_p = \sigma : \dot{\varepsilon_p} \tag{3}$$

The amount of energy forces in a system depends on its current thermodynamic state, while the dissipative forces only depend on the rate at which the system changes. Interestingly, in a quasi-static setting where the system's velocities decrease, the dissipative forces should disappear. The second and third terms are neglected in common engineering problems, and Equation (1) is simplified. Total fatigue fracture entropy, can be evaluated by integrating non-negative entropy generation of Equation (2) from time $t = 0$ to $t = t_f$, when fracture occurs:

$$S_g = \int_0^{t_f} \frac{W_p}{T} dt \tag{4}$$

That value could be evaluated from a pure material such as stainless steel with properties given in **Table 1**. The rate of strain can be calculated from

$$\frac{\Delta \epsilon}{2} = \frac{\Delta \sigma}{2E} + \alpha \left(\frac{\Delta \sigma}{2k'} \right)^{1/n'} \tag{5}$$

Table 1. Mechanical properties of stainless steel 304.

parameter	value
E (GPa)	193
μ (GPa)	79
k (W/mK)	16.3
n'	0.26
k' (MPa)	1200
λ (m^2/s)	4.06×10^{-6}
t (mm)	1.85
σ_0 (MPa)	270

where the Stress Coefficient k', Strain Coefficient α and Exponential Coefficient constants n' for each layer are given in **Table 2**.

$$\Delta \sigma_{ij} = \Delta \sigma_0' \left(\frac{\Delta K_I^2}{\alpha \Delta \sigma_0'^2 I_{n'} r} \right)^{\frac{n'}{n'+1}} \tilde{\sigma}_{ij}(n', \theta) \tag{6}$$

Table 2. Mechanical properties of three layer painting on canvas.

parameter	value
E (MPa)	38.6
α (1/°C)	10^{-5}
v	0.3
t (mm)	0.152
glue	
E (GPa)	3.791
α (1/°C)	2.5×10^{-5}
v	0.3
t (mm)	0.0508
Naples yellow oil paint	
E (GPa)	0.327
α (1/°C)	5.2×10^{-5}
v	0.3
t (mm)	0.152

Finally, the term needed for Equation (4) for the dissipated energy can be determined using the following equation

$$W_p = f\left(\frac{1-n^{'}}{1+n^{'}}\right)\sigma_{eq}\varepsilon_{eq}^{p} \tag{7}$$

For plane stress the angle θ dependency of stress factor variation ΔK_I comes form

$$\omega(\theta) = \frac{1}{16\pi}\frac{\Delta K_I^2}{\sigma_0^{'2}}\left(1+\frac{3}{2}sin^2\theta + cos\theta\right) \tag{8}$$

and plane strain the angle dependency of stress factor comes form

$$\omega(\theta) = \frac{1}{16\pi}\frac{\Delta K_I^2}{\sigma_0^{'2}}\left((1-2v)^2(1+cos\theta) + \frac{3}{2}sin^2\theta\right) \tag{9}$$

the cyclic BC is used. Since for horizontal line plane stress is

$$\omega_0 = \frac{1}{8\pi}\frac{\Delta K_I^2}{\sigma_0^{'2}} \tag{10}$$

and plane strain is

$$\omega_0 = \frac{1}{8\pi}\frac{\Delta K_I^2}{\sigma_0^{'2}}(1-2v)^2 \tag{11}$$

2.2. First low analysis (thermal balance) in fatigue

Temperature field near crack zone is

$$\frac{\rho C}{k}\frac{\partial T}{\partial t} = \nabla^2 T + \frac{q}{k} \tag{12}$$

where q is the heat generation rate comes from plastic form in Equation (7) and in Cartesian coordinates the Laplacian operator is:

$$\nabla^2 = \frac{\partial^2}{\partial x^2} + \frac{\partial^2}{\partial y^2} \tag{13}$$

The dissipated energy from the crack tip in the plastic zone as a function of cycle number is

$$\frac{dw_p}{dN} = At\frac{(\Delta K_I)^4}{\mu\sigma_0^2} \tag{14}$$

where t is the thickness and A is constant

2.3. Trefftz triangular finite element for linear elasticity

For a dimensional static linear elasticity problem defined in the domain Ω and boundaries (displacement boundaries Γ_u and traction boundaries Γ_t) presented in **Figure 1**, the governing equation is given by:

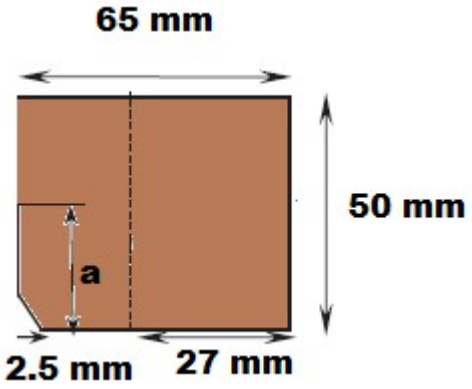

Figure 1. The experimental setup.

$$\rho\ddot{u} = \nabla \cdot \sigma + f \tag{15}$$

with the following boundary conditions presented in Figure\ref {FIG:3}:

$$u = \overline{u}\ on\ \Gamma_u \tag{16}$$

And

$$\sigma \cdot \boldsymbol{n} = \bar{\boldsymbol{t}}\ on\ \Gamma_t \tag{17}$$

The discrete equations for this problem formulated from Galerkin weak form of the governing Equation (15) is given by:

$$\int_{\Omega} (\nabla u)^T D(\nabla \delta u) d\Omega - \int_{\Omega} (\delta u)^T b d\Omega - \int_{\Gamma_t} (\delta u)^T \bar{\boldsymbol{t}} d\Gamma = \mathbf{0} \tag{18}$$

where u and δu are the trial and the test functions, respectively, and is the material constitutive matrix. The FEM uses the same trial and test functions. The finite element expansion of the governing equation, which is the series of the homogeneous solution, is given by:

$$u(x) = \sum_i N_i(x) c_i \tag{19}$$

Since the displacement matrix can be approximated by shape functions $N_i(x)$ with nodal degrees of freedom c_i which leads to the discretized algebraic system of equations:

$$M\ddot{u} + Ku = F \tag{20}$$

In Equation (20), M denotes the elastic inertia matrix, K denotes the elastic rigidity matrix, F denotes the external body force matrix, and u is the displacement

matrix, which they calculated in detail by

$$M = \int_{\Omega} N^T DN d\Omega \tag{21}$$

for the elastic inertia matrix and elastic rigidity matrix

$$K = \int_{\Omega} B^T DB d\Omega \tag{22}$$

The stiffness matrix is computed over each element and assembled to the global matrix. The size of the stiffness matrix depends on the number of nodes in an element. and external body force matrix

$$\boldsymbol{f} = \int_{\Omega} N^T b d\Omega + \int_{\Gamma_t} N^T \bar{\boldsymbol{t}} d\Gamma \tag{23}$$

3. Results

The thermal field spiral bearing is evaluated within the Fourier arrangement with four introductory expansions. The schematic is shown in **Figure 1**. This figure illustrates the setup used for conducting the experiment. It may show the equipment, instruments, or apparatus used in the study. Convergence is presented in **Table 3**. The method of three reference stress intensity factors leads to weight functions. Table 1 shows the mechanical properties of stainless steel 304. The loading cycle is 20 Hz. Material SS 304 is used for validation, as shown in **Figure 2**. This figure presents the comparison between the growth rate of a crack and the amount of entropy generated using experimental data. It helps validate the relationship between crack growth and entropy generation. In **Figure 2**, the spread appropriation of entropy generation around crack tip and crack speed is presented. **Figure 2** shows the break proliferation velocity taken from **Table 1**.

Table 3. Grid study.

Mesh number	Relative Error
783	0.02
4325	0.007
48210	0.003
81034	0.0005
128301	0

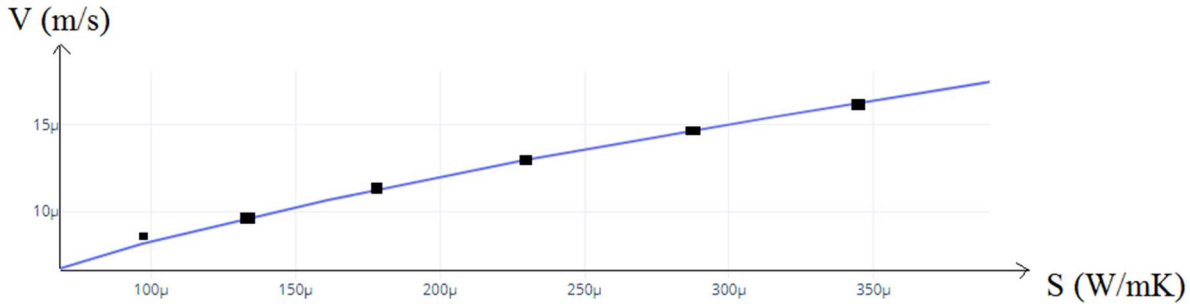

Figure 2. Validation of growth rate of crack versus entropy generation with experimental data.

As shown in **Figure 2**, the velocity of crack propagation increased with an increase in entropy generation around the crack tip.

Schematics of three-layer painting on canvas are presented in **Figure 3**. Note that the decision of the estimation of Fm is with the end goal that the outer pressure applied by the tip, Fm/S (being the anticipated surface of the tip on the film), is near the fine weight applied by the air/dissolvable meniscus at the dissipation surface of the layer. This figure provides a visual representation or diagram of the process or structure involved in a three-layer painting technique on canvas. It may show the layers and their arrangement.

Figure 3. Schematics of three layers painting on canvas.

In **Figure 4**, the distribution of shear stress and normal stress in painting layers are presented. This figure displays the distribution or magnitude of stress within a three-layer painting on canvas. It helps visualize the impact of the layers on the stress distribution. **Figure 4**. Warmth age of roundabout area split through the range of crack tip. **Figure 4** shows the engendering speed as an element of warmth age. The chart shows the consequences of the four tests. In ordinary exhaustion split engendering, the spread is examined in a moderately that conceivable to plan as indicated by the pressure power factor. Results displayed right now stream as a decent marker at low spread rates.

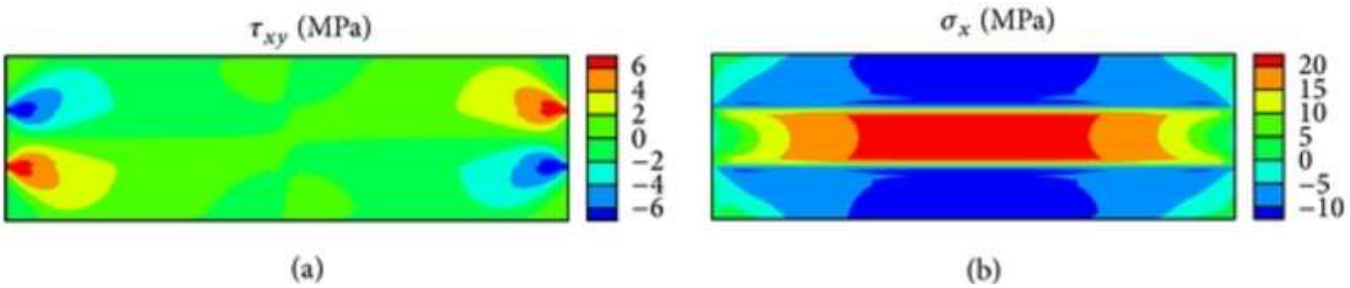

Figure 4. Stress in three layers painting on canvas.

In **Figure 5**, the thermal field in painting layers is presented. This figure depicts the thermal field or temperature distribution within a three-layer painting on canvas. It shows how heat is distributed across the layers and can provide insights into the painting process. To show the upside of utilizing entropy age in break spread examination, **Figure 5** delineates the examination between proliferation within the component of force stream. As appeared in **Figure 6**, the pressure power can't anticipate the speed; however, the entropy age approach yields reliable outcomes in

every one of the areas. It is viewed as a quick proliferation.

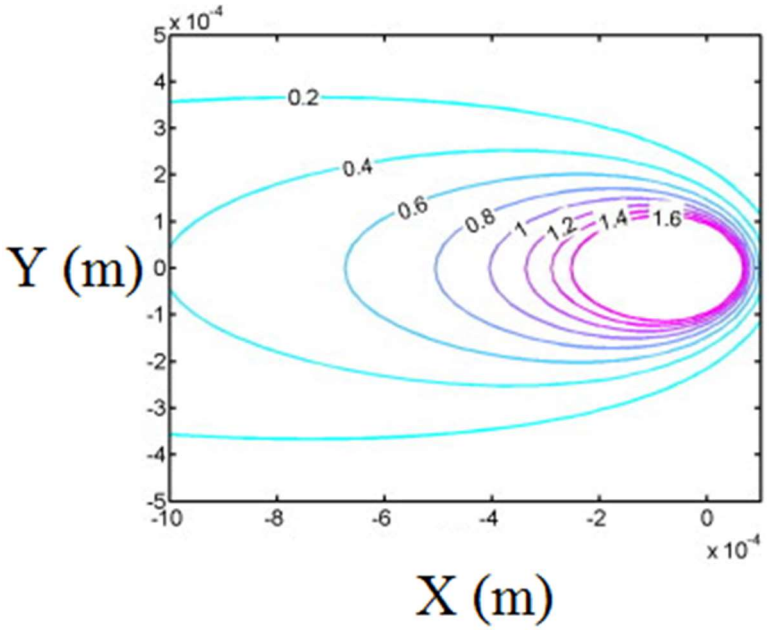

Figure 5. Increase of temperature (K) in three layers painting on canvas.

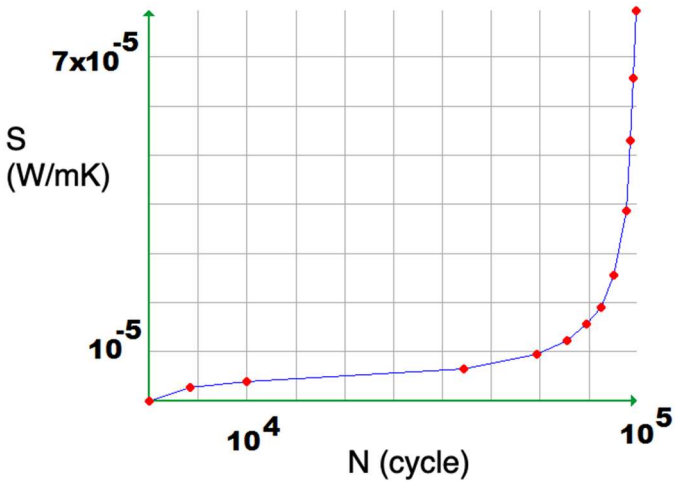

Figure 6. Entropy production versus cycle.

Entropy creation (or production) is the measure of entropy that is delivered in any irreversible procedures, for example, warmth and mass exchange forms, including the movement of bodies, heat trade, liquid stream, substances growing or blending, anaplastic distortion of solids, and any irreversible thermodynamic cycle. Entropy production versus cycle is presented in **Figure 6**. This figure plots the relationship between entropy production and the number of cycles or repetitions in a process. It helps analyze the change in entropy with each cycle.

Paris-Erdogan law (equation for rate of fatigue crack growth) is formulated by stress intensity factor and loading cycle. Based on crack growth versus entropy generation, the crack length can be predicted. Crack length rate versus entropy is presented in **Figure 7**. Split proliferation happens when the vitality stream from the pressure strain field to the break edge locale is adequate for supporting the procedures prompting mixtures of miniaturized scale partitions with the principle split. This figure

illustrates the relationship between the rate of crack lengthening and the amount of entropy generated. It helps understand how crack growth is related to entropy in the system. The investigation of the vitality stream to the procedure district is somewhat confounded in the general case.

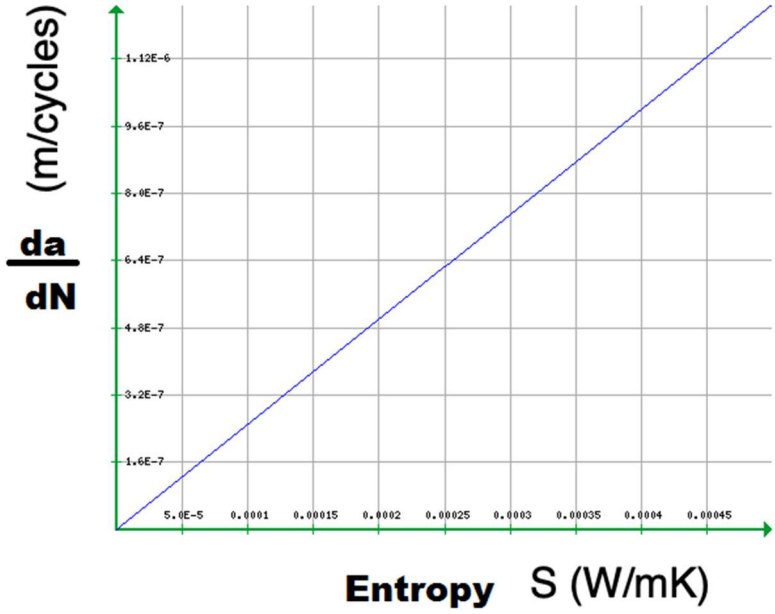

Figure 7. Crack length rate versus entropy.

4. Conclusion

The knowledge of how the craquelure happens and their pattern on historical objects, especially paintings, is interested in the field of cultural heritage. Entropy generation and thermal analysis were calculated numerically for the canvas painting. The painting is modeled as a three-layer composite with isotropic material properties. A house code is developed to model the plane strain elastostatic structural mechanics with hybrid-Trefftz finite element formulation. The results are benchmarked with numerical and analytical solutions. The main results are:

1) In mode, entropy generation and temperature field are simulated stacking of a delamination process.
2) The entropy generation parameter was significant in the expectation of break proliferation growth in fast areas.
3) It is likewise demonstrated that the use of the corruption entropy age hypothesis gives a technique for assessing the steady in Paris law regarding entropy production rate.

Conflict of interest: The author declares no conflict of interest.

References

1. Bueckner HF. Novel principle for the computation of stress intensity factors. Zeitschrift fuer Angewandte Mathematik & Mechanik. 1970; 50: 129-146.
2. Rice J. Some remarks on elastic crack-tip stress field. International Journal of Solids and Structures. 1972; 8: 751-758. doi: 10.1016/0020-7683(72)90040-6

3. Baraff D, Witkin A. Large steps in cloth simulation. In: Proceedings of the 25th Annual Conference on Computer Graphics and Interactive Techniques—SIGGRAPH'98; 18-24 July 1998; Orlando, USA. doi: 10.1145/280814.280821
4. Berger GA, Russell WH. Deterioration of Surfaces Exposed to Environmental Changes. Journal of the American Institute for Conservation. 1990; 29(1): 45-76. doi: 10.1179/019713690806046145
5. Blinn JF. Simulation of wrinkled surfaces. In: Proceedings of the 5th Annual Conference on Computer Graphics and Interactive Techniques; 23-25 August 1978; Atlanta, Georgia, USA. doi: 10.1145/800248.507101
6. Blinn JF, Newell ME. Texture and reflection in computer generated images. Communications of the ACM. 1976; 19(10): 542-547. doi: 10.1145/360349.360353
7. Breen DE, House DH, Wozny MJ. Predicting the drape of woven cloth using interacting particles. In: Proceedings of the 21st Annual Conference on Computer Graphics and Interactive Techniques—SIGGRAPH'94; 24-29 July 1994; Orlando, Florida, USA. doi: 10.1145/192161.192259
8. Carignan M, Yang Y, Thalmann NM, et al. Dressing animated synthetic actors with complex deformable clothes. ACM SIGGRAPH Computer Graphics. 1992; 26(2): 99-104. doi: 10.1145/142920.134017
9. Chen Y, Lin S, Hua Z, et al. Realistic rendering and animation of knitwear. IEEE Transactions on Visualization and Computer Graphics. 2003; 9(1): 43-55. doi: 10.1109/tvcg.2003.1175096
10. Cook RL. Shade trees. In: Proceedings of the 11th Annual Conference on Computer Graphics and Interactive Techniques; 23-27 July 1984; Minneapolis, Minnesota, USA. doi: 10.1145/800031.808602
11. Cook RL, Carpenter L, Catmull E. The Reyes image rendering architecture. In: Proceedings of the 14th Annual Conference on Computer Graphics and Interactive Techniques; 27-31 July 1987; Anaheim, California, USA. doi: 10.1145/37401.37414
12. Corel. Painter® Essentials 7 Quick Start Guide. Available online: https://product.corel.com/help/Painter-Essentials/540223061/Main/EN/Quick-Start-Guide/Painter-Essentials-Quick-Start-Guide.pdf (accessed on 12 January 2024).
13. Daubert K, Seidel HP. Hardware-Based Volumetric Knit-Wear. Computer Graphics Forum. 2002; 21(3): 575-583. doi: 10.1111/1467-8659.t01-1-00708
14. Daubert K, Lensch HPA, Heidrich W, Seidel H-P. Efficient cloth modeling and rendering. In: Proceedings of the 12th Eurographics Workshop on Rendering Techniques; 25-27 July 2001; London, UK.
15. Flores JC. Entropy Signature for Crack Networks in Old Paintings: Saturation Prospectus. Entropy. 2018; 20(10): 772. doi: 10.3390/e20100772
16. Lazarus V, Pauchard L. From craquelures to spiral crack patterns: influence of layer thickness on the crack patterns induced by desiccation. Soft Matter. 2011; 7(6): 2552. doi: 10.1039/c0sm00900h
17. Loganina V, Fediuk R. Thermodynamic Approach to Assessing the Curing of Protective and Decorative Coatings of Exterior Walls of Buildings. Materials Science Forum. 2019; 974: 3-8. doi: 10.4028/www.scientific.net/msf.974.3
18. Karimian SF, Bruck HA, Modarres M. Thermodynamic entropy to detect fatigue crack initiation using digital image correlation, and effect of overload spectrums. International Journal of Fatigue. 2019; 129: 105256. doi: 10.1016/j.ijfatigue.2019.105256
19. Flores JC, Palma-Chilla L. Entropy behavior for isolated systems containing bounded and unbounded states: latent heat at the inflection point. Journal of Physics Communications. 2020; 4(3): 035002. doi: 10.1088/2399-6528/ab78df
20. Agarwal N, Farris RJ. Thermodynamics of deformation of latex blend coatings and its implications for tailoring their properties. Journal of Coatings Technology. 1999; 71(9): 61-72. doi: 10.1007/bf02698385
21. Hirshikesh, Natarajan S, Annabattula RK, et al. Trefftz polygonal finite element for linear elasticity: convergence, accuracy, and properties. Asia Pacific Journal on Computational Engineering. 2017; 4(1). doi: 10.1186/s40540-017-0020-3
22. Ostoja-Starzewski M. Crack patterns in plates with randomly placed hole: A maximum entropy approach. Mechanics Research Communications. 2001; 28: 193-198. doi: 10.1016/S0093-6413(01)00162-8
23. Hajshirmohammadi B, Khonsari MM. Thermographic evaluation of metal crack propagation during cyclic loading. Theoretical and Applied Fracture Mechanics. 2020; 105: 102385. doi: 10.1016/j.tafmec.2019.102385
24. Hajshirmohammadi B, Khonsari MM. On the entropy of fatigue crack propagation. International Journal of Fatigue. 2020; 133: 105413. doi: 10.1016/j.ijfatigue.2019.105413
25. Abdollahzadeh Jamalabadi MY. Optimal rectangular crack pattern based on constructal, fracture saturation, and energy minimization theories for painting on wood. Chaos, Solitons & Fractals. 2022; 160: 112242. doi: 10.1016/j.chaos.2022.112242
26. Abdollahzadeh Jamalabadi MY. The Use of Artificial Intelligence for Image Processing of Crack Patterns in Panel Painting.

Sumerianz Journal of Scientific Research. 2022; 51: 1-12. doi: 10.47752/sjsr.51.1.12

27. Mohammad Yaghoub AJ. Paintings crack initiation time caused by microclimate. Annals of Mathematics and Physics. 2021; 4(1): 92-101. doi: 10.17352/amp.000028
28. Abdollahzadeh Jamalabadi MY, Zabari N, Bratasz Ł. Three-dimensional numerical and experimental study of fracture saturation in panel paintings. Wood Science and Technology. 2021; 55(6): 1555-1576. doi: 10.1007/s00226-021-01328-z

Mechanical Engineering Advances 2024, 2(1), 111.
https://doi.org/10.59400/mea.v2i1.111

Review

A review on Co_3O_4 nanostructures as the electrodes of supercapacitors

Samatha Kelathaya, Raghavendra Sagar*

Department of Physics, Mangalore Institute of Technology and Engineering (MITE), Affiliated to Visvesvaraya Technological University (VTU), Karnataka 574225, India
*** Corresponding author:** Raghavendra Sagar, raghav_sagar@rediffmail.com

CITATION

Kelathaya S, Sagar R. A review on Co3O4 nanostructures as the electrodes of supercapacitors. Mechanical Engineering Advances. 2024; 2(1): 111. https://doi.org/10.59400/mea.v2i1.111

ARTICLE INFO

Received: 12 July 2023
Accepted: 13 December 2024
Available online: 4 January 2024

Abstract: Usage of supercapacitors in energy storage applications has now become a new trend due to their auspicious features. The introduction of pseudocapacitance has increased its weightage to be used in a greater number of practical applications. Electrodes are the major constituents of a supercapacitor, based on which the electrochemical performance of the supercapacitor is decided. Among the varieties of electrode materials available, transition metal oxides are the most suitable ones to fulfill the required criteria. Due to the occurrence of faradic redox reactions on the surface of electrodes, the selection of efficient and favorable electrode material plays a major role. Co_3O_4 (cobalt (III) oxide) is one of the most desirable electrode materials due to its various peculiar features. This paper reviews briefly several factors of Co_3O_4 as electrode material in supercapacitor applications. It includes comparative discussions towards different synthesize methodologies and the influence of its dimensional morphology on the electrochemical outputs like specific capacitance, energy density, and power density.

Keywords: cobalt oxide; morphological structure; specific capacitance; energy density; power density

1. Introduction

Supercapacitors are one of the topmost investigated materials, which expand their applications further day by day. It has overwhelmed the constraints of fuel cells and the batteries for energy storage practices in assorted fields, including regenerative breaks, submarines, backup power systems, and voltage stabilizers. Also, due to the high efficiency of supercapacitors and high oil cost, supercapacitors rapidly engage all automobile applications[1]. Multiple investigations are under progress to enhance the competence and explore its usage in more and more fields with major practical applications. The electrolyte, separator, and electrodes are the major components of the supercapacitor, which highly impacts the electrochemical output. Here in this paper, a brief review of several factors of Co_3O_4, which is one of the highly demanded electrode materials, is discussed.

A number of materials are available that are applied as the electrode materials for these supercapacitors. But transition metal oxides own their importance due to their highly ambitious features with high stability and durability[2,3]. Prime transition metal oxides like ruthenium oxide, manganese oxide, vanadium pentoxide, nickel oxide, and cobalt oxide come across this route. They assure less toxicity and more economic and environmental friendliness[4,5]. Kumar et al.[3] used nickel oxide to fabricate the electrodes with highly applicable upshots. A vast literature survey proves that Co_3O_4 based electrodes establish their eminence role with exclusively anticipating qualities[6–8]. Zhu et al.[9] synthesized Co_3O_4 microspheres via hydrothermal route and reached a specific capacitance of 879 Fg^{-1}. Tian et al.[10] synthesized Co_3O_4 thin films using the

chemical bath deposition method, which demonstrated a high specific capacitance of 743 Fg^{-1}.

There are various convenient procedures to synthesize desired Co_3O_4 nanostructures, including co-precipitation, solvothermal, hydrothermal, chemical bath deposition, and so on. Nan et al.[11] synthesized Co_3O_4/In_2O_3 nanostructures utilizing hydrothermal strategy. Luo et al.[12] synthesized a composite of MXene-Co_3O_4 via solvothermal approach. Xiao et al.[13] evidenced the synthesize of Pt@Co_3O_4 by in situ methods. Barbieri et al.[14] synthesized cobalt oxide nanostructures with chemical deposition manner with the gain of 130 Fg^{-1} of specific capacitance.

Since transition metal oxides execute the redox reactions, the charge storage mechanism behind these supercapacitors is pseudocapacitive in nature. Hence the outcome obviously depends on the availability of electrode surface area for the redox reactions, flexibility and agglomerations of nanoparticles of electrode material, presence of pores in the nanostructures, and dimensionality of the nanostructures. Hence, synthesizing nanostructures with tunable morphology is being developed by different researchers[15]. Utilizing a number of synthesis procedures, a variety of morphological features of nanomaterials can be obtained. Zero-dimensional (0D) nanomaterials include nanospheres and nanoclusters; one-dimensional (1D) nanomaterials include nanorods, nanowires, nanotubes, and nanofibers; and two-dimensional (2D) nanomaterials include thin films, nanodiscs, and nanoplates. Similarly, wide varieties of three-dimensional (3D) structures like nanoballs, nanocoils, nanocones, nanopillars, and nanoflowers can be synthesized. Luo et al.[16] synthesized Co_3O_4 with the 3D enoki mushroom-like structures. Raman et al.[17] synthesized Co_3O_4 with block and sphere morphology. Morphological structure, which donates the highest electrochemical outputs with practical applications, is most desired.

In this paper, transition metal oxides to be implemented in developing electrodes for supercapacitors are examined, and Co_3O_4 is found to be the most anticipating material for this. A brief overview of the different synthesize procedures is carried out, and the hydrothermal route of synthesizing is considered the best one to serve the electrochemical features like high specific capacitance. Finally, the impact of zero- to three-dimensional Co_3O_4 nanostructures on electrochemical outputs like specific capacitance, energy, and power density is scrutinized. A three-dimensional structure with its high efficiency is found to be at the top of all other-dimensional morphology[18].

2. Result and discussion

A simple combination of electrode-separator networks is folded and impregnated with the electrolyte to get the basic structure of a supercapacitor. Here the nature of electrodes forms a major contributor to the consequences of the supercapacitor applications. Nanostructured transition metal oxides are well-known materials with the most aspiring features to be used in the manufacture of electrodes. The presence of several oxidation states brings their applications to the next level. Due to this, an extremely large number of conducting paths can be formed, which increases the number of electrochemical redox reactions. Moreover, these materials demonstrate

high electrical and electrochemical stability, fast and reversible redox reactions, and elevated cycling stability.

Based on observations of several investigations[19–27], **Figure 1** shows the maximum specific capacitance reached when composites of several transition metal oxides are used. For example, in the case of ruthenium oxide, rGO/RuO_2 is used as the electrode material. Similarly, composites of nickel oxide (NiO nanocrystals as electrodes), molybdenum oxide (carbon/α-MnO_2 electrodes), indium oxide (In_2O_3), iron oxide (Fe_3O_4), manganese oxide (MnO_2), cobalt oxide (Co_3O_4), vanadium pentoxide (V_2O_5), and bismuth oxide (copper bismuth oxide electrode) are used in fabricating the electrode materials of supercapacitors. Besides these, there are some lesser-used oxides like perovskite bismuth iron oxide, ferrites, Ti-V-W-O/Ti oxide, and Na_2SO_3. But due to their various limitations and considerably lesser electrochemical outputs, they are not mentioned.

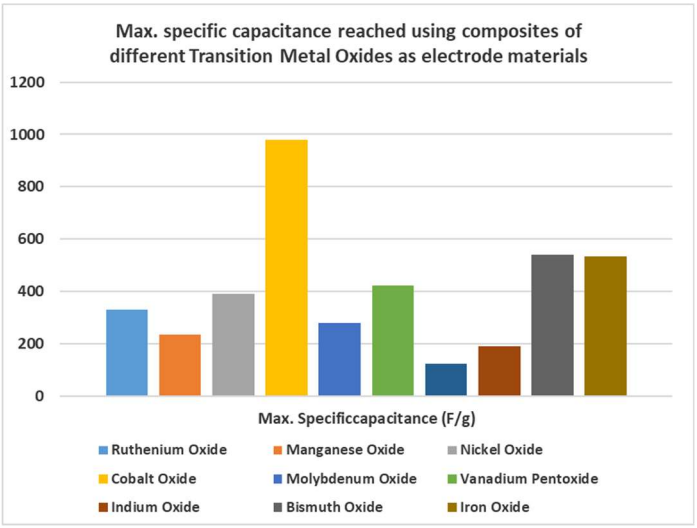

Figure 1. Maximum specific capacitance reached using composites of different transition metal oxides as electrode materials.

Among all the above transition metal oxides, cobalt oxide is found to demonstrate the highest specific capacitance value on account of its small band gap, structure of Co_3O_4 spinel, high crystallinity, high flexibility, exhibition of different morphological structures, and utilization of maximum oxidation states. Pure Co_3O_4 and Co_3O_4-based composites submit maximum impression on the enhancement of electrochemical activity of the generated electrodes[28]. All the other transition metal oxides exhibited considerably lesser electrochemical performance compared with the electrodes developed by cobalt oxide spinels. The number of investigations is increasing; concentrating on extracting several features of Co_3O_4 shows the efficiency of this spinel. Highly flexible Co_3O_4 nanostructures in various external features with high energy and power density values are employed in both pseudocapacitors and hybrid capacitors[29,30].

The synthesize strategy of these Co_3O_4 nanostructures in various appearances is large in counts applicable in accordance with convenience and availability of primary materials[31].

There are several, which are time-, cost-, and manpower-saving approaches like

hydrothermal, solvothermal, co-precipitation, in situ, chemical bath deposition, and solution combustion, as mentioned in **Figure 2**. This figure expresses the maximum specific capacitance exhibited by the differently prepared Co_3O_4 nanostructures used in the electrodes. Hydrothermal is a single-step easy method where cobalt nitrate and urea solution is heated at 150 °C under high pressure, followed by calcination for 24 h. Solvothermal includes dissolution of 0.1 M of cobalt II acetylacetonate and 0.2 M of cobalt III acetylacetonate in dilute ethanol, followed by heating at different temperatures under high pressure. Co-precipitation includes the drop-wise addition of cobalt nitrate solution to sodium hydroxide solution under a constant temperature of 90 °C and a constant pH of 10. This is followed by the collection, filtration, and calcination processes. In-situ synthesizes highly yields various metal-organic frameworks containing composites of Co_3O_4 nanostructures by various chemical reactions. Using a precursor solution, a chemical bath method can be used by depositing thin films of required materials like Co_3O_4. A chemical bath was generated by using proper amounts of solutions of 1 M $CoSO_4$, $NH_3 \cdot H_2O$, 0.25 M $K_2S_2O_8$ and demineralized water, and it was deposited on a suitable substrate. The solution combustion method includes the distribution of ions from exothermic reactions in a sol-gel medium. To synthesize Co_3O_4, various solvents like citric acid monohydrate, cobalt nitrate hexahydrate, and ammonium nitrate can be utilized in the form of fuel, oxidizer, and combustion enhancer, followed by the calcination process[32–35]. When these techniques are electrochemically compared, the Co_3O_4 nanostructure developed using the hydrothermal technique submitted the highest outputs.

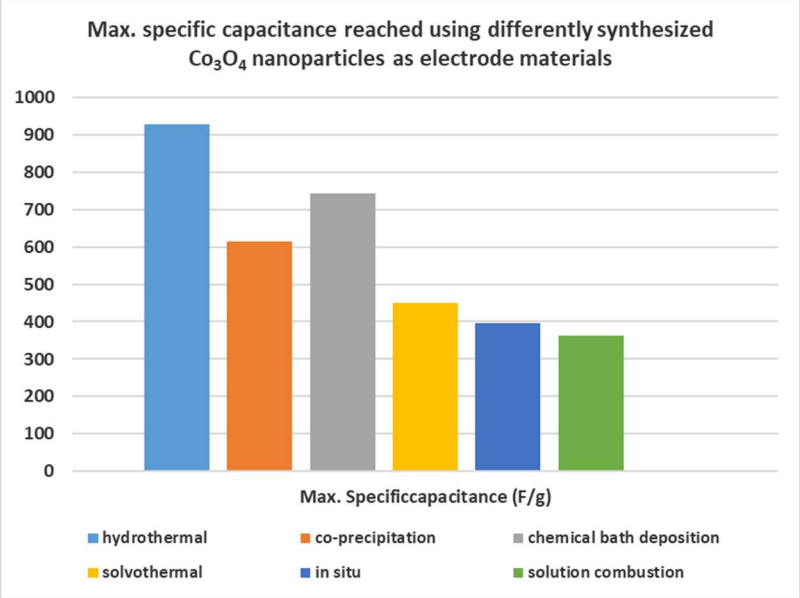

Figure 2. Maximum specific capacitance reached using differently synthesized Co_3O_4 nanoparticles as electrode materials.

The reason behind this can be justified as follows: The hydrothermal method is a soft chemical technique where an insoluble material at ambient temperatures is possible to make soluble at high temperatures and pressures. The hydrothermal technique shows the maximum possibility to process the advanced materials from the bulk to the nanorange, where the toughest and most complex compounds are

synthesized[36]. A number of merits can be observed in the hydrothermal method over other synthesize methods, and it is used to bring out nanomaterials that are not stable at elevated temperatures[37,38]. Since the resultant nanopowder is ultrapure, the high-temperature calcinations are not necessary. This fact eliminates the chance of re-clustering of nanoparticles and contamination. Nanoparticles with high vapor pressures can be prepared where the stoichiometry of the reaction and the size, shape, and composition of the resultant can be easily controlled. The purity of the prepared samples will be higher than the purity of the raw materials[39–41].

External morphology, including shape, porosity, and flexibility of the electrode material, shows a high impact on the electrochemical charge storage mechanism and hence on the efficiency of the supercapacitor. Wang et al.[42] synthesized a 3D nanonet hollow structure via the heterogeneous precipitation method and obtained 820 F/g of specific capacitance. Hou et al.[43] developed microspherical structures of Co_3O_4 by co-precipitation technique, and 614 F/g of specific capacitance was achieved. Piskin et al.[44] synthesized a 1D zinc oxide/cobalt oxide composite with the highest power density of 7500 Wg^{-1}. Co_3O_4 nanostructures, which are used as the electrode materials, exist in all 0, 1, 2, or 3D shapes synthesized via different routes[45–47]. **Figure 3** represents the relation between the maximum specific capacitance reached versus the dimensional morphology of Co_3O_4 nanostructures.

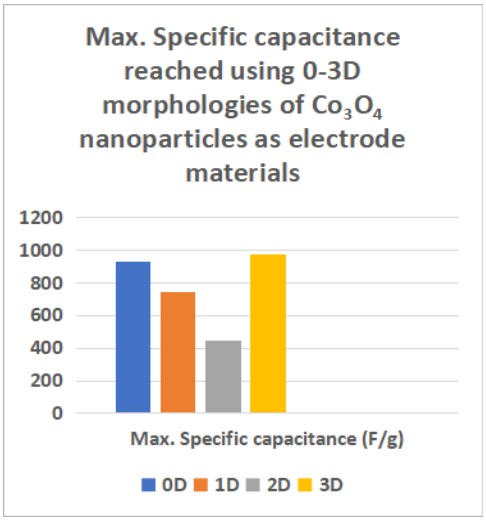

Figure 3. Relation between maximum specific capacitance and dimensional morphology of Co_3O_4 nanostructure.

0D nanomaterials exhibit high specific capacitance because of their high conductance, chemical inertness, minimized agglomeration, high mechanical stability, and high surface area available for faradaic redox reactions when compared with 1D or 2D nanomaterials. Yuan et al.[48] synthesized nanospheres for electrodes of supercapacitors with a specific capacitance of 928 Fg^{-1}. Deng et al.[49] showed that with the high agglomeration of nanoparticles, the specific capacitance decreased to 362 Fg^{-1}.

1D nanostructures of Co_3O_4 ensure external active area, thereby facilitating the motion of charged particles due to the influence of nanoscopic scale. But only the longitudinal axis of the material is the major pathway for the electron transfer[50]. Gao

et al.[51] developed nanowire arrays that could provide a specific capacitance of 746 Fg^{-1}. Different morphological types of 1D nanostructures can be formed by different foldings of nanosheets with differences in their electrical conductivity.

In the 2D nanosized structures, even though surface area is available, it lacks depth and dimensions. Also, due to the presence of point and line defects like vacancies, grain boundaries and pattern defects, cracks, and areal defects, the conductivity will be reduced. Yuan et al.[52] fabricated 2D Co_3O_4 film with mesoporous walls with the 443 Fg^{-1} of specific capacitance. 3D nanomaterials are the most abundant materials in comparison with other dimensional materials.

3D nanoparticles can be arranged into layers on surfaces, availing a high surface area, leading to increased surface activities[53]. They provide high absorption sites in all dimensions to cover all the molecules present. In addition to this, porous 3D nanostructures highly contribute to increased transportation of charged particles. 3D printing technology also favors the electrochemical results of the supercapacitors[54]. Zheng et al.[55] prepared a 3D hierarchical structure of Co_3O_4 with the highest specific capacitance of 978 Fg^{-1}.

Nearly the same result appears in **Figures 4** and **5**, which show the variation of energy and power density with respect to the dimensional morphology of Co_3O_4 nanostructures[56,57]. The energy density (E, Wh kg^{-1}) and power density (P, W kg^{-1}) are calculated using the equations[58,59],

$$E = 0.5 \times C_S \times (\Delta V^2)/3.6$$

$$P = E \times 3600/\Delta t$$

where ΔV speaks for the potential window during discharging time Δt.

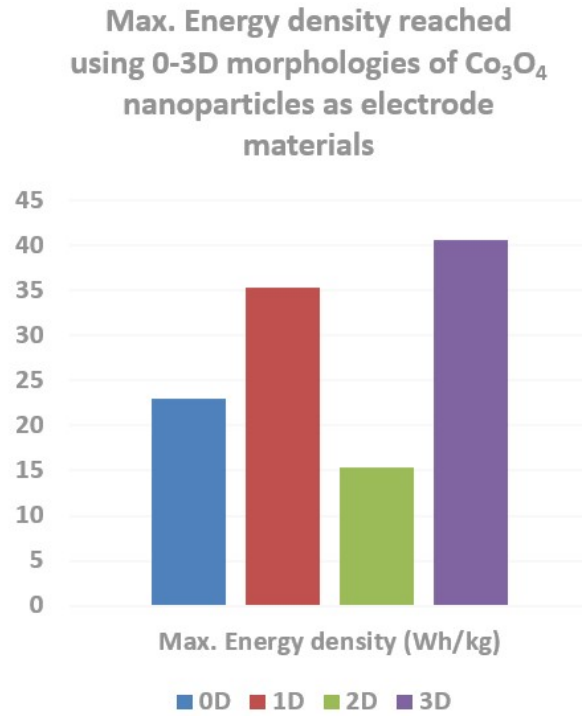

Figure 4. Relation between maximum energy density and dimensional morphology of Co_3O_4 nanostructure.

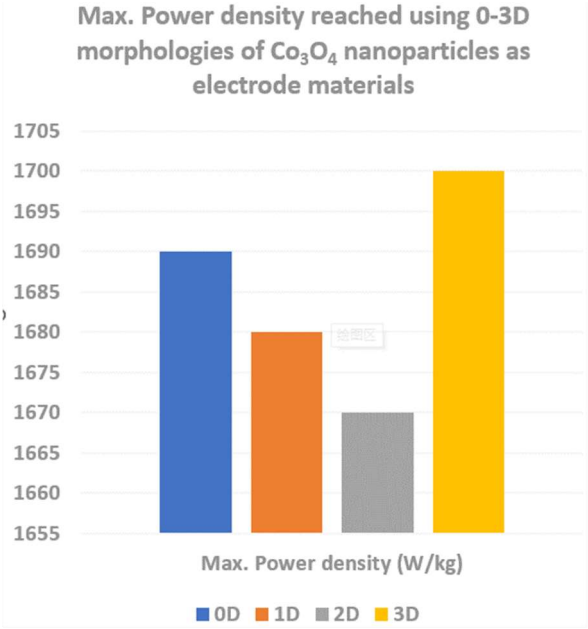

Figure 5. Relation between maximum power density and dimensional morphology of Co_3O_4 nanostructure.

Variation in energy density can be observed when specific capacitance and potential window vary. Also, power density depends upon energy density and the discharge time[60–64]. In both cases, as expected, 3D nanostructures provide a huge amount of electrochemical output.

3. Conclusion

Considering all transition metal oxides, Co_3O_4 is appraised as the efficient electrode material with innumerable practical merits. It can be synthesized by simple, time-saving, low-cost procedures in various morphological structures. According to a huge literature study, hydrothermal is found to be the most suitable method that has provided high electrochemical outputs. Though all 0D to 3D nanostructured Co_3O_4 is widely used in the electrodes of supercapacitors, 3D structured have proven comparatively more efficient due to accessibility of large surface area, possibility of various shapes and porosity, along with high conductance. Hence it leads to enhanced electrochemical results like high specific capacitance, energy, and the power density of a supercapacitor.

Conflict of interest: The authors declare no conflict of interest.

References

1. Zhang Q, Liu L, Zhang J, et al. Experimental investigation of starting-up, energy-saving, and emission-reducing performances of hybrid supercapacitor energy storage systems for automobiles. Journal of Energy Storage. 2023; 60: 106602. doi: 10.1016/j.est.2022.106602
2. Liu X, Xu F, Li Z, et al. Design strategy for MXene and metal chalcogenides/oxides hybrids for supercapacitors, secondary batteries and electro/photocatalysis. Coordination Chemistry Reviews. 2022; 464: 214544. doi: 10.1016/j.ccr.2022.214544
3. Kumar A, Rathore HK, Sarkar D, Shukla A. Nanoarchitectured transition metal oxides and their composites for supercapacitors. Electrochemical Science Advances. 2022; 2(6): e2100187. doi: 10.1002/elsa.202100187

4. Babu B, Kim J, Yoo K. Nanocomposite of SnO_2 quantum dots and Au nanoparticles as a battery-like supercapacitor electrode material. Materials Letters. 2022; 309: 131339. doi: 10.1016/j.matlet.2021.131339
5. Poudel MB, Kim AA, Lohani PC, et al. Assembling zinc cobalt hydroxide/ternary sulfides heterostructure and iron oxide nanorods on three-dimensional hollow porous carbon nanofiber as high energy density hybrid supercapacitor. Journal of Energy Storage. 2023; 60: 106713. doi: 10.1016/j.est.2023.106713
6. Al Jahdaly BA, Abu-Rayyan A, Taher MM, Shoueir K. Phytosynthesis of Co_3O_4 nanoparticles as the high energy storage material of an activated carbon/Co_3O_4 symmetric supercapacitor device with excellent cyclic stability based on a Na_2SO_4 aqueous electrolyte. ACS Omega. 2022; 7(27): 23673-23684. doi: 10.1021/acsomega.2c02305
7. Al Kiey SA, Abdelhamid HN. Metal-organic frameworks (MOFs)-derived Co_3O_4@N-doped carbon as electrode materials for supercapacitor. Journal of Energy Storage. 2022; 55: 105449. doi: 10.1016/j.est.2022.105449
8. Duan Z, Shi XR, Sun C, et al. Interface engineered hollow Co_3O_4@$CoNi_2S_4$ nanostructure for high efficiency supercapacitor and hydrogen evolution. Electrochimica Acta. 2022; 412: 140139. doi: 10.1016/j.electacta.2022.140139
9. Zhu YR, Peng PP, Wu JZ, et al. Co_3O_4@$NiCo_2O_4$ microsphere as electrode materials for high-performance supercapacitors. Solid State Ionics. 2019; 336: 110-119. doi: 10.1016/j.ssi.2019.03.022
10. Tian K, Wang JT, Xing L, et al. Nanostructure modulation of Co_3O_4 films by varying anion sources for pseudocapacitor applications. Solid State Ionics. 2021; 371: 115756. doi: 10.1016/j.ssi.2021.115756
11. Nan JJ, Guo S, Alhashmialameer D, et al. Hydrothermal microwave synthesis of Co_3O_4/In_2O_3 nanostructures for photoelectrocatalytic reduction of Cr(VI). ACS Applied Nano Materials. 2022; 5(7): 8755-8766. doi: 10.1021/acsanm.2c00107
12. Luo S, Wang R, Yin J, et al. Preparation and dye degradation performances of self-assembled MXene-Co_3O_4 nanocomposites synthesized via solvothermal approach. ACS Omega. 2019; 4(2): 3946-3953. doi: 10.1021/acsomega.9b00231
13. Xiao M, Yu X, Guo Y, Ge M. Boosting toluene combustion by tuning electronic metal support interactions in in situ grown Pt@Co_3O_4 catalysts. Environmental Science & Technology. 2022; 56(2): 1376-1385. doi: 10.1021/acs.est.1c07016
14. Barbieri EMS, Lima EPC, Lelis MFF, Freitas MBJG. Recycling of cobalt from spent Li-ion batteries as β-Co $(OH)_2$ and the application of Co_3O_4 as a pseudocapacitor. Journal of Power Sources. 2014; 270: 158-165. doi: 10.1016/j.jpowsour.2014.07.108
15. Xiong S, Yuan C, Zhang X, et al. Controllable synthesis of mesoporous Co_3O_4 nanostructures with tunable morphology for application in supercapacitors. Chemistry. 2009; 15(21): 5320-5326. doi: 10.1002/chem.200802671
16. Luo F, Li J, Lei Y, et al. Three-dimensional enoki mushroom-like Co_3O_4 hierarchitectures constructed by one-dimension nanowires for high-performance supercapacitors. Electrochimica Acta. 2014; 135: 495-502. doi: 10.1016/j.electacta.2014.04.075
17. Raman V, Suresh S, Savarimuthu PA, et al. Synthesis of Co_3O_4 nanoparticles with block and sphere morphology, and investigation into the influence of morphology on biological toxicity. Experimental and Therapeutic Medicine. 2016; 11(2): 553-560. doi: 10.3892/etm.2015.2946
18. Delbari SA, Ghadimi LS, Hadi R, et al. Transition metal oxide-based electrode materials for flexible supercapacitors: A review. Journal of Alloys and Compounds. 2021; 857: 158281. doi: 10.1016/j.jallcom.2020.158281
19. Korkmaz S, Kariper IA, Karaman O, Karaman C. The production of rGO/RuO_2 aerogel supercapacitor and analysis of its electrochemical performances. Ceramics International. 2021; 47(24): 34514-34520. doi: 10.1016/j.ceramint.2021.08.366
20. Roberts AJ, Slade RCT. Effect of specific surface area on capacitance in asymmetric carbon/α-MnO_2 supercapacitors. Electrochimica Acta. 2010; 55(25): 7460-7469. doi: 10.1016/j.electacta.2010.01.004
21. Zhang X, Shi W, Zhu J, et al. Synthesis of porous NiO nanocrystals with controllable surface area and their application as supercapacitor electrodes. Nano Research. 2010; 3: 643-652. doi: 10.1007/s12274-010-0024-6
22. Li J, Liu X. Preparation and characterization of α-MoO_3 nanobelt and its application in supercapacitor. Materials Letters. 2013; 112: 39-42. doi: 10.1016/j.matlet.2013.08.094
23. Zhang Y, Huang Y. Facile synthesis and characterization of rough surface V_2O_5 nanomaterials for pseudo-supercapacitor electrode material with high capacitance. Bulletin of Materials Science. 2017; 40(6): 1137-1149. doi: 10.1007/s12034-017-1470-5
24. Manikandan K, Dhanuskodi S, Maheswari N, Muralidharan G. SnO_2 nanoparticles for supercapacitor application. AIP Conference Proceedings. 2016; 1731(1): 050048. doi: 10.1063/1.4947702

25. Prasad KR, Koga K, Miura N. Electrochemical deposition of nanostructured indium oxide: High-performance electrode material for redox supercapacitors. Chemistry of Materials. 2004; 16(10): 1845-1847. doi: 10.1021/cm0497576
26. Ahmed AO, Samer BS, Nakate UT, et al. Electrodeposited spruce leaf-like structured copper bismuth oxide electrode for supercapacitor application. Microelectronic Engineering. 2020; 229: 111359. doi: 10.1016/j.mee.2020.111359
27. Lorkit P, Panapoy M, Ksapabutr B. Iron oxide-based supercapacitor from ferratrane precursor via sol-gel-hydrothermal process. Energy Procedia. 2014; 56: 466-473. doi: 10.1016/j.egypro.2014.07.180
28. Wang H, Shi Y, Li Z, et al. Synthesis and electrochemical performance of Co_3O_4/graphene. Chemical Research in Chinese Universities. 2014; 30(4): 650-655. doi: 10.1007/s40242-014-4109-8
29. Pang H, Li X, Zhao Q, et al. One-pot synthesis of heterogeneous Co_3O_4-nanocube/$Co(OH)_2$-nanosheet hybrids for high-performance flexible asymmetric all-solid-state supercapacitors. Nano Energy. 2017; 35: 138-145. doi: 10.1016/j.nanoen.2017.02.044
30. Che H, Lv Y, Liu A, et al. Facile synthesis of three dimensional flower-like Co_3O_4@MnO_2 core-shell microspheres as high-performance electrode materials for supercapacitors. Ceramics International. 2017; 43(8): 6054-6062. doi: 10.1016/j.ceramint.2017.01.148
31. Cui L, Li J, Zhang XG. Preparation and properties of Co_3O_4 nanorods as supercapacitor material. Journal of Applied Electrochemistry. 2009; 39(10): 1871-1876. doi: 10.1007/s10800-009-9891-5
32. Xie L, Li K, Sun G, et al. Preparation and electrochemical performance of the layered cobalt oxide (Co_3O_4) as supercapacitor electrode material. Journal of Solid State Electrochemistry. 2013; 17(1): 55-61. doi: 10.1007/s10008-012-1856-7
33. Xiao A, Zhou S, Zuo C, et al. Controllable synthesis of mesoporous Co_3O_4 nanoflake array and its application for supercapacitor. Materials Research Bulletin. 2014; 60: 674-678. doi: 10.1016/j.materresbull.2014.09.034
34. Gopalakrishnan M, Srikesh G, Mohan A, Arivazhagan V. In-situ synthesis of Co_3O_4/graphite nanocomposite for high-performance supercapacitor electrode applications. Applied Surface Science. 2017; 403: 578-583. doi: 10.1016/j.apsusc.2017.01.092
35. Michalska M, Xu H, Shan Q, et al. Solution combustion synthesis of a nanometer-scale Co_3O_4 anode material for Li-ion batteries. Beilstein Journal of Nanotechnology. 2021; 12(1): 424-431. doi: 10.3762/bjnano.12.34
36. Yoshimura M, Byrappa K. Hydrothermal processing of materials: Past, present and future. Journal of Materials Science. 2008; 43(7): 2085-2103. doi: 10.1007/s10853-007-1853-x
37. Carregosa JDC, Grilo JPF, Godoi GS, et al. Microwave-assisted hydrothermal synthesis of ceria (CeO_2): Microstructure, sinterability and electrical properties. Ceramics International. 2020; 46(14): 23271-23275. doi: 10.1016/j.ceramint.2020.06.021
38. Gan YX, Jayatissa AH, Yu Z, et al. Hydrothermal synthesis of nanomaterials. Journal of Nanomaterials. 2020; 2020: 8917013. doi: 10.1155/2020/8917013
39. Dhanalakshmi R, Denardin JC. Magnetic field enhanced photoreduction of Cr (VI) over the p-n-p $BiFeO_3$/$CoFe_2O_4$/Co_3O_4 nanocomposites. Journal of Magnetism and Magnetic Materials. 2022; 562: 169788. doi: 10.1016/j.jmmm.2022.169788
40. Askari MB, Rozati SM, Salarizadeh P, Azizi S. Reduced graphene oxide supported Co_3O_4-Ni_3S_4 ternary nanohybrid for electrochemical energy storage. Ceramics International. 2022; 48(11): 16123-16130. doi: 10.1016/j.ceramint.2022.02.160
41. Askari MB, Rozati SM. Construction of Co_3O_4-Ni_3S_4-rGO ternary hybrid as an efficient nanoelectrocatalyst for methanol and ethanol oxidation in alkaline media. Journal of Alloys and Compounds. 2022; 900: 163408. doi: 10.1016/j.jallcom.2021.163408
42. Wang Y, Lei Y, Li J, et al. Synthesis of 3D-nanonet hollow structured Co_3O_4 for high capacity supercapacitor. ACS Applied Materials & Interfaces. 2014; 6(9): 6739-6747. doi: 10.1021/am500464n
43. Hou L, Yuan C, Yang L, et al. Urchin-like Co_3O_4 microspherical hierarchical superstructures constructed by one-dimension nanowires toward electrochemical capacitors. RSC Advances. 2011; 1(8): 1521-1526. doi: 10.1039/C1RA00312G
44. Pişkin B, Uygur CS, Aydınol MK. Morphology effect on electrochemical properties of doped (W and Mo) 622NMC, 111NMC, and 226NMC cathode materials. International Journal of Hydrogen Energy. 2020; 45(14): 7874-7880. doi: 10.1016/j.ijhydene.2019.07.249
45. Shwetha KP, Manjunatha C, Kamath MKS, et al. Morphology-controlled synthesis and structural features of ultrafine nanoparticles of Co_3O_4: An active electrode material for a supercapacitor. Applied Research. 2022; 1(4): e202200031. doi: 10.1002/appl.202200031
46. Jamil S, Janjua MRSA, Khan SR. Synthesis of self-assembled Co_3O_4 nanoparticles with porous sea urchin-like morphology

and their catalytic and electrochemical applications. Australian Journal of Chemistry. 2017; 70(8): 908-916. doi: 10.1071/CH16694

47. Niveditha CV, Aswini R, Fatima MJJ, et al. Feather like highly active Co_3O_4 electrode for supercapacitor application: A potentiodynamic approach. Materials Research Express. 2018; 5(6): 065501. doi: 10.1088/2053-1591/aac5a7
48. Yuan C, Yang L, Hou L, et al. Large-scale Co_3O_4 nanoparticles growing on nickel sheets via a one-step strategy and their ultra-highly reversible redox reaction toward supercapacitors. Journal of Materials Chemistry. 2011; 21(45): 18183-18185. doi: 10.1039/C1JM14173B
49. Deng J, Kang L, Bai G, et al. Solution combustion synthesis of cobalt oxides (Co_3O_4 and Co_3O_4/CoO) nanoparticles as supercapacitor electrode materials. Electrochimica Acta. 2014; 132: 127-135. doi: 10.1016/j.electacta.2014.03.158
50. Toghan A, Khairy M, Kamar EM, Mousa MA. Effect of particle size and morphological structure on the physical properties of $NiFe_2O_4$ for supercapacitor application. Journal of Materials Research and Technology. 2022; 19: 3521-3535. doi: 10.1016/j.jmrt.2022.06.095
51. Gao Y, Chen S, Cao D, et al. Electrochemical capacitance of Co_3O_4 nanowire arrays supported on nickel foam. Journal of Power Sources. 2010; 195(6): 1757-1760. doi: 10.1016/j.jpowsour.2009.09.048
52. Yuan YF, Xia XH, Wu JB, et al. Hierarchically porous Co_3O_4 film with mesoporous walls prepared via liquid crystalline template for supercapacitor application. Electrochemistry Communications. 2011; 13(10): 1123-1126. doi: 10.1016/j.elecom.2011.07.012
53. Yu Z, Tetard L, Zhai L, Thomas J. Supercapacitor electrode materials: Nanostructures from 0 to 3 dimensions. Energy & Environmental Science. 2015; 8(3): 702-730. doi: 10.1039/C4EE03229B
54. Zhou H, Yang H, Yao S, et al. Synthesis of 3D printing materials and their electrochemical applications. Chinese Chemical Letters. 2022; 33(8): 3681-3694. doi: 10.1016/j.cclet.2021.11.018
55. Zheng Y, Li Z, Xu J, et al. Multi-channeled hierarchical porous carbon incorporated Co_3O_4 nanopillar arrays as 3D binder-free electrode for high performance supercapacitors. Nano Energy. 2016; 20: 94-107. doi: 10.1016/j.nanoen.2015.11.038
56. Hussain I, Lee JM, Iqbal S, et al. Preserved crystal phase and morphology: electrochemical influence of copper and iron co-doped cobalt oxide and its supercapacitor applications. Electrochimica Acta. 2020; 340: 135953. doi: 10.1016/j.electacta.2020.135953
57. Singh AK, Sarkar D, Karmakar K, et al. High-performance supercapacitor electrode based on cobalt oxide-manganese dioxide-nickel oxide ternary 1D hybrid nanotubes. ACS Applied Materials & Interfaces. 2016; 8(32): 20786-20792. doi: 10.1021/acsami.6b05933
58. Jiang Y, Chen L, Zhang H, et al. Two-dimensional Co_3O_4 thin sheets assembled by 3D interconnected nanoflake array framework structures with enhanced supercapacitor performance derived from coordination complexes. Chemical Engineering Journal. 2016; 292: 1-12. doi: 10.1016/j.cej.2016.02.009
59. Zhang M, Fan H, Zhao N, et al. 3D hierarchical $CoWO_4$/Co_3O_4 nanowire arrays for asymmetric supercapacitors with high energy density. Chemical Engineering Journal. 2018; 347: 291-300. doi: 10.1016/j.cej.2018.04.113
60. Deori K, Ujjain SK, Sharma RK, Deka S. Morphology controlled synthesis of nanoporous Co_3O_4 nanostructures and their charge storage characteristics in supercapacitors. ACS Applied Materials & Interfaces. 2013; 5(21): 10665-10672. doi: 10.1021/am4027482
61. Yadav S, Yadav J, Kumar M, Saini K. Synthesis and characterization of nickel oxide/cobalt oxide nanocomposite for effective degradation of methylene blue and their comparative electrochemical study as electrode material for supercapacitor application. International Journal of Hydrogen Energy. 2022; 47(99): 41684-41697. doi: 10.1016/j.ijhydene.2022.02.011
62. Wang J, Huang Y, Du X, et al. Hollow 1D carbon tube core anchored in Co_3O_4@SnS_2 multiple shells for constructing binder-free electrodes of flexible supercapacitors. Chemical Engineering Journal. 2023; 464: 142741. doi: 10.1016/j.cej.2023.142741
63. Kumar YA, Das HT, Guddeti PR, et al. Self-supported Co_3O_4@Mo-Co_3O_4 needle-like nanosheet heterostructured architectures of battery-type electrodes for high-performance asymmetric supercapacitors. Nanomaterials. 2022; 12(14): 2330. doi: 10.3390/nano12142330
64. Tang C, Yin X, Gong H. Superior performance asymmetric supercapacitors based on a directly grown commercial mass 3D Co_3O_4@$Ni(OH)_2$ core-shell electrode. ACS Applied Materials & Interfaces. 2013; 5(21): 10574-10582. doi: 10.1021/am402436q

Academic Publishing Pte. Ltd.

Add: 73 Upper Paya Lebar Road, #07-02B-01, Centro Bianco, Singapore 534818
Tel: +65 83184869
E-mail: editorial_office@acad-pub.com
Web: http://ojs.acad-pub.com/